

Dissertation

Numerisches Simulationsverfahren für die präzise Berechnung der menschlichen Phonation unter realen Bedingungen

ausgeführt zum Zwecke der Erlangung des akademischen Grades
eines Doktors der technischen Wissenschaften unter der Leitung von

Univ.Prof. Dipl.-Ing. Dr.techn. Manfred Kaltenbacher
Institut für Mechanik und Mechatronik
Abteilung für Messtechnik und Aktorik, E325/A4

eingereicht an der Technischen Universität Wien
Fakultät für Maschinenwesen und Betriebswissenschaften

von

Dipl.-Math. Stefan Zörner
Mat.Nr. 0861599
Wilhelminenstr. 34/6
1160 Wien

Wien, November 2013

Kurzfassung

Die menschliche Stimme ist das alltägliche Instrument zur verbalen Kommunikation. Eine Erkrankung der Stimme, die so genannte Dysphonie, wie Heiserkeit, kann somit beträchtliche Auswirkung auf die Lebensqualität haben. Einschränkungen auf privater sowie beruflicher Ebene sind die Folge. Um die Mechanismen und dessen Ursachen nachzuvollziehen, die eine gesunde Stimme von der einer erkrankten unterscheidet, muss zunächst der Stimmbildungsprozess grundlegend verstanden werden.

Die computergestützte Simulation ist im Falle der menschlichen Phonation ein hilfreiches Werkzeug, da sie nicht invasiv ist. Allerdings stößt eine exakte Nachbildung der komplexen Vorgänge der Phonation an die Grenzen der heutigen Rechenkapazitäten. Um diesem entgegenzuwirken, ist es notwendig, das Modell zu vereinfachen. Diese Dissertation analysiert verschiedene Modellvereinfachungen und die dadurch verursachten modellbasierten Fehler. Für die Untersuchungen wurde das Computerprogramm *CFS++* verwendet und erweitert, um die Interaktion von Strömung (Luft) und Strukturvibrationen (Stimmlippenschwingung) simulieren zu können. Ebenfalls können mit dem Programm die daraus entstehenden Schallquellen und die Schallausbreitung berechnet werden. Zuerst wird die Auswirkung der geometrischen Modellierung der Stimmlippen untersucht. Dazu werden in einer voll gekoppelten Strömungs-Struktur-Simulation die Schwingungen zweier unterschiedlicher geometrischer Stimmlippenmodelle genauestens miteinander verglichen. Ferner wird untersucht, ob die Kopplung von Strömung und Struktur zu einer reinen Strömungssimulation reduziert werden kann. Die Schwingung der Stimmlippen wird dabei mit speziellen Randbedingungen imitiert. Zusätzlich werden unterschiedliche aeroakustische Analogien untersucht und verglichen. Die akustischen Verfahren ermöglichen dabei eine genaue Ortung der akustischen Quellen bei der Stimmerzeugung. Das entwickelte Simulationsverfahren ist ebenfalls dazu fähig, den Vokaltrakt zu berücksichtigen, um beispielsweise das erzeugte Schallfeld eines Vokals zu berechnen.

Ehrenwörtliche Erklärung

Ich erkläre ehrenwörtlich, dass ich die vorliegende wissenschaftliche Arbeit selbstständig angefertigt und die mit ihr unmittelbar verbundenen Tätigkeiten selbst erbracht habe. Ich erkläre weiters, dass ich keine anderen als die angegebenen Hilfsmittel benutzt habe. Alle aus gedruckten, ungedruckten oder dem Internet im Wortlaut oder im wesentlichen Inhalt übernommenen Formulierungen und Konzepte sind gemäß den Regeln für wissenschaftliche Arbeiten zitiert und durch Fußnoten bzw. durch andere genaue Quellenangaben gekennzeichnet.

Die während des Arbeitsvorganges gewährte Unterstützung einschließlich signifikanter Betreuungshinweise ist vollständig angegeben. Die wissenschaftliche Arbeit ist noch keiner anderen Prüfungsbehörde vorgelegt worden. Diese Arbeit wurde in gedruckter und elektronischer Form abgegeben. Ich bestätige, dass der Inhalt der digitalen Version vollständig mit dem der gedruckten Version übereinstimmt.

Ich bin mir bewusst, dass eine falsche Erklärung rechtliche Folgen haben wird.

(Unterschrift)

(Ort, Datum)

Dissertation

**Numerical simulation method for a
precise calculation of the human
phonation under realistic conditions**

performed for the purpose of obtaining the academic degree
of Doctor of Technical Science
under the supervision of

Univ.Prof. Dipl.-Ing. Dr.techn. Manfred Kaltenbacher
Institute of Mechanics and Mechatronics
Measurement and Actuator, E325/A4

submitted to the Vienna University of Technology
Faculty of Mechanical and Industrial Engineering

by

Dipl.-Math. Stefan Zörner

Mat.Nr. 0861599
Wilhelminenstr. 34/6
1160 Wien

Vienna, November 2013

Abstract

The human voice is essential for day-to-day communication. Consequently, impairment of speech, known as dysphonia, may have a significant impact on a person's career and possibly even their social life. To understand the mechanisms and effects that distinguish a healthy voice from an unhealthy one, the phonation process itself must be understood. In the case of human phonation, computer aided simulation is a useful tool, as it is non-invasive. However, if the target is to achieve an exact replica, the complex nature of the phonation process pushes the bounds of current research and also demands high computational capacities. Simplifications in the model are therefore necessary to counteract these problems. This thesis analyses different kinds of simplifications and the error which is caused by the corresponding model. These investigations were carried out with the simulation tool *CFS++*, and extended to allow for a precise simulation of the interaction between air flow and structural (vocal fold) vibration. Furthermore, it is also capable of determining the acoustic sources and propagation of aeroacoustical and vibration-induced sound.

Firstly, the impact of the geometrical shape of the vocal folds is studied. Thereby, a fully coupled fluid-structure simulation is employed to compare two different kinds of vocal fold models. Moreover, investigations have been performed if the coupling of fluid and structure can be reduced to a pure flow simulation. The vocal fold vibration is thereby imitated by special boundary conditions. In addition, different aeroacoustic analogies are analysed and compared. These acoustic methods also permit a precise location of the sound sources during phonation. We also present an enhancement of the model, which integrates and considers the acoustic impact of the vocal tract, to calculate for instance the sound field of a vowel.

Acknowledgements

First and foremost, I want to thank my supervisor Univ.Prof. Dipl.-Ing. Dr. techn. Manfred Kaltenbacher, who supported me throughout my Ph.D.. His ability to create a supportive environment inside the research group ensured constructive and positive working conditions. Most notable are the technical discussions and the freedom of creativity that allows one to thrive in research. Furthermore, I am grateful for the chance to participate in the international renowned research group *DFG FOR894*, which was funded by the *German Research Foundation* (DFG) and the *Austrian Science Fund* (FWF) under grant No. I 532 N20, which is gratefully acknowledged. Head of the research group *FOR894* is Prof. Dr. Ing. Dipl.-Math. Michael Döllinger, who is key to its success. I would like to thank him for taking interest in my work by accepting the task of second supervisor. The main research partners in this group were Univ.Prof. Dr. Ing. C. Brücker and Dipl.-Ing. W. Mattheus, who I like to thank for supplying me with fluid simulation data for the 3D aeroacoustic simulations. For interesting discussions and helpful collaboration I would also like to thank each head of the subgroups involved in the *FOR894* research, Prof. Dr. med. Dr. rer. nat. Dipl.-Phys. U. Eysholdt, Prof. Dr. rer. nat. Dipl.-Math. G. Leugering, Prof. Dr. rer. nat. Dipl.-Math. M. Stingl, Prof. Dr. Ing. R. Lerch, PD Dr. Ing. S. Becker, as well as their researchers and Ph.D. students Prof. Dr. Ing. R. Schwarze, Dipl.-Ing. W. Mattheus, Dr. Ing. M. Triep, Dipl.-Phys. C. Kirmse, Dipl.-Math. B. Schmidt, Dr. Ing. A. Sutor, Dipl.-Ing. S. Weiss, Dipl.-Ing. S. Kniesburges, Prof. Dr. Ing. J. Lohscheller, Dr. Ing. A. Yang and Dr. Ing. G. Luegmair.

Moreover, I would like to thank my colleagues at the Chair of Sensor Technology in Erlangen (Germany), my colleagues at the technical faculty in Klagenfurt (Austria) and my colleagues at the research group of Measurement and Actuators in Vienna (Austria) for a pleasant and enjoyable working environment. I especially want to mention Dr. techn. Andreas Hüppe, Dr. techn. Hendrik Husstedt and Dr. techn. Simon Triebenbacher for their support during technical discussions and helpful

ideas, as well as their moral support, which led to a solid friendship.

For additional flow data, which enabled further 3D aeroacoustic simulations, I would like to thank Dr.-Ing. Petr Šidlof. With his friendly attitude and his eager will, we were able to develop a productive cooperation, which was intensified through the support of the Czech and Austrian agencies for international cooperation and mobility within ICM OeAD - MŠMT (project No. CZ 09/2013). This is also gratefully acknowledged.

I also like to thank U. Katz, K. Puschel, R. Polterauer and B. Pimperl for their great support in organisational matters, which allowed me to focus on my research.

Finally, I would like to express my gratitude for the support of my family - my siblings for their moral and personal encouragement and my parents for allowing me to freely develop my goals and supporting me in my chosen path.

Contents

1	Introduction	1
1.1	Motivation	1
1.1.1	Outline	3
1.2	Human phonation	4
1.2.1	Basic laryngeal physiology	4
1.3	Current status of research	6
1.3.1	Lumped element models	7
1.3.2	PDE based models	9
1.3.3	Material parameter measurement	12
2	Governing equations and their FE-formulation	14
2.1	Fluid mechanics	15
2.1.1	Spatial reference systems	15
2.1.2	Navier-Stokes equations	18
2.1.3	Finite element formulation	24
2.1.4	SUPG method	26
2.1.5	Time discretisation and linearisation	28

2.2	Solid mechanics	30
2.2.1	Finite element formulation	33
2.2.2	Structural damping (steady state case)	34
2.3	Fluid-Solid interaction	36
2.3.1	Aitken relaxation	37
2.3.2	Mesh smoothing	37
2.4	Aeroacoustics	39
2.4.1	Lighthill's analogy	40
2.4.2	Finite element formulation – wave equation	42
2.4.3	Perturbation equations (incompressible flow)	43
2.4.4	Alternative source terms for the wave equation	45
3	Vocal fold models and material parameters	49
3.1	2D geometrical model	50
3.1.1	M5 vocal fold shape	52
3.2	Determining material parameters with the pipette aspiration method	52
3.2.1	Pipette aspiration set-up	54
3.2.2	Pressure inducer and measurement	55
3.2.3	Damping measurement set-up	56
3.2.4	Numerical framework	58
3.2.5	Results	59
4	2D Simulation results	63
4.1	Numerical framework	64
4.1.1	Boundary conditions	64
4.1.2	Grid dependency	65
4.2	Comparison of vocal folds geometry	67
4.3	Investigation of prescribed movement	71
4.3.1	Vocal fold vibration	72
4.3.2	Case study: homogeneous boundary condition	73
4.3.3	Case study: 800Pa	76
4.3.4	Case study: reformed vocal folds	77
4.3.5	Case study: reformed vocal folds with prescribed inflow	78

4.3.6	Conclusion and summary	81
5	3D Simulation results	82
5.1	Velocity driven flow	84
5.1.1	Geometry	84
5.1.2	Numerical framework	86
5.1.3	Similitude model	87
5.1.4	Acoustic sources	90
5.1.5	Aeroacoustic fields	91
5.2	Pressure driven flow	97
5.2.1	Geometry	98
5.2.2	Acoustic sources	101
5.2.3	Vocal tract influence	102
5.2.4	Acoustic impact of false vocal folds	106
5.2.5	Discussion and conclusions	107
6	Conclusion	109
6.1	Outlook	111
	Appendices	112
A	Anatomical terms of location	112
B	Mathematics for engineers	114
	Bibliography	119

Notation and Abbreviations

In this thesis, scalars are represented by normal letters (b), Cartesian vectors are set in bold-italic letters (\mathbf{b}) and tensors by bold letters in square brackets ($[\mathbf{b}]$). Matrices are capital boldface Roman letters (\mathbf{B}).

Abbreviations

ALE	Arbitrarily Lagrangian-Eulerian Method
BDF2	2nd order backward difference method
CFD	computational fluid dynamics
<i>CFS++</i>	Coupled Field Simulation
DNS	direct numerical simulation
FDM	finite difference method
FE	finite element
FEM	finite element method
FSAI	fluid-structure-acoustic interaction
FSI	fluid-structure interaction
FVF	false vocal fold

FVM	finite volume method
HBC	homogeneous boundary condition
IBVP	initial boundary value problem
LES	large eddy simulation
NSC	no-slip condition
NSE	Navier-Stokes equations
ODE	ordinary differential equation
PDE	partial differential equation
PE	perturbation equation
SUPG	Streamline-Upwind-Petrov-Galerkin
SPL	sound pressure level
VF	vocal fold

Fluid mechanics

Γ_f	fluid boundary
μ	dynamic viscosity
ν	kinematic viscosity
\mathbf{p}	fluid pressure
\mathbf{P}	kinematic fluid pressure
ρ_f	fluid density
$\boldsymbol{\sigma}_f$	fluid stress
$\boldsymbol{\tau}$	viscous stress
\mathbf{v}	fluid velocity
\mathbf{v}_c	convective velocity
\mathbf{v}_g	grid velocity
Ω_f	fluid domain

Structural mechanics

$[\mathbf{c}_s]$	tensor of elasticity
E	elasticity modulus

Notations and Abbreviations

Γ_s	structural boundary
λ_L	Lamé parameter
μ_L	Lamé parameter
ν_P	Poisson's ratio
ρ_s	structural density
$[\boldsymbol{\sigma}_s]$	mechanical stress tensor
\mathbf{u}	mechanical displacement
Ω_s	structural domain

Acoustics

c	speed of sound
Γ_a	acoustic boundary
p'	acoustic pressure (Lighthill formulation)
p_0	temporal and spacial mean pressure (Lighthill formulation)
p^{ic}	fluid pressure (incompressible formulation)
\bar{p}	mean pressure
p^h	fluctuating hydrodynamic pressure
p^a	acoustic pressure (perturbation formulation)
ρ_0	temporal and spacial mean density (Lighthill formulation)
ρ^c	fluid density (compressible formulation)
$\bar{\rho}$	mean density
ρ^h	fluctuating hydrodynamic pressure
ρ^a	acoustic density (perturbation formulation)
\mathbf{v}^{ic}	fluid velocity (incompressible formulation)
$\bar{\mathbf{v}}$	mean fluid velocity
\mathbf{v}^h	fluctuating hydrodynamic velocity
\mathbf{v}^a	acoustic particle velocity
Ω_a	acoustic domain

CHAPTER 1

Introduction

This research originated as part of an interdisciplinary research group called *DFG FOR894* with the joint research topic “Fluid Mechanical Basis of the Human Voice”. It was funded by the *German Research Foundation* (DFG) and the *Austrian Science Fund* (FWF) and consists of seven subprojects situated at the *Friedrich-Alexander University Erlangen-Nuremberg*, the *Technische Universität Bergakademie Freiberg* and the *Vienna University of Technology*. The aim of the project is to gain a better physical and fundamental understanding of the sound generating mechanisms of phonation and their influences on the perceived voice quality.

1.1 Motivation

Human voice is sound generated inside the larynx and modulated by the oral cavities, called vocal tract. Voice is used as a primary method for

communication in the form of speech and even by means of music or emotional expressions (laughing, crying etc.). Any kind of voice disorder, or dysphonia, is therefore a serious condition as it limits the afflicted individuals from a social perspective. A number of pathologies cause dysphonia: bacterial infection of the larynx (laryngitis), carcinomas, laryngeal papillomatosis, vocal fold (VF) nodules, cysts, polyps, bi- and unilateral VF paralysis. Resulting voice quality impairment, e.g., hoarseness and subharmonic variations, are characterised by jitter, shimmer (varying frequency and pitch, respectively) and biphonation (multiple fundamental frequencies).

The aim of this work is to understand the complete sound generating process in the voice, to identify the mechanisms causing the perceived dysfunction and thereby build the basis for future treatments to ensure a healthy voice. Prospectively, this could be used for targeted healing, assisting surgery, optimising implants or recommendations on long-term vocal training – In a related work, a first insight into these questions provided by Birkholz [10] has already made significant improvements in speech synthesis possible.

To understand the underlying mechanisms, a physical model of the human voice is required as direct measurements are invasive. In physical terms it is an interaction of flow dynamics, structural dynamics and acoustics (FSAI). This model can be expressed by a set of partial differential equations (PDEs) and can be solved numerically. However, due to the high complexity of these equations and the correspondingly resulting long computational time, several modifications are necessary to simplify the problem so that viable calculation are possible. Firstly, voice simulation can be split up geometrically into the larynx and vocal tract, separating sound generation and filtering. Further problem reducing possibilities include, for example, geometric simplification or reducing the system to a 2D model. Existing known methodologies in numerically simulating and modelling the human phonation process are detailed in section 1.3.

Working towards technologies to analyse and understand the human voice, this thesis employs a 2D coupled fluid-structure interaction (FSI) simulation to inspect the validity of model reduction. Model reduction is a necessity, since current computerised replicas of phonation all require

some kind of trade-off, to counteract the high complexity of the system and thereby thus the high computational cost. Additionally, geometrical simplifications are also common due to missing or inaccurate data and they also allow easier analysis. This thesis addresses these issues of model based errors by comparing full and partial coupling between air flow and structural vibration of the VFs, by analysing the effects of different geometry models, and by examining two aeroacoustic methods. The latter provides insight into the precise sources of voice production and demonstrates an applicability for simulating the whole speech process.

All aeroacoustic results and all simulations concerning 2D FSI were performed with the in-house research code *CFS++*, which is covered in detail by Kaltenbacher [54]. The FSI code as provided by Link et al. [62] was extended and used for the investigations.

1.1.1 Outline

To achieve the objectives set in the motivation section 1.1, this thesis is organised as follows. In section 1.2, the basic principles of the larynx as sound generator and its anatomical structure are briefly introduced in order to provide a first view of the problem at hand. Section 1.3 presents the current status of research with regard to simulating the human phonation process and determining VF material parameters in order to ensure an accurate material model.

In chapter 2, the theoretical background of fluid dynamics, solid mechanics, acoustics and the interaction between these physical fields are covered. As one focus of this work is aeroacoustics, two hybrid methods are presented: Lighthill's analogy ([59]) and the perturbation equations ([47]). The resulting partial differential equations from all three physical fields are put into finite element context to enable implementation in the in-house research code *CFS++*.

To complete the simulation framework, chapter 3 describes the 2D geometry of the laryngeal layout and additionally specifies material parameters required for the continuum mechanical model. Based on the method presented, the 2D results of a phonation simulation are studied in chapter 4. One task is to determine the impact of the geometrical model of the VFs

on the vibrational pattern and flow field inside the larynx. A second is to analyse two way coupled fluid structure interaction and determine whether simplifying phonation simulations by a one way coupling is justified.

Effects of aeroacoustics during phonation are discussed in chapter 5 using two 3D flow simulation models with prescribed VFs motions. In general, the aim is to provide insight into the basic principle of sound generating mechanism of human phonation and to study, compare and verify various different aeroacoustic approaches.

1.2 Human phonation

The human voice is the basis for verbal communication, i.e., speech. Its primary signal is generated inside the larynx by the two opposing oscillating VFs ([23]). The entire process of the human voice is a complex interaction of fluid mechanics, solid mechanics and acoustics. In a healthy voice, the process is initialised by a tensioning of the VFs, which seals the larynx. As the lungs compress, air pressure builds up causing a pressure gradient between the subglottal and the supraglottal region. An air stream is thereby induced through the trachea onto the VFs, forcing them to open. The air stream equalises subglottal and supraglottal pressure which, in turn reduces the velocity of the air stream itself, enabling the VFs to close up again, thus repeating the process. This creates a pulsating air stream, which together with VFs vibrations and supraglottal air vortices form the source of the perceived acoustic sound. For adult females the fundamental frequency is in the range of 165 to 255 Hz and for adult males, from 85 to 155 Hz ([33]).

1.2.1 Basic laryngeal physiology

The human larynx is part of the respiratory system. It is located inside the neck and measures about 5 cm long. Besides phonation it has several tasks, as it connects the trachea with the pharynx. It is also a passage for air to reach the lungs and the epiglottis protects it from stray food particles by acting as lid during swallowing.

Figure 1.1a displays a coronal¹ cut of the larynx. It is comparable to a simple tube with a constriction half way along it, the glottis. The form of the glottis is determined by the positioning of the two opposing VFs. Superior to the VFs are the ventricular folds also known as false vocal folds (FVFs). The mucosa forms a protuberance between the VFs and the FVFs known as the laryngeal sinus or ventricle. Figure 1.1b is a superior view of a transversal cut through the larynx and exposes the VFs and their “V”-like position. Posterior, the VFs are attached to the pyramidal

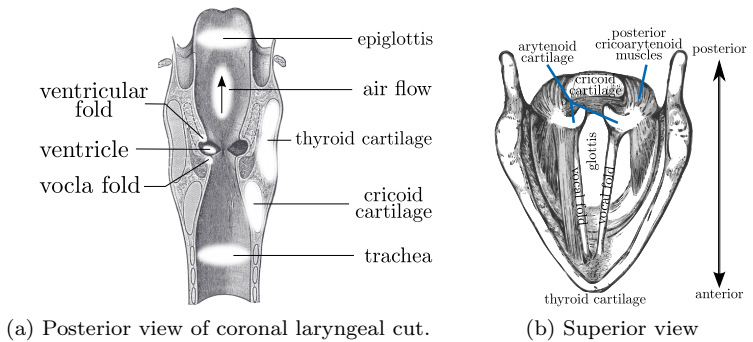


Figure 1.1: Larynx structure ([38]).

shaped arytenoid cartilages, which are linked by joints to the cricoid cartilage (see Fig. 1.1b). The cricoid cartilage is ring shaped and forms the basis of the larynx, as depicted in Fig. 1.2. Two joints (cricothyroid joints) join the ring shaped cricoid cartilage to the thyroid cartilage, which surrounds the inner parts of the larynx, thereby protecting them. The cricoid and thyroid cartilages can be tiled against each other and put the VFs under tension. However, the main mechanism to control the VFs is via the arytenoid cartilage. These pivot-mounted cartilages can be turned, mainly by the posterior cricoarytenoid muscles, which

¹Anatomical planes and directional terms are explained in Appendix A.

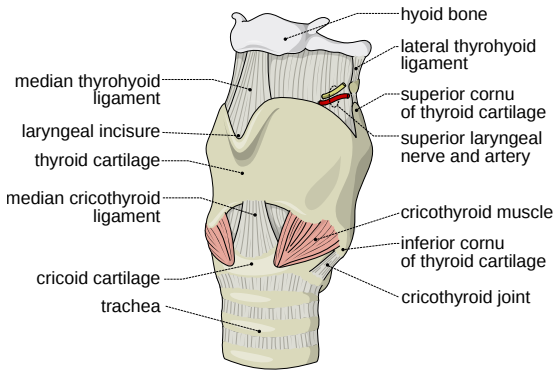


Figure 1.2: Anterior-lateral view of larynx (Larynx external by Olek Remesz/ Wikimedia Commons / CC-BY-SA-2.5).

also causes the cartilages to be pushed and pulled in the anterior and posterior direction. These adjustments regulate the distance between the VFs and can close the glottis completely to initiate the phonation process. Furthermore, they control the tension of the VFs, which modulates the pitch of the voice.

1.3 Current status of research

This section will provide an overview of the current status of mathematical models for the human phonation process, as they have served as valuable tools for providing an insight into the basic mechanisms of phonation and may eventually be of sufficient detail and accuracy to allow surgical planning, diagnostics, and rehabilitation evaluations on an individual basis. In section 1.3.1, we present lumped element models, which are still used and in process of further development. What they lack in precision, they make up for in computational speed, making real time simulations possible. For more accurate modelling, section 1.3.2 presents

an overview of continuum mechanical models based on partial differential equations (PDE). These accurately describe the physical properties of fluid flow, structural mechanics and acoustics, but have the disadvantage of having a high order of complexity and thereby leading to larger computation costs.

For a correct continuum mechanical model, accurate material parameters are essential. As these must be determined by experiment, a brief overview of existing experimental set-ups to measure vocal fold tissue is provided in section 1.3.3.

1.3.1 Lumped element models

The fundamental idea of lumped element models is to divide up the structure, in this case the vocal folds, into masses and couple them via springs and dampers. Figure 1.3 illustrates how the structure may be represented by a simple two mass model in the case of the vocal folds. The governing equations to determine the displacement x_i of mass m_i

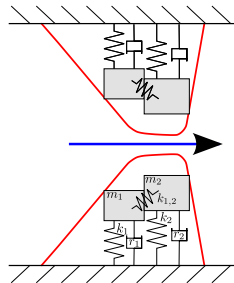


Figure 1.3: Schematic illustration of a multi-mass model for vocal folds structure, represented by masses (m), springs (k), and dampers (r).

are given by

$$\begin{aligned} m_1\ddot{x}_1 + r_1\dot{x}_1 + k_1x_1 + k_{1,2}(x_1 - x_2) &= F_1, \\ m_2\ddot{x}_2 + r_2\dot{x}_2 + k_2x_2 + k_{1,2}(x_2 - x_1) &= F_2, \end{aligned}$$

with the constant parameters r_i and k_i representing damping and stiffness, respectively, whereas $k_{i,j}$ represents the coupling stiffness of the masses m_i and m_j . F_i is the force of the air flow acting on the vocal folds, which needs to be computed. In lumped models, fluid flow is usually computed by Bernoulli's equation, due to its simplicity and thus computational time. It assumes that the fluid acts like a mass that is accelerated and decelerated as a unit.

Even simpler would be a single mass model, as used by Flanagan and Landgraf [34]. However, for the vocal fold to induce self-oscillation due to the flow, multiple masses are necessary ([88]). Thus, Ishizaka and Isshiki [50] improved the model to a two mass model. This enables a phase difference in vertical direction of the masses, known as convergent and divergent shape. In early works focusing on asymmetric left and right vocal folds, this computational simulation was already being used to study pathologies (Ishizaka and Isshiki [50]). Results were similar to physiological experiments on natural larynges and it was possible to synthesise different types of hoarse voice by applying a vocal tract synthesiser. Later Steinecke and Herzel [81] simplified the model and studied non-linear dynamics and the location of instabilities due to different stiffness values in left and right VF characteristic for laryngeal paralysis.

To capture longitudinal tension, a 10 mass model was presented by Wong et al. [98], which also covers pathological cases and investigates their effects, e.g. local mass changes are made to study the impact of cancer. Additional advantages of high dimensional lump mass models are their detailed anatomical and physiological structure description, and the fact that they can simulate complicated spatial-temporal modes, which exist in real vocal folds. With these models even the singing voice may be studied, as done by Kob [56]. A further improvement in geometrical detail was presented by Titze [86, 87], a 16 mass model which not only considers the anterior-posterior direction, but also models coarse spatial

variation by considering the different tissue layers of VFs. This model has been updated by Titze [89], p. 164 in which 175 point mass construct is used, with 7 layers describing the vibrating tissue, 5 divisions in the inferior-superior direction, and 5 divisions in the anterior-posterior direction. A more recent work paving the way for 3D lumped element models was designed by Yang et al. [99], a 25 mass model optimised to fit model dynamics of experimental data. Fitting lumped element parameters defining the multi mass model are crucial and were extracted from endoscopic imaging for the first time by Döllinger et al. [27]. Digital high-speed images were recorded to determine vibrating masses, VF tension and subglottal pressure by means of optimisation. Yang et al. [99] further enhanced the method by using endoscopic recording to automatically determine the parameters of their 3D model.

Bernoulli's equation assumes laminar flow, but air flow during phonation inside the larynx is asymmetric as shown by simulation results of Alipour et al. [3], Link et al. [62] and Mittal et al. [69]. Therefore, Tao et al. [84] used the NSE (Navier-Stokes equations) to describe the flow field, and this computed flow forces acting onto the lumped element structure model. The fluid mesh was divided up into less than 3k unknowns in order to retain the advantage of a relatively fast solver. However, due to the low resolution of the flow, a correct representation cannot be achieved and the impact of the asymmetric flow in contrast to a symmetric flow has not been analysed in depth.

For an additional summary and review on different lumped element approaches, Alipour et al. [3] and Birkholz [11] describe the current status. It is also noteworthy that the thesis of Birkholz [10] covers the whole speech process based on lumped element models and the resulting software is capable of acoustically generating complete sentences.

1.3.2 PDE based models

With a continuum mechanical assumption, the phonation process is formulated by a set of partial differential equations (PDEs), describing fluid mechanics, structural mechanics and acoustics. The accurate physical representation has its drawback in computational cost, as numerical

methods are required to solve the PDEs which may result in a number of unknowns that can only be calculated with supercomputers—high computational effort applies primarily for CFD. Nevertheless, both capturing the physics and resolving the physiological structures – not possible with lumped elements – is necessary in order to understand and analyse the fundamentals of voice production. A continuum approach was first presented by Alipour et al. [2] using 2D FE to simulate the vocal fold vibration, while retaining Bernoulli’s equations to determine the fluid forces acting on the structures. With the help of a lumped element model of the VFs, de Vries et al. [21] showed that the NSE exhibited a significantly higher phonation threshold pressure in comparison to the Bernoulli’s equation and a glottal peak flow twice as high. de Oliveira Rosa et al. [19] presented the first fluid-structure coupled PDE approach for human phonation, which was solved using FEs. Although, the discretisation of the flow domain was too coarse to fully resolve the flow, the author was able to demonstrate self-sustained oscillation of the VFs.

As so called hemilarynx approaches reduce the number of unknowns by half, Hofmans et al. [43] discussed their admissibility, by investigating an experimental set-up of a larynx model. The conclusion was that turbulence effects take too long to develop. It needs to be pointed out that the VFs were rigid and to emulate their vibration effect on the flow an unsteady pressure drop across in- and outlet was set. With a more sophisticated experiment which fully regards the FSI by using VFs made out of polyurethane, Becker et al. [9] were able to observe downstream eddies which influence the flow upstream and inflict deflection of the glottal jet. In the case of numerical simulation, Zheng et al. [103] thoroughly examined the jet deflection by employing a 2D finite-difference method and a sharp-interface immersed-boundary method to impose the prescribed vocal fold motion as a boundary condition. Nevertheless, certain simplifications of the flow field still remain valid as they provide the possibility to observe and analyse specific effects. This is demonstrated by the work of Bae and Moon [7], who uses a symmetry assumption and are thereby able to significantly reduce the number of unknowns for their finite-difference formulation of the incompressible NSE. They also repli-

cated the VF motion from an axisymmetric model, which was incorporated into the simulation with a moving mesh methodology. The results of the glottal wave form were in good agreement with those of Rothenberg [75], who measured the volume velocity at the mouth and used an inverse filter to acquire the glottal volume flow. Bae and Moon [7] additionally computed the acoustic field using the perturbed compressible equations and found that the motion of the VFs from the divergence to the convergence position increases the acoustic efficiency as it controls the glottal impedance.

Concerning pure fluid mechanics in phonation, methods and studies have been designed by Decker and Thomson [22] with rigid VFs and induced movement by Alipour and Scherer [1] and Šidlof et al. [95]. Also using prescribed VFs movement, Schwarze et al. [79] used the finite-volume code *OpenFOAM* to simulate the laryngeal flow based on an experimental set-up suggested by Triep and Brücker [91]. It differs from other models as a result of its elliptic glottal opening. This feature was further analysed by Mattheus and Brücker [66], who compared the elliptic glottal opening to a 2D model and a 2D extruded model. Their findings revealed, that the elliptic opening forced the glottal jet to be symmetrical, whereas a slit-like opening skewed the jet towards one side of the laryngeal wall, demonstrating the importance of 3D fluid simulation and 3D geometry. Pure flow simulation neglects the energy exchange between the air flow (fluid) and the vocal fold vibration (structure) which, under certain conditions, could lead to false assumptions as described by Zörner et al. [105]. Based on a higher order 2D finite difference method, a 2D fully coupled FSI model was presented by Larsson and Müller [58]. Starting with an abstract channel and a symmetry assumption, Mittal et al. [68] illustrates his 3D flow model. In a further development by Luo et al. [64], Zheng et al. [102], the finite-different model was replaced by the FVM and the immersed boundary was devised to couple the FSI. This tool is then used to analyse vocal fold vibration and flow structure (Zheng et al. [104]), revealing a divergent-convergent vibrating pattern with physiological realistic amplitudes for the VFs and demonstrating that the glottal jet deflection is a result of downstream flow structures. By further extending the model using the linearised perturbation compressible equation to

additionally solve the acoustics and including the vocal tract and propagation region, Seo and Mittal [80] were capable of simulating the sound field leaving the mouth. An earlier work on FSAI methods was introduced by Link et al. [62], who adopted a 2D FE approach, which was extended by Zörner et al. [105] to analyse the effects of different interface and boundary conditions.

Focusing on the analysis of the acoustic sources and their origin, Zhao et al. [100] and Zhao et al. [101] presented their incompressible NSE model on a 2D axisymmetric geometry. To characterise the different sources, they used the analogy of Ffowcs-Williams-Hawkings. They concluded that the main source is a dipole source, induced by the net force exerted by the surface of the vocal folds onto the fluid. They determine that the axisymmetric assumption prevents the generation of turbulence and the glottis form is assumed to be circular. In an acoustic investigation on a 2D quasi static glottal model in converging and diverging state, Suh and Frankel [83] found that turbulence actually has an additional indirect effect on the acoustics by affecting the flow field and thereby modifying the main jet.

For an extensive review of the different numeric approaches for the continuum mechanical model of human phonation, the reader is referred to the work by Alipour et al. [3].

1.3.3 Material parameter measurement

Material parameters of the VFs have either not yet been measured or remain uncertain due to inconsistent measuring results ([3]). However, acquiring accurate data is important for a number of different reasons. From a medical perspective it would be interesting to fabricate artificial VFs with the correct parameters. This could also be used in experimental phonation research ([9]) to manufacture a larynx imitation – currently moulded out of silicone or polyurethane. In numerical simulation these material parameters define the model parameters. Furthermore, investigating the VFs texture will also reveal the geometrical decomposition of the VFs as it consists of different layers ([89]). In addition, understanding the structure may provide better insight into the complex VFs

movement. Therefore, the methods known to determine VF parameters are covered briefly and a method derived from these classic approaches is considered in detail in chapter 3.

Several studies have been made to investigate laryngeal material parameters. In [4, 5], excised canine vocal folds were stretched and released with the help of an ergometer, making it possible to determine the elasticity modulus. The ergometer operated at frequencies between 0.1 Hz and 10 Hz. To determine the material parameters, shear modulus, viscous shear modulus and dynamic viscosity rheometers were applied by [17, 37, 42, 90]. However, these investigations were limited to low frequencies. Theoretical prediction ([14, 15]) and extrapolation analysis ([17]) has been used to characterize the viscoelastic behaviour of the vocal folds in the frequency range of human phonation. In [16] a first approach to determine viscoelastic properties of vocal folds up to around 250 Hz can be found, where the authors based their experimental set-up on a shear rheometer.

CHAPTER 2

Governing equations and their FE-formulation

In the following chapter, the basic equations of fluid mechanics (section 2.1), solid mechanics (section 2.2) and acoustics (section 2.4) are derived. This results, in a number of PDEs, which are then put into a finite element formulation in order to solve them numerically. Additionally, the different coupling terms between the physical fields are presented and included into the numerical scheme. Any necessary treatments, such as stabilisation terms, are included difficulties arising from convection dominant problems. The chapter only gives an overview with the aim of providing a summary of all methods used for simulation. For a more detailed discussion and derivation of the equations, relevant references will be provided in each section.

2.1 Fluid mechanics

2.1.1 Spatial reference systems

A spatial reference system defines how the motion of a continuum is described i.e., from which perspective an observer views the matter. In a Lagrangian frame of reference, the observer monitors the trajectory in space of each material point and measures its physical quantities. This can be understood by considering a measuring probe which moves together with the material, like a boat on a river. The advantage is that free or moving boundaries can be captured easily as they require no special effort. Therefore, the approach is suitable in the case of structural mechanics. The limitation of this approach is confronted when dealing with large deformation, as in the case of fluid dynamics. In this case, a better choice is the Eulerian frame of reference, in which the observer monitors a single point in space when measuring physical quantities – the measuring probe stays at a fixed position in space. However, contrary to the Lagrangian approach, difficulties arise with deformations on the domain boundary, e.g., free boundaries and moving interfaces.

Formally, a deformation of a material body \mathcal{B} is defined as a map ψ , which projects each point \mathbf{X} at time $t \in \mathbb{R}$ to its current location \mathbf{x} , in mathematical terms

$$\mathbf{x} = \psi(\mathbf{X}, t), \quad \psi : \mathcal{B} \times \mathbb{R} \rightarrow \mathbb{R}^3 \quad .$$

By coupling structural and fluid mechanics, the different reference systems collide. Hughes et al. [46] presented the first method to solve the problem for an incompressible, viscous fluid in a FE context. The so called Arbitrary-Lagrangian-Eulerian (ALE) method combined the advantages of both approaches. The concept is that the observer is neither fixed nor does he move together with the material. Instead, he can move “arbitrarily”. Between each of the two reference systems a bijective mapping of the spatial variables \mathbf{x} (Eulerian system), \mathbf{X} (Lagrangian system) and $\boldsymbol{\chi}$ (ALE system) exists, as illustrated in Fig. 2.1. The choice of ref-

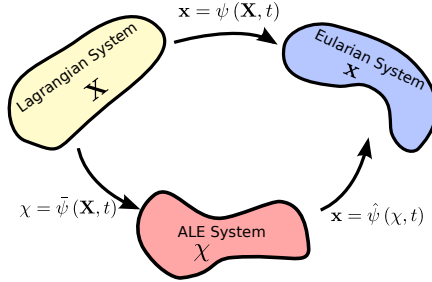


Figure 2.1: Illustration of mapping between reference systems.

reference system effects the PDEs through its time derivative. Exemplified for a quantity f and its velocity \mathbf{v} , the total derivative results for the

- Lagrangian system to

$$\frac{Df}{Dt} = \left. \frac{\partial f}{\partial t} \right|_{\mathbf{x}}$$

- Eulerian system to

$$\frac{Df}{Dt} = \underbrace{\left. \frac{\partial f}{\partial t} \right|_{\mathbf{x}}}_{\text{local change}} + \underbrace{(\mathbf{v} \cdot \nabla_{\mathbf{x}}) f}_{\text{convective change}}$$

- ALE system to

$$\frac{Df}{Dt} = \left. \frac{\partial f}{\partial t} \right|_{\mathbf{x}} + (\mathbf{v}_c \cdot \nabla_{\chi}) f, \quad (2.1)$$

with the convective velocity $\mathbf{v}_c = \mathbf{v} - \mathbf{v}_g$, the difference between material velocity \mathbf{v} and grid velocity \mathbf{v}_g .

Reynolds' transport theorem

To derive the integral form of the balance equations, recasting derivatives of integrated scalar or vectorial quantities is beneficial. This is known as the Reynolds' transport theorem.

Considering a scalar quantity $f(\mathbf{x}, t) : \Omega \times \mathbb{R} \rightarrow \mathbb{R}$, the change in time in a Lagrangian system of its volume integral

$$F(t) := \int_{\Omega(t)} f(\mathbf{x}, t) \, d\mathbf{x} \quad (2.2)$$

is given as

$$\frac{D}{Dt} F(t) = \frac{D}{dt} \int_{\Omega_L} f(\mathbf{X}, t) \, d\mathbf{X} = \int_{\Omega_L} \frac{\partial}{\partial t} f(\mathbf{X}, t) \, d\mathbf{X}. \quad (2.3)$$

The simple transformation is due to the linearity of the integral and differential operators. And since the Lagrangian domain Ω_L conforms with the material movement, no additional terms follow.

In an Eulerian context, time derivation must also take the time dependent domain $\Omega(t)$ into account by adding a surface flux term, which can be formulated as a volume term using the Gauß integral theorem. This results in

$$\begin{aligned} \frac{D}{dt} \int_{\Omega(t)} f \, d\mathbf{x} &= \int_{\Omega(t)} \frac{\partial}{\partial t} f \, d\mathbf{x} + \int_{\Gamma(t)} f \mathbf{v} \cdot \mathbf{n} \, d\mathbf{x} \\ &= \int_{\Omega(t)} \left(\frac{\partial}{\partial t} f + \nabla \cdot (f \mathbf{v}) \right) \, d\mathbf{x}. \end{aligned} \quad (2.4)$$

Here f stands for $f(\mathbf{x}, t)$, the same applies for \mathbf{v} , and \mathbf{n} is the outward pointing normal. The ALE Reynolds' transport theorem is derived analogously to (2.1).

2.1.2 Navier-Stokes equations

Conservation of mass

The Mass M of a body is the volume integral of the density ρ_f ,

$$M = \int_{\Omega(t)} \rho_f(\mathbf{x}, t) \, d\mathbf{x}. \quad (2.5)$$

Mass conservation states that the mass of a body is conserved over time, assuming there is no source or drain. The derivation of mass conservation is presented, using the example of a fluid. What holds for the entire fluid, also holds for all the single fluid element masses m_i , and can be expressed as

$$\frac{DM}{Dt} = \sum_i \frac{Dm_i}{Dt} = 0. \quad (2.6)$$

In a Eulerian system, inserting (2.5) in equation (2.6), and exploiting Reynolds' transport theorem (2.4), leads to

$$\begin{aligned} \frac{Dm_i}{Dt} &= \int_{\Omega_i} \frac{\partial}{\partial t} \rho_f \, d\mathbf{x} + \int_{\Gamma_i} \rho_f \mathbf{v} \cdot \mathbf{n} \, d\mathbf{x} \\ &= \int_{\Omega_i} \frac{\partial}{\partial t} \rho_f + \nabla \cdot (\rho_f \mathbf{v}) \, d\mathbf{x} = 0. \end{aligned} \quad (2.7)$$

With the help of Fig. 2.2, which depicts a single fluid element, the first equality can be understood in the following way: In a Eulerian system the domain Ω_i remains constant, whereas the element mass m_i can change position and volume. Therefore, to compensate for compression and decompression, the mass flux over the fluid element is introduced, which is expressed by the boundary integral in (2.7).

The integral in (2.7) can be dismissed, as it holds for arbitrary Ω_i and in the special case of an incompressible fluid ($\rho_f = \text{const.} \quad \forall(\mathbf{x}, t) \in \Omega \times \mathbb{R}$), which may be assumed for low Mach numbers, the time and space derivative of the density vanishes. This leads to the following form of mass

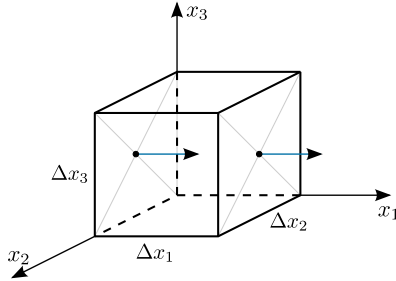


Figure 2.2: Fluid element, with vectors indicating fluid flux.

conservation equations

$$\begin{aligned} \frac{\partial}{\partial t} \rho_f + \nabla \cdot (\rho_f \mathbf{v}) &= 0 && \text{(compressible fluid),} \\ \nabla \cdot \mathbf{v} &= 0 && \text{(incompressible fluid).} \end{aligned} \quad (2.8)$$

Conservation of momentum

The equation of momentum is implied by Newton's second law and states that momentum \mathbf{I} is the product of mass m and velocity \mathbf{v} ($\mathbf{I} = m\mathbf{v}$). Derivation in time gives the rate of change of momentum, which is equal to the force \mathbf{F} and reveals the relation to Newton's second law in a Eulerian reference system,

$$\mathbf{F} = \frac{D\mathbf{I}}{Dt} = \frac{D}{Dt}(m\mathbf{v}) = \frac{\partial}{\partial t}(m\mathbf{v}) + \nabla \cdot (m\mathbf{v} \otimes \mathbf{v}), \quad (2.9)$$

where $\mathbf{v} \otimes \mathbf{v}$ is a tensor defined by the dyadic product \otimes . The last equality in (2.9) is derived from Reynolds transport theorem (2.4) and mass conservation (2.8). For a Lagrangian reference system it would result in $\mathbf{F} = m\mathbf{a}$. Forces \mathbf{F} acting on fluids can be split up into forces acting on the surface of the body \mathbf{f}_Γ , forces due to momentum of the molecules

2 Governing equations and their FE-formulation

$\frac{D}{Dt}\mathbf{I}_m$ and external forces \mathbf{f} (e.g. gravity, electromagnetic forces). In mathematical terms

$$\mathbf{F} = \mathbf{f}_\Gamma + \frac{D}{Dt}\mathbf{I}_m + \mathbf{f}. \quad (2.10)$$

Fluids are characterised by the fact that only surface forces act on a fluid element as a result of molecular pressure, as depicted in Fig. 2.3. Considering the surface forces \mathbf{f}_{Γ_j} pointing in the j -direction, and the

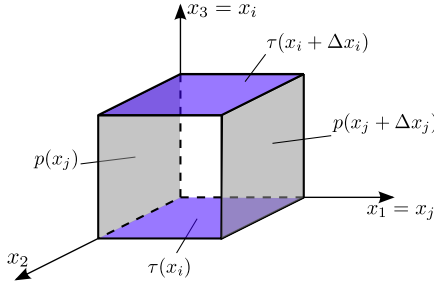


Figure 2.3: Forces acting on a fluid element.

Γ_j which are orthogonal to the normal \mathbf{n}_j , results in the acting pressure forces

$$\mathbf{f}_{\Gamma_j} = p(x_j)|\Gamma_j|\mathbf{n}_j - p(x_j + \Delta x_j)|\Gamma_j|\mathbf{n}_j. \quad (2.11)$$

Using the Taylor series

$$p(x_j + \Delta x_j) = p(x_j) + \frac{\partial p}{\partial x_j}\Delta x_j + \mathcal{O}(2), \quad (2.12)$$

disregarding higher order terms and inserting it into (2.11) gives

$$\mathbf{f}_{\Gamma_j} = p(x_j)|\Gamma_j|\mathbf{n}_j - \left(p(x_j) + \frac{\partial p}{\partial x_j}\Delta x_j \right) |\Gamma_j|\mathbf{n}_j. \quad (2.13)$$

Simplifying (2.13) and adding up all forces in each space direction results

in

$$\sum_{i=1}^3 \mathbf{f}_{\Gamma_j} = - \sum_{i=1}^3 \frac{\partial p}{\partial x_j} |\Omega| \mathbf{n}_j = - |\Omega| \nabla p. \quad (2.14)$$

The second term in (2.10) is the momentum of the molecules per time unit. Introducing the tensor $\boldsymbol{\tau}$ with entries τ_{ij} , with the indices denoting the j -impulse in i th-direction as shown in Fig. 2.3, the derivation begins in the same way as for the surface force in (2.11)

$$\frac{D}{Dt} \mathbf{I}_m = -\tau_{ij}(x_i) |\Gamma_i| \mathbf{n}_j + \tau_{ij}(x_i + \Delta x_i) |\Gamma_i| \mathbf{n}_j. \quad (2.15)$$

Using the same techniques (Taylor series etc.) as for the surface forces leads to

$$\frac{D}{Dt} \mathbf{I}_m = \nabla \cdot \boldsymbol{\tau} |\Omega|. \quad (2.16)$$

By exploiting the fact that $m = |\Omega| \rho_f$ and inserting the surface force (2.14), the viscous force (2.16) and any outer forces per unit volume \mathbf{f}_Ω acting on the fluid into (2.9) we obtain the momentum equation

$$\rho_f \frac{\partial}{\partial t} (\mathbf{v}) + \rho_f (\mathbf{v} \cdot \nabla) \mathbf{v} = -\nabla p + \nabla \cdot [\boldsymbol{\tau}] + \mathbf{f}_\Omega. \quad (2.17)$$

To determine the viscous stress tensor $[\boldsymbol{\tau}]$, empirical data is necessary, which according to Stokes is found to be

$$\tau_{ij} = 2\mu \epsilon_{ij} + \lambda \epsilon_{ii} \delta_{ij}, \quad (2.18)$$

with the dynamic viscosity μ and the strain rate ϵ

$$\epsilon_{ij} = \frac{1}{2} \left(\frac{\partial v_i}{\partial x_j} + \frac{\partial v_j}{\partial x_i} \right). \quad (2.19)$$

According to Stokes hypothesis ($\lambda = -2/3\mu$) (2.18) can be rewritten as

$$\tau_{ij} = \mu \left(\frac{\partial v_i}{\partial x_j} + \frac{\partial v_j}{\partial x_i} \right) - \frac{2}{3} \mu (\nabla \cdot \mathbf{v}) \delta_{ij}. \quad (2.20)$$

Navier-Stokes equations

Inserting (2.20) in (2.17) and including the mass conservation (2.8), reveals the more common notation of the compressible Navier-Stokes equations:

$$\begin{aligned} \rho_f \frac{\partial}{\partial t} \mathbf{v} + \rho_f (\mathbf{v}_c \cdot \nabla) \mathbf{v} + \nabla p - \mu \Delta \mathbf{v} - \frac{1}{3} \mu \nabla \nabla \cdot \mathbf{v} &= \mathbf{f}_\Omega \\ \frac{\partial \rho_f}{\partial t} + \nabla \cdot (\rho_f \mathbf{v}) &= 0, \end{aligned} \quad (2.21)$$

with the ALE reference system correction term \mathbf{v}_c , as defined in equation (2.1). Since the equations of mass and momentum conservation in (2.21) consist of more unknowns than equations, boundary conditions, the equations of state and conservation of energy (see [26]) need to be included to define a well-posed problem. Alternatively, under the condition of low Mach number flow (see Tab. 2.1)

$$\text{Ma} = \frac{\|\mathbf{v}\|}{c}. \quad (2.22)$$

Incompressibility may be assumed, which simplifies (2.21) to

$$\begin{aligned} \frac{\partial}{\partial t} \mathbf{v} + (\mathbf{v}_c \cdot \nabla) \mathbf{v} + \nabla P - \nu \Delta \mathbf{v} &= \mathbf{0} \\ \nabla \cdot \mathbf{v} &= 0, \end{aligned} \quad (2.23)$$

with the kinematic viscosity $\nu = \mu/\rho_f$, kinematic pressure $P = p/\rho_f$ and outer forces $\mathbf{f}_\Omega = \mathbf{0}$. During normal speech, an incompressibility assumption is legitimate ([89, p. 240]) and is therefore used to model the flow inside the larynx¹.

For the sake of completeness, the whole set of incompressible NSE, to-

¹Other types of human phonation, e.g., singing, may cause a back reaction of acoustics onto the flow field, due to the high velocities, in which case an incompressible flow assumption is not correct.

$\text{Ma} < 0.3$	incompressible flow
$\text{Ma} < 1$	subsonic
$\text{Ma} \approx 1$	sonic (trans sonic)
$\text{Ma} > 1$	supersonic
$\text{Ma} \gg 1$	hyper sonic

Table 2.1: Classification of flow by its Mach number Ma .

gether with boundary conditions, is given as

$$\frac{\partial}{\partial t} \mathbf{v} + (\mathbf{v}_c \cdot \nabla) \mathbf{v} + \nabla P - \nu \Delta \mathbf{v} = \mathbf{0} \quad \text{in } \Omega \times \mathbb{R}, \quad (2.24a)$$

$$\nabla \cdot \mathbf{v} = 0 \quad \text{in } \Omega \times \mathbb{R}, \quad (2.24b)$$

$$\mathbf{v} = \mathbf{v}_0 \quad \text{on } \Gamma_{D_V} \times \mathbb{R}, \quad (2.24c)$$

$$P = P_0 \quad \text{on } \Gamma_{D_P} \times \mathbb{R}, \quad (2.24d)$$

$$\boldsymbol{\sigma}_f \cdot \mathbf{n} = \mathbf{h} \quad \text{on } \Gamma_N \times \mathbb{R}. \quad (2.24e)$$

The boundary conditions given in (2.24) are divided up into Dirichlet boundary conditions for velocity and pressure, (2.24c) and (2.24d) respectively, and a Neumann condition (2.24e). Here, $\partial\Omega = \Gamma_{D_V} \cup \Gamma_{D_P} \cup \Gamma_N$ and the boundaries are disjointed.

Example: Consider a channel flow which is driven by a pressure gradient. The domain consists of the inlet boundary Γ_I , the outlet Γ_O and the walls of the channel Γ_W . At the inlet the pressure would be set to a fixed value P_0 and at the outlet to zero. As the fluid adheres to the channel walls, no-slip conditions are given by using homogeneous Dirichlet conditions for the velocity.

A detailed derivation of the NSE is presented by Durst [26], which also covers the equations of state and conservation of energy necessary for solving the compressible NSE.

2.1.3 Finite element formulation

Solving the NSE requires a numerical scheme. The finite volume method FVM is commonly used as it, among other properties, implicitly preserves mass conservation. However, when it comes to higher order methods, the FVM is generally unsuited as it becomes overly complex. In contrast, the FEM generally does not require any special treatment for higher order approximation.

In a first step of the FEM, the strong form of the problem (2.24) is transformed into a variation formulation. This requires a function space with an inner product, termed a Hilbert space. A first choice is the Lebesgue space $L^2(\Omega_f)$, defined on the fluid domain Ω_f , with the inner product

$$(p, \varphi) = \int_{\Omega_f} p\varphi \, dx \quad \text{with } p, \varphi \in L^2(\Omega_f). \quad (2.25)$$

In words, it is the space of square integrable functions defined on Ω_f . Since (2.24) also contains derivatives, the Hilbert space $H^n(\Omega_f)$ is introduced, which additionally demands that the n -th order derivatives of a function are also in $L^2(\Omega_f)$.

In the case of the NSE, the following function spaces are required

$$\begin{aligned} \mathcal{V} &= \{\boldsymbol{\omega} \in H_0^2(\Omega_f)\}, \\ \mathcal{P} &= \{\varphi \in L_0^2(\Omega_f)\}. \end{aligned}$$

Subscript “0” denotes that the functions have a compact support (see Appendix B). The unknown variables \mathbf{v} , P and their according test functions $\boldsymbol{\omega}$ and φ , are of the respective function space – $\mathbf{v}, \boldsymbol{\omega} \in \mathcal{V}$ and $P, \varphi \in \mathcal{P}$.

Remark: It would be sufficient for the velocity field \mathbf{v} and its test function $\boldsymbol{\omega}$ to be in $H_0^1(\Omega_f)$, but the stabilisation method (see section 2.1.4) requires weak second derivatives, which will be discussed in the next section. A detailed explanation on function spaces and partial differential equations can be found by Evans [31].

The variational form changes the original problem to finding a unique

$\mathbf{v} \in \mathcal{V}$ and $P \in \mathcal{P}$ such that for all $\boldsymbol{\omega} \in \mathcal{V}$ and $\varphi \in \mathcal{P}$ following holds

$$\begin{aligned} (\partial_t \mathbf{v}, \boldsymbol{\omega}) + ((\mathbf{v}_c \cdot \nabla) \mathbf{v}, \boldsymbol{\omega}) - (\nabla P, \boldsymbol{\omega}) + \nu (\Delta \mathbf{v}, \boldsymbol{\omega}) &= 0, \\ (\nabla \cdot \mathbf{v}, \varphi) &= 0. \end{aligned} \quad (2.26)$$

By applying the integral theorem of Gauss, the pressure term $(\nabla P, \boldsymbol{\omega})$ and diffusive term $\nu (\Delta \mathbf{v}, \boldsymbol{\omega})$ in (2.26) become

$$\begin{aligned} -(\nabla P, \boldsymbol{\omega}) + \nu (\Delta \mathbf{v}, \boldsymbol{\omega}) &= \\ - \int_{\Omega_f} P \nabla \cdot \boldsymbol{\omega} \, dx + \nu \sum_i \int_{\Omega_f} \frac{\partial}{\partial x_i} v_i \frac{\partial}{\partial x_i} \omega_i \, dx - \int_{\Gamma_N} \mathbf{h} \cdot \boldsymbol{\omega} \, dx. \end{aligned} \quad (2.27)$$

To simplify the notation, the differential operator \mathcal{I} for the momentum conservation (*ger.*: Impuls) and \mathcal{M} for the mass conservation are defined as

$$\begin{aligned} \mathcal{I}(\mathbf{v}, \boldsymbol{\omega}, P) &= (\partial_t \mathbf{v}, \boldsymbol{\omega}) + ((\mathbf{v}_c \cdot \nabla) \mathbf{v}, \boldsymbol{\omega}) \\ &\quad - (P, \nabla \cdot \boldsymbol{\omega}) + \nu (\overline{\nabla} \mathbf{v}, \overline{\nabla} \boldsymbol{\omega}) = (\mathbf{h}, \boldsymbol{\omega})_{\Gamma_N} \\ \mathcal{M}(\mathbf{v}, \varphi) &= (\nabla \cdot \mathbf{v}, \varphi) = 0, \end{aligned} \quad (2.28)$$

with the vector-valued differential operator

$$\overline{\nabla} \mathbf{v} := \sum_i \frac{\partial}{\partial x_i} \mathbf{v} \mathbf{e}_i,$$

\mathbf{e}_i being the unit vector in direction i .

After the variational formulation has been established, the next step in the FEM is to replace the infinite function spaces $(\mathcal{V}, \mathcal{P})$ by their finite dimensional subspaces $(\mathcal{V}_h, \mathcal{P}_h)$. Here the unknowns were approximated

in the following way

$$\mathbf{v} \approx \mathbf{v}_h := \sum_j v_j \boldsymbol{\omega}_h,$$
$$P \approx P_h := \sum_j P_j \varphi_h.$$

The approximating functions $\boldsymbol{\omega}_h$ and φ_h are called shape functions. Converting the weak formulation, a continuous problem, into a discrete problem is called Galerkin method. Further details, analysis and error estimations of the Galerkin method can be found in Hughes [45], Braess [12] and for application in engineering Kaltenbacher [54]. They also cover, space and time discretisation, non-linear and linear solvers, which is also examined by Schwarz and Köckler [78].

2.1.4 SUPG method

For convective transport problems, the FEM becomes unstable unless the exact solution happens to be globally smooth. In the case of the NSE, this occurs for high velocities (i.e. high Reynolds numbers), resulting in a convective dominant problem or $(\mathbf{v} \cdot \nabla)\mathbf{v} \gg \Delta\mathbf{v}$. A straightforward approach is to severely refine the mesh, such that convection is not dominant at an element level. If global features of the flow are sufficient, upwinding is an alternative method, as has been established for finite difference methods. In FEM, this is called Petrov-Galerkin scheme, and is accomplished by choosing the test functions from a different function space than that of the field variables. The idea behind it is to weight the test function so that the path of the flow, and thereby the direction of information, is considered. This results in artificial diffusion in the direction perpendicular to the flow, which has been criticised as it misrepresents the physical transport process ([20, 39]). Therefore, Brooks and Hughes [13] presented the Streamline-Upwind-Petrov-Galerkin method, or SUPG method, to circumvent the cross-stream diffusion by considering only upwinding with streamline direction. This is achieved by enriching the test

function ω with an upwinding term resulting in

$$\hat{\omega} = \omega + \alpha (\mathbf{v}_c \cdot \nabla) \omega. \quad (2.29)$$

A further instability is induced by the pressure, which causes pressure oscillations. Hansbo and Szepessy [41] and Tezduyar et al. [85] both independently combined pressure stabilisation with the SUPG method, forming the SUPG/PSPG (pressure stabilisation Petrov-Galerkin). Thereby, the test function is further enriched with the test function of the pressure and the pressure test function is also enriched, resulting in

$$\tilde{\omega} = \omega + \alpha_M ((\mathbf{v}_c \cdot \nabla) \omega + \nabla \varphi), \quad (2.30)$$

$$\tilde{\varphi} = \varphi + \alpha_C \nabla \cdot \omega. \quad (2.31)$$

α_M and α_C are stabilisation parameters which need to be set appropriately. In the current work focusing on simulating the human phonation process with quadrilateral elements, the parameter values according to Wall [96] have proven to be effective

$$\alpha_M = \frac{h_K}{2\|\mathbf{v}\|_2} \zeta \quad \text{and} \quad \alpha_C = \frac{\|\mathbf{v}\|_2 h_K}{2} \zeta. \quad (2.32)$$

$\|\cdot\|_2$ denotes the L_2 -norm, h_K the characteristic element length (e.g. edge length) and ζ is defined as

$$\zeta = \begin{cases} Re_K, & 0 \leq Re_K < 1 \\ 1, & Re_K \geq 1 \end{cases},$$

with the element Reynolds number

$$Re_K := \frac{\|\mathbf{v}\|_2 h_K}{24\nu}.$$

A brief overview of different works on the choice of stabilisation parameters has been performed by Wall [96].

To summarise, the NSE with stabilisation terms result in

$$\begin{aligned}
 \mathcal{I}_h(\mathbf{v}, \boldsymbol{\omega}, P, \varphi) &= (\partial_t \mathbf{v}, \boldsymbol{\omega}) + ((\mathbf{v}_c \cdot \nabla) \mathbf{v}, \boldsymbol{\omega}) - (P, \nabla \cdot \boldsymbol{\omega}) + \nu (\overline{\nabla} \mathbf{v}, \overline{\nabla} \boldsymbol{\omega}) \\
 &\quad + \alpha_M (\partial_t \mathbf{v}, (\mathbf{v}_c \cdot \nabla) \boldsymbol{\omega}) + \alpha_M ((\mathbf{v}_c \cdot \nabla) \mathbf{v}, (\mathbf{v}_c \cdot \nabla) \boldsymbol{\omega}) \\
 &\quad + \alpha_M (\nabla P, (\mathbf{v}_c \cdot \nabla) \boldsymbol{\omega}) + \alpha_M \nu (\Delta \mathbf{v}, (\mathbf{v}_c \cdot \nabla) \boldsymbol{\omega}) \\
 &\quad + \alpha_M (\partial_t \mathbf{v}, \nabla \varphi) + \alpha_M ((\mathbf{v}_c \cdot \nabla) \mathbf{v}, \nabla \varphi) \\
 &\quad + \alpha_M (\nabla P, \nabla \varphi) + \alpha_M \nu (\Delta \mathbf{v}, \nabla \varphi) \\
 &= (\mathbf{h}, \boldsymbol{\omega})_{\Gamma_N} \\
 \mathcal{M}_h(\mathbf{v}, \boldsymbol{\omega}, \varphi) &= (\nabla \cdot \mathbf{v}, \varphi) + \alpha_C (\nabla \cdot \mathbf{v}, \nabla \cdot \boldsymbol{\omega}) = 0.
 \end{aligned}$$

By summing up momentum and mass conservation, the equations can be transformed into a non-linear matrix vector notation

$$\mathbf{M}(\mathbf{v}_h) \partial_t \mathbf{v}_h + \mathbf{N}(\mathbf{v}_h) \mathbf{v}_h + \mathbf{G}(\mathbf{v}_h) \mathbf{P}_h = \mathbf{F}, \quad (2.33)$$

with matrices \mathbf{M} , \mathbf{N} and \mathbf{G} defined as

$$\begin{aligned}
 \mathbf{M}(\mathbf{v}_h) \partial_t \mathbf{v}_h &= (\partial_t \mathbf{v}, \boldsymbol{\omega}) + \alpha_M (\partial_t \mathbf{v}, (\mathbf{v}_c \cdot \nabla) \boldsymbol{\omega}) + \alpha_M (\partial_t \mathbf{v}, \nabla \varphi) \\
 \mathbf{N}(\mathbf{v}_h) \mathbf{v}_h &= ((\mathbf{v}_c \cdot \nabla) \mathbf{v}, \boldsymbol{\omega}) + \nu (\overline{\nabla} \mathbf{v}, \overline{\nabla} \boldsymbol{\omega}) + \alpha_M \nu (\Delta \mathbf{v}, (\mathbf{v}_c \cdot \nabla) \boldsymbol{\omega}) \\
 &\quad + \alpha_M ((\mathbf{v}_c \cdot \nabla) \mathbf{v}, (\mathbf{v}_c \cdot \nabla) \boldsymbol{\omega}) + \alpha_M ((\mathbf{v}_c \cdot \nabla) \mathbf{v}, \nabla \varphi) \\
 &\quad + \alpha_M \nu (\Delta \mathbf{v}, \nabla \varphi) - (\nabla \cdot \mathbf{v}, \varphi) - \alpha_C (\nabla \cdot \mathbf{v}, \nabla \cdot \boldsymbol{\omega}) \\
 \mathbf{G}(\mathbf{v}_h) \mathbf{P}_h &= - (P, \nabla \cdot \boldsymbol{\omega}) + \alpha_M (\nabla P, (\mathbf{v}_c \cdot \nabla) \boldsymbol{\omega}) + \alpha_M (\nabla P, \nabla \varphi) \\
 \mathbf{F} &= (\mathbf{h}, \boldsymbol{\omega})_{\Gamma_N}.
 \end{aligned}$$

2.1.5 Time discretisation and linearisation

The 2nd order backward difference formula (BDF2) has been shown to be reliable in combination with the NSE, as it has low numerical dissipation, is A-stable and even L-stable according to Hairer et al. [40]. Error estimates and stability analysis in combination with NSE have been per-

formed by Emmrich [28, 29].

By approximating the time derivative in (2.33) with the *BDF2*, we obtain the following non-linear system

$$\begin{aligned} \left(\mathbf{M}(\mathbf{v}_h^{n+1}) + \frac{2}{3}\Delta t \mathbf{N}(\mathbf{v}_h^{n+1}) \right) \mathbf{v}_h^{n+1} + \frac{2}{3}\Delta t \mathbf{G}(\mathbf{v}_h^{n+1}) \mathbf{P}_h^{n+1} \\ = \frac{2}{3}\Delta t \mathbf{F} + \mathbf{M}(\mathbf{v}_h^{n+1}) \left(\frac{4}{3}\mathbf{v}_h^n - \frac{1}{3}\mathbf{v}_h^{n-1} \right) \end{aligned} \quad (2.34)$$

with, the fixed time step size Δt and the superscripts $n+1$, n , $n-1$ denoting new, current and old time steps, respectively. For the right hand side \mathbf{F} , dependency on time is implied, as it is considered to be known.

For the non-linear term $((\mathbf{v} \cdot \nabla)\mathbf{v}, \tilde{\boldsymbol{\omega}})$, the Newton method (also known as the Newton-Raphson method) is applied. For (2.34) this is given by

$$\begin{aligned} \left(\mathbf{M}(\mathbf{v}_k^{n+1}) + \frac{2}{3}\Delta t \mathbf{J}_N(\mathbf{v}_k^{n+1}) \right) \mathbf{v}_{k+1}^{n+1} + \frac{2}{3}\Delta t \mathbf{G}(\mathbf{v}_k^{n+1}) \mathbf{P}_{k+1}^{n+1} \\ = -\frac{2}{3}\Delta t \mathbf{F} - \mathbf{M}(\mathbf{v}_k^{n+1}) \left(\frac{4}{3}\mathbf{v}_k^n - \frac{1}{3}\mathbf{v}_k^{n-1} \right) + \frac{2}{3}\Delta t \mathbf{J}_N(\mathbf{v}_k^{n+1}) \mathbf{v}_k^{n+1}. \end{aligned}$$

The subscripts h have been replaced with the Newton iteration step k and \mathbf{J}_N denotes the Jacobian of the vector valued function $[\mathbf{N}(\mathbf{v}_h^{n+1})\mathbf{v}_h^{n+1}]$. With the subscripts i and j denoting the row index of matrix and vector, the Jacobian of \mathbf{N} is defined as

$$\mathbf{J}_N(\mathbf{v}_h^{n+1}) := \left(\frac{\partial(N_i(\mathbf{v}_h^{n+1})\mathbf{v}_h^{n+1})}{\partial \mathbf{v}_j^{n+1}} \right)_{ij}. \quad (2.35)$$

Since matrices \mathbf{G} and \mathbf{M} are linear and not constant, they coincide with their Jacobian. When a sufficient error bound $\varepsilon_{\text{Newton}}$ is reached, calculated by

$$\frac{\|P_{k+1}^{n+1} - P_k^{n+1}\|_2}{\|P_{k+1}^{n+1}\|} + \frac{\|\mathbf{v}_{k+1}^{n+1} - \mathbf{v}_k^{n+1}\|_2}{\|\mathbf{v}_{k+1}^{n+1}\|} < \varepsilon_{\text{Newton}},$$

the Newton iteration stops and the next time step can be processed.

Remark: The stabilisation terms, and thereby the test functions, are velocity dependant ($(\mathbf{v}_c \cdot \nabla)\tilde{\omega}$) and can induce further non-linear terms, but these are not linearised. Instead, velocity values of the test function are computed based on the last Newton iteration step. This leads to a significant reduction in computational time, since matrices \mathbf{M} and \mathbf{G} are thereby linear. However, the quadratic convergence of the Newton method is thereby not achieved.

2.2 Solid mechanics

This section covers the equation of linear elasticity, including its weak formulation in order to put into context with the FEM. Firstly, a unit solid element as depicted in Fig. 2.4a is considered, then all forces, consisting of volume force \mathbf{f}_Ω and surface forces, sum to zero. This state of equilibrium also holds for any arbitrary solid element inside a structure. The force of a body over a surface is denoted by mechanical stress (force per area). For each face direction, the corresponding stress vectors $\boldsymbol{\sigma}_x$,

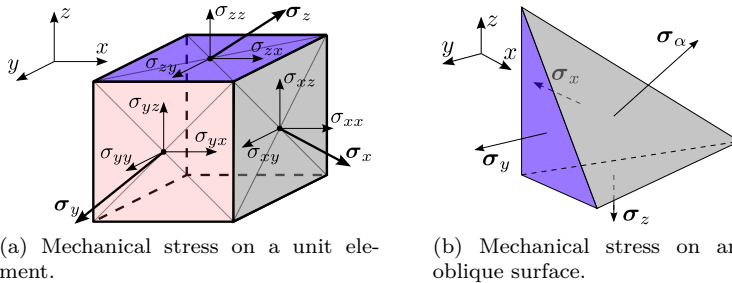


Figure 2.4: Mechanical stress $\boldsymbol{\sigma}$ on surfaces of a reference solid elements

$\boldsymbol{\sigma}_y$, $\boldsymbol{\sigma}_z$ are given by

$$\begin{aligned}\boldsymbol{\sigma}_x &= \sigma_{xx}\mathbf{e}_x + \sigma_{xy}\mathbf{e}_y + \sigma_{xz}\mathbf{e}_z, \\ \boldsymbol{\sigma}_y &= \sigma_{yx}\mathbf{e}_x + \sigma_{yy}\mathbf{e}_y + \sigma_{yz}\mathbf{e}_z, \\ \boldsymbol{\sigma}_z &= \sigma_{zx}\mathbf{e}_x + \sigma_{zy}\mathbf{e}_y + \sigma_{zz}\mathbf{e}_z,\end{aligned}\tag{2.36}$$

with the normal stresses $(\sigma_{xx}, \sigma_{yy}, \sigma_{zz})$, shear stresses σ_{ij} ($i \neq j$) and \mathbf{e}_i the unit vector in direction i . In general, looking at a oblique face of a reference system, schematically displayed in Fig. 2.4b, the equilibrium of force is given by

$$d\Gamma_\alpha \boldsymbol{\sigma}_\alpha - d\Gamma_x \boldsymbol{\sigma}_x - d\Gamma_y \boldsymbol{\sigma}_y - d\Gamma_z \boldsymbol{\sigma}_z = 0,\tag{2.37}$$

with the infinite small surfaces $d\Gamma$ labelled with the indices α, x, y, z . Defining the vector $\mathbf{n}_\alpha = (n_x, n_y, n_z)^T$, which is normal to $d\Gamma_\alpha$, it follows that

$$d\Gamma_x = d\Gamma_\alpha n_x, \quad d\Gamma_y = d\Gamma_\alpha n_y, \quad d\Gamma_z = d\Gamma_\alpha n_z,$$

and (2.37) can be rewritten as

$$\boldsymbol{\sigma}_\alpha = n_x \boldsymbol{\sigma}_x + n_y \boldsymbol{\sigma}_y + n_z \boldsymbol{\sigma}_z.$$

Using (2.36), the mechanical stress tensor $[\boldsymbol{\sigma}]$ is introduced

$$[\boldsymbol{\sigma}] = \begin{bmatrix} \sigma_{xx} & \sigma_{xy} & \sigma_{xz} \\ \sigma_{yx} & \sigma_{yy} & \sigma_{yz} \\ \sigma_{zx} & \sigma_{zy} & \sigma_{zz} \end{bmatrix},\tag{2.38}$$

and is termed the *Cauchy* stress tensor.

Considering the equation of translation

$$\int_{\Omega_s} \mathbf{f}_\Omega \, d\mathbf{x} + \int_{\Gamma} [\boldsymbol{\sigma}]^T \, d\mathbf{x} = 0,\tag{2.39}$$

applying the theorem of Gauss and removing the integral, as Ω_s can be

arbitrarily chosen, it follows that

$$\mathbf{f}_\Omega + \nabla[\boldsymbol{\sigma}] = 0. \quad (2.40)$$

As the Cauchy tensor is symmetric (see Appendix B) and using the Voigt notation (see Appendix B), (2.40) takes the following form

$$\mathcal{B}^T \boldsymbol{\sigma} + \mathbf{f}_\Omega = 0, \quad (2.41)$$

with the symmetric differential operator

$$\mathcal{B} = \begin{pmatrix} \frac{\partial}{\partial x} & 0 & 0 & 0 & \frac{\partial}{\partial z} & \frac{\partial}{\partial y} \\ 0 & \frac{\partial}{\partial y} & 0 & \frac{\partial}{\partial z} & 0 & \frac{\partial}{\partial x} \\ 0 & 0 & \frac{\partial}{\partial z} & \frac{\partial}{\partial x} & \frac{\partial}{\partial y} & 0 \end{pmatrix}^T.$$

For the dynamic system the forces are equal to the inertia forces, given by Newton's second law, and this results in Navier's equation

$$\mathcal{B}^T \boldsymbol{\sigma} + \mathbf{f}_\Omega = \rho_s \frac{\partial^2}{\partial t^2} \mathbf{u}. \quad (2.42)$$

Here, ρ_s denotes the density of the solid and \mathbf{u} the mechanical displacement.

Introducing the tensor of elasticity $[\mathbf{c}]$ and tensor of linear strain $[\mathbf{S}]$, allows us to express Hook's law by

$$\boldsymbol{\sigma} = [\mathbf{c}][\mathbf{S}], \quad (2.43)$$

the linear strain-displacement by

$$[\mathbf{S}] = \frac{1}{2} (\nabla \otimes \mathbf{u} + (\nabla \otimes \mathbf{u})^T), \quad (2.44)$$

and the elasticity tensor by

$$[\mathbf{c}] = \begin{pmatrix} \lambda_L + 2\mu_L & \lambda_L & \lambda_L & 0 & 0 & 0 \\ \lambda_L & \lambda_L + 2\mu_L & \lambda_L & 0 & 0 & 0 \\ \lambda_L & \lambda_L & \lambda_L + 2\mu_L & 0 & 0 & 0 \\ 0 & 0 & 0 & \mu_L & 0 & 0 \\ 0 & 0 & 0 & 0 & \mu_L & 0 \\ 0 & 0 & 0 & 0 & 0 & \mu_L \end{pmatrix}.$$

λ_L and μ_L are the Lamé parameters, which are determined by elasticity modulus E ($[E]=Pa$) and the dimensionless Poisson's ratio ν_P using the following equations

$$\lambda_L = \frac{\nu_P E}{(1 + \nu_P)(1 - 2\nu_P)}$$

$$\mu_L = \frac{E}{2(1 + \nu_P)}.$$

Substituting (2.43) and (2.44) into (2.42) results in the final PDE for linear elasticity

$$\mathcal{B}^T [c] \mathcal{B} \mathbf{u} + \mathbf{f}_\Omega = \rho_s \frac{\partial^2}{\partial t^2} \mathbf{u}. \quad (2.45)$$

For a more detailed description, Parkus [71] provides derivations of the basic laws of structural mechanics.

2.2.1 Finite element formulation

Equation (2.45) is discretised using the FEM, as for the NSE. To obtain the variational formulation, (2.45) is multiplied by an appropriate test function $\psi \in H_0^1(\Omega_s)$ and integrated over the computational domain Ω_s .

Integrating by parts then gives

$$\begin{aligned}
 - \int_{\Omega_s} [\mathbf{c}] \mathcal{B} \mathbf{u} \cdot \mathcal{B} \boldsymbol{\psi} \, dx + \int_{\Gamma_s} [\boldsymbol{\sigma}] \cdot \boldsymbol{\psi} \cdot \mathbf{n} \, dx + \int_{\Omega_s} \mathbf{f} \cdot \boldsymbol{\psi} \, dx = \\
 \int_{\Omega_s} \rho_s \frac{\partial^2}{\partial t^2} \mathbf{u} \cdot \boldsymbol{\psi} \, dx .
 \end{aligned} \tag{2.46}$$

The infinite-dimensional space is replaced by finite-dimensional subspace $V_h \subset H_0^1$ and the displacement is approximated by

$$\mathbf{u}(t, x) \approx \mathbf{u}_h(t, x) = \sum_{i=1}^N u_i(t) \boldsymbol{\psi}_i(x),$$

with $\{\boldsymbol{\psi}_1, \dots, \boldsymbol{\psi}_N\}$ a basis of V_h and N the number of FE nodes in the computational domain. With a suitable set of basis functions the test functions are chosen from this set, resulting in a matrix vector notation of (2.46)

$$\mathbf{M} \ddot{\mathbf{u}} + \mathbf{K} \mathbf{u} = \mathbf{f} . \tag{2.47}$$

In (2.47), \mathbf{M} denotes the mass matrix, \mathbf{K} the stiffness matrix, \mathbf{u} the discrete displacement with its second time derivative $\ddot{\mathbf{u}}$. \mathbf{f} denotes the right hand side, consisting of the given volume force \mathbf{f}_Ω , boundary values or interface conditions.

To solve the system of ordinary differential equations of 2nd order, due to the time derivative in (2.47), the Crank-Nicolson scheme is employed. This results in the approximation

$$\frac{1}{\Delta t^2} \mathbf{M} (\mathbf{u}^{n+1} - 2\mathbf{u}^n + \mathbf{u}^{n-1}) + \mathbf{K} \mathbf{u}^{n+1} = \mathbf{f}^{n+1} . \tag{2.48}$$

2.2.2 Structural damping (steady state case)

To simulate the structural displacement of the measurement set-up in section 3.2, damping is introduced via a Rayleigh damping model. This simplified damping model for the viscoelastic behaviour of the material

is justified, since steady state vibrations are considered and no transient behaviour. It is implemented by introducing an additional damping matrix \mathbf{C} into equation (2.47). The damping matrix consists of mass matrix \mathbf{M} and the stiffness matrix \mathbf{K} with the weights $\beta_{\mathbf{M}}$ and $\beta_{\mathbf{K}}$, giving

$$\mathbf{C} := \beta_{\mathbf{M}}\mathbf{M} + \beta_{\mathbf{K}}\mathbf{K}. \quad (2.49)$$

Inserting the damping matrix as defined in (2.49) into (2.47) results in the following differential equation to be solved

$$\mathbf{M}\ddot{\mathbf{u}} + \mathbf{C}\dot{\mathbf{u}} + \mathbf{K}\mathbf{u} = \mathbf{f}. \quad (2.50)$$

Instead of solving (2.50) in the time domain, a harmonic analysis for each measured frequency is performed to match the experimental set-up. In this way, the following complex algebraic system of equations is solved

$$(\mathbf{K} + j\omega\mathbf{C} - \omega^2\mathbf{M}) \hat{\mathbf{u}} = \hat{\mathbf{f}}. \quad (2.51)$$

As shown in [8], a mode superposition analysis including damping according to (2.49) leads to the following relation

$$\beta_{\mathbf{M}} + \beta_{\mathbf{K}}\omega_i^2 = 2\omega_i\xi_i, \quad (2.52)$$

with ω_i the i -th eigenfrequency (in rad/s) and ξ_i the modal damping for the i -th eigenfrequency. The modal damping factor ξ_i corresponds to the loss factor $\tan \delta_i$ for ω_i , so that

$$\tan \delta_i = 2\xi_i = \frac{\beta_{\mathbf{M}} + \beta_{\mathbf{K}}\omega_i^2}{\omega_i} \quad (2.53)$$

is obtained. With the help of a small deviation within (2.53), the two coefficients $\beta_{\mathbf{M}}$ and $\beta_{\mathbf{K}}$ can be computed by

$$\begin{aligned} \beta_{\mathbf{M}} + \beta_{\mathbf{K}}(\omega_i + \Delta\omega)^2 &= 2(\omega_i + \Delta\omega)\xi_i, \\ \beta_{\mathbf{M}} + \beta_{\mathbf{K}}(\omega_i - \Delta\omega)^2 &= 2(\omega_i - \Delta\omega)\xi_i. \end{aligned}$$

2.3 Fluid-Solid interaction

For a correct representation of the fluid-structure interaction, two conditions must be met at the common interface Γ_{fs} between fluid and solid. First, the fluid velocity and structural velocity must be equal

$$\mathbf{v} = \frac{\partial}{\partial t} \mathbf{u} \quad \text{on } \Gamma_{fs}, \quad (2.54)$$

which indicates that the fluid adheres to the structure. For a fixed wall, this corresponds to a “no-slip” condition.

The second condition is the continuity of stress in the normal direction along the interface, indicating that the fluid stress $\boldsymbol{\sigma}_f$ and the solid stress $\boldsymbol{\sigma}_s$ must coincide, which is enforced by

$$[\boldsymbol{\sigma}_s] \cdot \mathbf{n} = [\boldsymbol{\sigma}_f] \cdot \mathbf{n} \quad \text{on } \Gamma_{fs}. \quad (2.55)$$

Here, \mathbf{n} denotes the outer pointing normal of the fluid field. Therefore, the acting fluid forces can be split up into a pressure and a viscous component

$$\mathbf{f}_{fs} = \underbrace{\rho_f \int_{\Gamma_{fs}} -p \mathbf{1} \cdot \mathbf{n} \, dx}_{\text{pressure force}} + \underbrace{\int_{\Gamma_{fs}} \mu \left(\nabla \otimes \mathbf{v} + (\nabla \otimes \mathbf{v})^T \right) \cdot \mathbf{n} \, dx}_{\text{viscous force}}. \quad (2.56)$$

Hence, on Γ_{fs} the following Neumann boundary condition for structural mechanics is applied

$$[\boldsymbol{\sigma}_s] \cdot \mathbf{n} = [\boldsymbol{\sigma}_f] \cdot \mathbf{n} = -\rho_f P \mathbf{1} \cdot \mathbf{n} + \mu \left(\nabla \otimes \mathbf{v} + (\nabla \otimes \mathbf{v})^T \right) \cdot \mathbf{n}. \quad (2.57)$$

A detailed description of linear elasticity and implementation of the FEM can be found by Kaltenbacher [54].

2.3.1 Aitken relaxation

For an increase in convergence of the staggered coupling of fluid and structure, the simple yet effective Aitken relaxation is used, as described by Irons and Tuck [49]. Küttler and Wall [57] presented a very clear description of the Aitken method together with the application of fluid flowing through a flexible tube. For the relaxation it is sufficient to regard just the interface displacement \mathbf{d} instead of the whole structure. Thereby, the relaxation is given by

$$\mathbf{d}_{k+1} = \gamma_{k+1} \widehat{\mathbf{d}}_{k+1} + (1 - \gamma) \mathbf{d}_k, \quad (2.58)$$

with the relaxation parameter γ_{k+1} , the iteration counter k and $\widehat{\mathbf{d}}_{k+1}$ denoting non relaxed interface displacement. By introducing the displacement change

$$\Delta \mathbf{d}_{k+1} = \mathbf{d}_k - \widehat{\mathbf{d}}_{k+1},$$

the Aitken μ_{k+1}^A factor is computed

$$\mu_{k+1}^A = \mu_k^A + (\mu_k^A - 1) \frac{(\Delta \mathbf{d}_k - \Delta \mathbf{d}_{k+1}) \cdot \Delta \mathbf{d}_{k+1}}{(\Delta \mathbf{d}_k - \Delta \mathbf{d}_{k+1})^2},$$

which leads to the relaxation parameter

$$\gamma_{k+1} = 1 - \mu_{k+1}^A.$$

2.3.2 Mesh smoothing

During fluid-structure interaction, the structural movement changes the domain of the flow. Physical effects are covered in the previous section 2.3, but the implication of the mesh still need to be discussed. Here, the mesh itself is regarded as a pseudo structure, having the unknown displacement variable \mathbf{r} . Based on the equation of linear elasticity (2.46), the deformation can be determined by

$$\mathbf{K} \mathbf{r} = \mathbf{f}_g, \quad (2.59)$$

but in contrast to the structure and fluid field, there is no necessity for time dependency. The right hand side of (2.59) consists only of a Dirichlet boundary condition, which is specified by the position of the adjacent structure.

The material parameters are concealed in the stiffness matrix \mathbf{K} . They can be set arbitrarily, as it is an artificial structure. For small deformations a constant parameter value is sufficient, but for large deformations the choice of parameters can lead to mesh qualities which cause inaccurate results in the flow field. In the worse case overlapping elements may occur, rendering the mesh useless. For this reason a two step method is employed. Firstly, the deformation \mathbf{r} of the mesh is calculated with a constant pseudo elasticity modulus E_0 . Pseudo strain $[\epsilon_g]$ is then determined

$$[\epsilon_g] = \frac{1}{2} (\nabla \otimes \mathbf{r} + (\nabla \otimes \mathbf{r})^T), \quad (2.60)$$

to obtain a measure of deformation, considered for each element. In a second step the deformation calculation is repeated, but each element receives a new elasticity modulus

$$E_e = \sqrt{\frac{1}{3} ([\epsilon_g]_{e,11}^2 + [\epsilon_g]_{e,22}^2 + [\epsilon_g]_{e,12}^2)}, \quad (2.61)$$

with the index “ e ” denoting the element number. This ensures that elements which were exposed to large deformation in the first step will undergo a smaller deformation in the second step and vice versa, ensuring a smooth mesh. Instead of using E_0 as an initial value in the first step, it is advantageous to use the parameters that were identified in the previous time step.

For Poisson’s ratio, a value of 0.0 has been chosen, which has shown to be advantageous according to Johnson and Tezduyar [52]. The presented grid smoother was introduced by Löhner and Yang [63], but they use a distance function to construct the artificial parameters.

2.4 Aeroacoustics

Aeroacoustics is the study of flow induced sound generation and propagation. Sound generation is associated with turbulent flow, periodic varying flow or aerodynamic forces acting on solids. Simulating aeroacoustics can be performed either by direct numerical simulation (DNS) or a so called *hybrid method*. In the case of DNS, the compressible NSE are used. This not only captures flow effects, but also acoustic quantities – particle velocity and acoustic pressure. The high disparity in scale between acoustic pressure and hydrodynamic pressure, reach differences to the order of 10^3 – 10^5 , results in this approach posing some difficulties. Furthermore, the different numerical requirements for fluid dynamics and acoustics have to be considered, e.g., the mesh size needs to be fine enough to resolve small scale vortices, but due to the relative long acoustic wave length, a significantly coarser mesh for the acoustic computation could be used. Geometrical requirements also differ. The region of interest for flow is relatively confined, whereas radiated sound is relevant even at a distance. For instance during speech, the acoustic generating flow field is mainly restricted to the larynx (length ~ 10 cm) and the perceived sound of the speaker is monitored at 3 m distance of the mouth. Another crucial point are the boundary conditions, as they should guarantee a correct velocity outflow but also correctly represent acoustic waves leaving the simulation domain, i.e. no acoustic reflection at outflow. As this is not yet efficiently solved, a computational alternative for low Mach number flows is the hybrid method. Based on results of (*here*: incompressible) NSE, the acoustics are calculated separately. In this way the previously mentioned difficulties and problems can be circumvented, as there are no restraints by the flow simulation on the acoustic simulation of geometry, mesh size and even time step size (to a certain degree). Two hybrid methods, Lighthill’s acoustic analogy derived by Lighthill [59, 60] and the perturbation equations derived by Hüppe [47] are presented in the upcoming sections – section 2.4.1 and section 2.4.3 respectively.

2.4.1 Lighthill's analogy

Lighthill's idea was to separate the flow dynamical dimension from the acoustical in the NSE. This results in the quantities p' (fluctuating pressure) and ρ' (fluctuating density) being introduced with the following relation

$$p' = p - p_0; \quad \rho' = \rho - \rho_0; \quad \frac{p'}{\rho'} = c^2, \quad (2.62)$$

where c is the speed of sound² and the index "0" denotes the temporal and spacial mean. The relations given in (2.62) are only valid for an adiabatic process, i.e., where no heat transfer is taking place, which is valid for the assumption of constant temperature. As discussed in section 2.1, the compressible mass conservation equation (2.8) and momentum equation in the notation of (2.17) are given by

$$\frac{\partial}{\partial t} \rho + \nabla \cdot (\rho \mathbf{v}) = 0, \quad (2.63)$$

$$\rho \frac{\partial}{\partial t} (\mathbf{v}) + \rho (\mathbf{v} \cdot \nabla) \mathbf{v} = -\nabla p + \nabla \cdot [\boldsymbol{\tau}]. \quad (2.64)$$

Thereby, any volume forces \mathbf{f}_Ω are set to zero.

Since the derivative of the mean pressure p_0 is zero, it can be added to the right hand side of (2.64). Furthermore, multiplying (2.63) by \mathbf{v} and also adding it to (2.64) results in

$$\underbrace{\mathbf{v} \frac{\partial}{\partial t} \rho + \rho \frac{\partial}{\partial t} (\mathbf{v})}_{\frac{\partial}{\partial t} (\rho \mathbf{v})} + \underbrace{\mathbf{v} \nabla \cdot (\rho \mathbf{v}) + \rho (\mathbf{v} \cdot \nabla) \mathbf{v}}_{\nabla \cdot (\rho \mathbf{v} \otimes \mathbf{v})} = -\nabla (p - p_0) + \nabla \cdot [\boldsymbol{\tau}]. \quad (2.65)$$

With the definition of the Lighthill tensor

$$T_{ij} = \rho v_i v_j + (p - c^2 \rho) \delta_{ij} - \tau_{ij}. \quad (2.66)$$

²The speed at which acoustic waves propagate depends on the medium it travels in, for air at sea level at about 20° it is approximately 340m/s.

Equation (2.65) can be rewritten by adding the term $c^2 \nabla \rho$ on both sides as

$$\frac{\partial}{\partial t}(\rho \mathbf{v}) + c^2 \nabla \rho = -\nabla \cdot [\mathbf{T}]. \quad (2.67)$$

The differential operator ∇ is applied to (2.67) and the equality

$$\nabla \rho = \nabla(\rho_0 + \rho') = \nabla \rho'$$

is exploited – due to the fact that $\nabla \rho_0 = 0$. By additionally applying the time derivative to the mass conservation equation (2.65), $\frac{\partial}{\partial t} \nabla \cdot (\rho \mathbf{v})$ can be substituted and (2.67) is transformed into the inhomogeneous wave equation

$$\frac{\partial^2}{\partial t^2} \rho' - c^2 \Delta \rho' = \Delta[\mathbf{T}]. \quad (2.68)$$

To understand the source term in (2.68), it is necessary to take a closer look at the Lighthill tensor (2.66). This reveals that three of the four terms are part of the momentum flux tensor, the isotropic contribution p , the non-isotropic term $[\boldsymbol{\tau}]$ (viscous stress) and the convection of the i -momentum in the j -direction through term $\rho v_i v_j$. According to Lighthill [59], these exactly represent the aerodynamically generated sound sources: “By forcing the rates of momentum flux across fixed surfaces to vary, (...)”.

When a constant temperature is assumed ($p - c^2 \rho = 0$, see also (2.62)) and viscous stress effect are neglected as the dynamic viscosity of air is relative low, Lighthill’s tensor can be approximated by

$$T_{ij} \approx \rho_0 v_i v_j. \quad (2.69)$$

Remark: Outside the flow region the fluctuating quantities p' and ρ' are identical to the acoustic quantities p^a and ρ^a , respectively.

Remark: The assumption of a constant temperature inside the medium also implies low Mach number flows ($Ma \leq 0.3$). Otherwise heating may occur due to fluid friction or cooling due to rapid acceleration.

2.4.2 Finite element formulation – wave equation

In order to employ the FEM; the boundary value problem (2.68) is required in a weak formulation. To achieve this, equation (2.68) is multiplied by an appropriate test function and is integrated over the whole domain Ω_a . The necessary test function ψ is chosen from the Sobolev space H_0^1 . With $p' = c^2 \rho'$ the variational formulation is then given as

$$\int_{\Omega_a} \frac{1}{c^2} \frac{\partial^2 p'}{\partial t^2} \psi \, dx - \int_{\Omega_a} \Delta p' \psi \, dx = \int_{\Omega_a} \nabla \cdot (\nabla \cdot \mathbf{T}) \psi \, dx .$$

Applying Green's integral theorem on the second derivatives in space results in

$$\begin{aligned} \int_{\Omega_a} \frac{1}{c^2} \frac{\partial^2}{\partial t^2} p' \psi \, dx + \int_{\Omega_a} \nabla p' \cdot \nabla \psi \, dx \\ = - \int_{\Omega_a} \nabla \cdot \mathbf{T} \cdot \nabla \psi \, dx . - \int_{\Gamma_a} \nabla \cdot \mathbf{T} \cdot \psi \mathbf{n} \, dx, \end{aligned} \quad (2.70)$$

with the outer pointing normal \mathbf{n} . An advantage of the FEM with regard to Lighthill's analogy is the order reduction of the spatial derivative of the Lighthill tensor due to the integration by parts. Hard reflecting walls are assumed at the vocal tract and larynx and therefore the boundary integral on the left hand side of equation (2.70), arising from the integration by parts, is zero.

The infinite-dimensional space is replaced by the finite-dimensional subspace $V_h \subset H^1$ and a basis $\{\varphi_1, \dots, \varphi_N\}$ of V_h is selected, with N the number of FE nodes in the computational domain. Thereby, the unknown pressure is approximated by

$$p'(t, x) \approx p'_h(t, x) = \sum_{i=1}^N p'_i(t) \varphi_i(x) . \quad (2.71)$$

Verification for the presented method was published by Kaltenbacher

et al. [55], who compare simulation and experimental results of the acoustic field induced by flow around a cylinder. Additionally, they examine the acoustics of co-rotating vortex pairs for which an analytic solutions exists. Both verification examples were in good agreement with the corresponding experimental results or analytical solution.

To avoid backscattering of acoustic waves from the boundary of the computational domain, i.e. the inflow and the surroundings of the propagation region, a perfectly matched layer (PML) technique is applied according to Kaltenbacher et al. [53]. For further details and numerical implementation, Kaltenbacher [54] presents a detailed overview.

2.4.3 Perturbation equations (incompressible flow)

This CAA section introduces the acoustic perturbation approach as presented by Hüppe [47], which is related to the acoustic perturbation equation (APE) introduced by Ewert and Schröder [32].

The basis is the splitting technique that assumes the decomposition of flow field variables into a sum of components, in this case into a static part and two fluctuating parts, one hydrodynamical and one acoustical. In a compressible formulation, velocity, pressure and density are decomposed into

$$\begin{aligned}\mathbf{v}^c &= \bar{\mathbf{v}} + \mathbf{v}^h + \mathbf{v}^a, \\ p^c &= \bar{p} + p^h + p^a, \\ \rho^c &= \bar{\rho} + \rho^h + \rho^a.\end{aligned}\tag{2.72}$$

In equation (2.72) $(\bar{\cdot})$ denotes the temporal mean, the superscript “c” explicitly points out compressibility, “h” and “a” describe hydrodynamic and acoustic fluctuating parts, respectively – precise mathematical definition and calculus, helpful for the upcoming derivation, are found in Appendix B. The compressible mass conservation equation (2.63) is one of two equations which forms the basis to acquire the perturbation equa-

tions. Firstly, the time averaged version is considered

$$\overline{\frac{\partial}{\partial t} \rho} + \overline{\nabla \cdot \rho \mathbf{v}} = \overline{(\mathbf{v}^h \cdot \nabla (\rho^h + \rho^a))} + \overline{\nabla \cdot (\rho^h \mathbf{v}^a)} + \nabla \cdot (\bar{\rho} \bar{\mathbf{v}}) = 0. \quad (2.73)$$

In a second step, the splitting (2.72) is introduced into the compressible mass conservation equation, which results for (2.63) in

$$\begin{aligned} \frac{\partial}{\partial t} \rho^a + \nabla \cdot (\bar{\rho} \mathbf{v}^a + \rho^a \bar{\mathbf{v}} + \rho^h \mathbf{v}^a + \rho^a \mathbf{v}^h + \rho^a \mathbf{v}^a) \\ = -\frac{\partial}{\partial t} \rho^h - \nabla \cdot (\rho^h \bar{\mathbf{v}} + \bar{\rho} \mathbf{v}^h + \rho^h \mathbf{v}^h) - \frac{\partial}{\partial t} \bar{\rho} - \nabla \cdot (\bar{\rho} \bar{\mathbf{v}}). \end{aligned} \quad (2.74)$$

By neglecting non linear terms and applying $\nabla \cdot (\bar{\rho} \bar{\mathbf{v}}) = 0$, according to (2.73), equation (2.74) becomes

$$\begin{aligned} \frac{\partial}{\partial t} \rho^a + \nabla \cdot (\bar{\rho} \mathbf{v}^a) + \nabla \cdot (\rho^a \bar{\mathbf{v}}) = -\frac{\partial}{\partial t} \rho^h - \bar{\mathbf{v}} \cdot (\nabla \rho^h) \\ - \mathbf{v}^h \cdot \nabla \bar{\rho} - (\mathbf{v}^h \cdot \nabla \rho^h)' + \overline{\nabla \cdot (\rho^h \mathbf{v}^a)}. \end{aligned} \quad (2.75)$$

To obtain a complete system of equations, the physical quantities of pressure and velocity, but not the density, are split according to (2.72) in the compressible momentum equation (2.64), leading to

$$\begin{aligned} \frac{\partial}{\partial t} \mathbf{v}^a + \frac{\partial}{\partial t} (\bar{\mathbf{v}} + \mathbf{v}^h) \\ + ((\bar{\mathbf{v}} + \mathbf{v}^h) \cdot \nabla) (\bar{\mathbf{v}} + \mathbf{v}^h) + (\mathbf{v}^a \cdot \nabla) (\bar{\mathbf{v}} + \mathbf{v}^h + \mathbf{v}^a) \\ + ((\bar{\mathbf{v}} + \mathbf{v}^h) \cdot \nabla) (\mathbf{v}^a) \\ + \frac{1}{\rho^c} \nabla (\bar{p} + p^h + p^a) = -\frac{1}{\rho^c} \nabla \cdot [\tau]. \end{aligned} \quad (2.76)$$

For an incompressible flow, the incompressible quantities velocity and pressure are defined as $\mathbf{v}^{ic} = \bar{\mathbf{v}} + \mathbf{v}^h$ and $p^{ic} = \bar{p} + p^h$, respectively. Subtracting the incompressible momentum equation from equation (2.76)

then results in

$$\begin{aligned} \frac{\partial}{\partial t} \mathbf{v}^a + (\mathbf{v}^a \cdot \nabla) (\bar{\mathbf{v}} + \mathbf{v}^h) \\ + ((\bar{\mathbf{v}} + \mathbf{v}^h) \cdot \nabla) \mathbf{v}^a + \frac{1}{\rho^c} \nabla p - \frac{1}{\rho_f} \nabla p^{ic} = 0. \end{aligned} \quad (2.77)$$

For an adiabatic process the approximation

$$\frac{1}{\rho^c} \nabla p - \frac{1}{\rho_f} (\bar{p} + p^h) \approx \frac{1}{\rho_f} p^a \quad (2.78)$$

holds, as well as $p' - c^2 \rho' = \text{const.}$. By additionally removing non linear terms and couplings of fluctuating quantities, i.e., $(\mathbf{v}^a \cdot \nabla) \mathbf{v}^h$, equations (2.75) and (2.77) then form the perturbation equations

$$\begin{aligned} \frac{\partial}{\partial t} p^a + \rho_f c^2 \nabla \cdot (\mathbf{v}^a) + \nabla \cdot (p^a \bar{\mathbf{v}}) = - \frac{\partial}{\partial t} p^{ic} - \bar{\mathbf{v}} \cdot (\nabla p^{ic}), \\ \rho_f \frac{\partial}{\partial t} \mathbf{v}^a + \rho_f (\mathbf{v}^a \cdot \nabla) \bar{\mathbf{v}} + \rho_f (\bar{\mathbf{v}} \cdot \nabla) \mathbf{v}^a + \nabla p^a = 0. \end{aligned} \quad (2.79)$$

Hüppe [47] presents a more detailed derivation and discussion of the perturbation equation. Additionally, the reader is referred to this work for the incorporation into the FEM, which also requires a special method to achieve stability – the mixed FEM together with stabilisation terms.

2.4.4 Alternative source terms for the wave equation

Having derived the wave equation with Lighthill's source term approach and the perturbation equation, it is now possible to vary the right hand side of the wave equation, in essence varying the derivation of the acoustic source terms. In Lighthill's approach the hydrodynamic quantities for determining the acoustic source term are the fluid velocities. In the two upcoming variations these are calculated based on the hydrodynamic pressure. An advantage of this approach is that pressure is a scalar quantity. This means that when it comes to numerical simulation, three times less storage will be required than that of the vector valued fluid

velocity.

Source term $\frac{\partial^2}{\partial t^2} p^{\text{ic}}$

Starting with the perturbation equations (2.75) and neglecting the influence of the mean flow $\bar{\mathbf{v}}$, which may be done for low flow velocities, the equations simplify to

$$\frac{\partial}{\partial t} p^{\text{a}} + \rho_{\text{f}} c^2 \nabla \cdot \mathbf{v}^{\text{a}} = -\frac{\partial}{\partial t} p^{\text{ic}}, \quad (2.80)$$

$$\rho \frac{\partial}{\partial t} \mathbf{v}^{\text{a}} + \nabla p^{\text{a}} = 0. \quad (2.81)$$

To merge the two equations, the same technique as for the wave equation with Lighthill's tensor (2.68) is used – applying the time derivative to (2.80), $\nabla \cdot$ to (2.81) and substituting $\frac{\partial}{\partial t} \nabla \cdot (\rho \mathbf{v})$. This leads to the inhomogeneous wave equation with the second derivative in time of the incompressible pressure p^{ic} as the source term

$$\frac{\partial^2}{\partial t^2} p^{\text{a}} - c^2 \Delta p^{\text{a}} = -\frac{\partial^2}{\partial t^2} p^{\text{ic}}. \quad (2.82)$$

Source term Δp

Another possibility is to begin with the altered version of the momentum equation (2.65) and neglect the viscous stress, as done for the approximation of the Lighthill tensor (2.69). For the approximated Lighthill tensor (2.69) this leads to

$$\nabla (\mathbf{v}^{\text{ic}} \otimes \mathbf{v}^{\text{ic}}) = \frac{\partial}{\partial t} (\rho_{\text{f}} \mathbf{v}^{\text{ic}}) + \nabla p^{\text{ic}}. \quad (2.83)$$

Assuming ρ_{f} is to be constant and replacing the Lighthill tensor in the wave equation (2.68) by (2.83) transforms the source term to a second

derivative in space of the pressure

$$\frac{1}{c^2} \frac{\partial^2}{\partial t^2} p' - \Delta p' = -\Delta p^{\text{ic}} + \underbrace{\nabla \cdot \left(\rho_f \frac{\partial}{\partial t} \mathbf{v}^{\text{ic}} \right)}_{=0}. \quad (2.84)$$

Vocal fold models and material parameters

Simplification of the complex larynx is necessary for numerical simulations and therefore it is modelled as a simple rectangular channel with two indentations forming the vocal folds. In section 3.1 2D, geometry is presented which is used for FSI simulations in this work, but which will also be compared to a second model found in numerous publications.

There are large discrepancies in measurement data relating to the material parameters of vocal folds, as explained by Alipour et al. [3]. This is due to the fact that the thin and complex structure makes an experimental measurement difficult.¹ Consequently, a new method suited for determining soft tissue material parameters is presented in section 3.2, but is yet to be further developed for in vivo application.

¹Difficulties in parameter measuring also arise due to the form and inaccessibility inside the human larynx. For dissected vocal folds the question of pre-stress arise which is also unknown.

3.1 2D geometrical model

The geometric 2D model used in this work consists of a simple channel with two elastic bodies inside representing the vocal folds. Through use

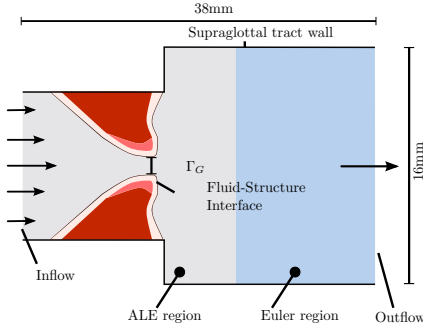


Figure 3.1: 2D model with fluid regions and vocal folds.

of magnetic resonance imaging (MRI), Gömmel [36] extracted the geometry of the trachea, which shows that the vibration of the vocal fold covers only a part of the trachea. This fact is incorporated by narrowing the subglottal channel width as depicted in Fig. 3.1.

There are two prominent models of the vocal folds: 1) the “M5” model constructed by Scherer et al. [76, 77], and 2) the model by Šidlof et al. [94], which uses an ex vivo plaster-casting methodology. A 2D version of the latter model is used in the subsequent simulations due to its complexity and realistic structure and will from now on be referred to as “S-Model”. For the sake of completeness, a comparison of the models is presented in section 4.2. Both have been improved by additionally considering different layers. The muscle, also called the body, is at the base, and has a skewed trapezoidal form and supports the ligament. Both the muscle and the ligament are covered by the lamina propria, which is approximately 1.2 mm thick at the base and narrows to half of its original thickness at the tip of the vocal fold. The lamina propria is covered by

a very thin tissue (0.05 mm) called the epithelium, represented by a thin line in Fig. 3.2.

As mentioned, material parameters are still uncertain, and therefore

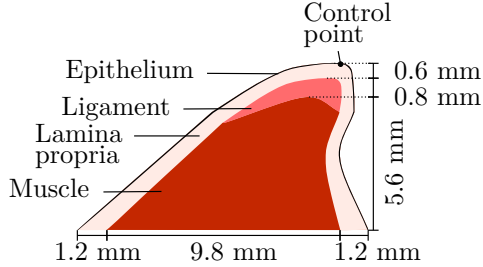


Figure 3.2: Geometry and material model of the vocal fold, consisting of four different regions. Dotted lines are reference lines for better readability.

the material parameters used here rely on good estimation and comparison with different models. Additionally, an eigenfrequency analysis is performed in advance to achieve a realistic vibrational frequency that mimics human phonation (Titze [89]). The elasticity moduli, used in the simulations are listed in Tab. 3.1.. A Poisson's ratio of 0.45 is taken for all four tissue types. It should be noted that according to Cook et al. [18] human phonation is not sensitive towards Poisson's ratio.

Table 3.1: Vocal fold material parameters for the 4 layer model.

Material	Elasticity modulus (kPa)
muscle	30
ligament	25
lamina propria	20
epithelium	50

3.1.1 M5 vocal fold shape

The model of Scherer et al. [76, 77] was developed for a scaled up measurement set-up to determine the pressure profiles along its surface. The model is well established and used by different research groups, also for numerical simulation (e.g. Šidlof et al. [95]). Therefore, it is considered in this work and will be compared to the model by Šidlof et al. [94], the model on which the 2D simulations presented here are focused. Topologically speaking, the multi layer M5 model is identical to the model

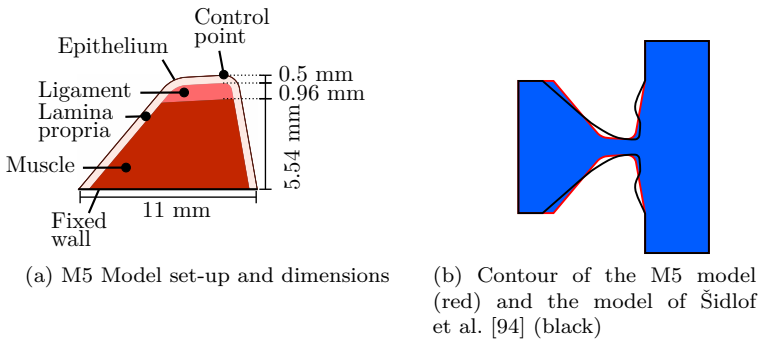


Figure 3.3: M5 vocal fold shape, geometry, regions and boundaries.

presented earlier in section 3.1.

3.2 Determining material parameters with the pipette aspiration method

The pipette aspiration method is designed to measure material parameters of soft tissues as a function of frequency, in particular the elasticity modulus of silicone or polyurethane mixtures, which substitute human vocal folds. It is of interest how the material parameters, especially the elasticity modulus, change over the frequency range of human phonation. Conditions for the measurement system are: it should resolve small ar-

3.2 Determining material parameters with the pipette aspiration method

feasible to identify spatial differences which would make it possible to compare healthy tissue with scarred tissue, and the measurement should not damage or strain the material, since that would influence any further measurement on the same material.

The pipette aspiration was originally introduced by Rand and Burton [73] to measure the stiffness and intracellular pressure of red blood cell membranes. Therein, a pipette was placed onto the material sample and excited via a static low pressure, sucking the material into the pipette. The displacement was plotted against the applied pressure resulting in a linear relation. The slope of this relation determines the stiffness. Further works on this method can be found in Evans [30]. An application to determine the elasticity modulus on soft tissues was presented by Aoki et al. [6], Matsumoto et al. [65], Ohashi et al. [70]. Here, the method has been extended to determine the elasticity modulus over the frequency range of 20–250 Hz by replacing the static pressure with a fluctuating pressure. The exciting pressure is measured by a microphone, close to the sample, and mechanical vibrations by a laser scanning vibrometer. With the help of FE simulations of the experimental set-up, the elasticity modulus of the sample is automatically adjusted within the computations until simulated and measured displacements are in good agreement. The FEM numerically solves the partial differential equation for linear elasticity. For a correct modelling of the vibrating silicone its elasticity modulus, Poisson ratio and damping behaviour is needed. To determine the modal damping, a measurement set-up has been developed, which will be utilised in the FE model via a Rayleigh damping approach.

In section 3.2 we discuss the details of the experimental set-up of the enhanced aspiration pipette which allows dynamic pressure excitation of the sample material at frequencies in the phonatory range. Section 3.2.3 describes the measurement set-up for determining the damping properties. Therewith, the loss factor of the sample material over the considered frequency range is obtained. The FE formulation as presented in section 2.2.1 is then used to determine, through optimisation, the elasticity moduli of the samples by using the measured pressure excitation and displacement as boundary conditions. Results of these investigations will be discussed in section 3.2.5, where the obtained elasticity moduli for

three different silicone materials are presented as a function of frequency.

3.2.1 Pipette aspiration set-up

In the original set-up (Aoki et al. [6]), a static low pressure was used to suck the material into the pipette and the resulting deformation was measured. The elasticity modulus was then determined using a simple analytical formula. This work replaces the static low pressure with a fluctuating pressure, induced by a pistonphone at a pre-set frequency as displayed in Fig. 3.4. A flexible tube channels the pressure to a gauge head with a pipette fixed to it, which is placed upon the sample. Different diameters of the pipette make it possible to define the enclosed area that the fluctuating pressure acts on. Therefore, it is possible to resolve a very small spatial area. The force generated by the fluctuating pressure makes the enclosed area vibrate. The displacement of the vibration is measured with the help of a laser scanning vibrometer. A draft of the whole set-up

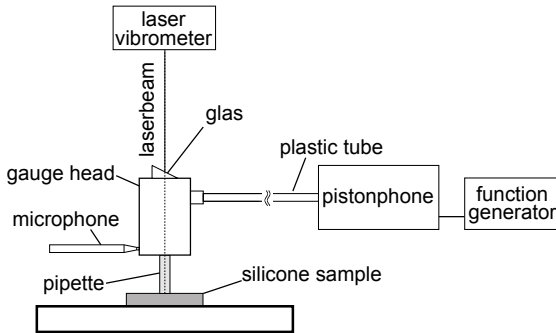


Figure 3.4: Schematic layout of the experimental set-up.

is depicted in Fig. 3.4. It should be noted that for it to function correctly, the set-up has to be air tight from pistonphone to pipette.

In the following, the main components of the experimental set-up will be discussed in detail.

3.2.2 Pressure inducer and measurement

A pistonphone with an inner diameter of 30 mm and a stroke of 50 mm was designed and manufactured. It consists of a piston inside a cylinder which is propelled by the shaker “TIRAvib S 504” from *Tira GmbH* as depicted in Fig. 3.5. The shaker works at a frequency range of 2–11 000 Hz fed with a sine signal. To regulate the pressure amplitude, the amplifier “BAA 120” controlled by a function generator is used. The movement of the piston generates a fluctuating pressure. A flexible plastic tube is fixed at the end of the pistonphone to channel the excited pressure. To detect the fluctuating pressure near the sample, a 1/8-inch micro-

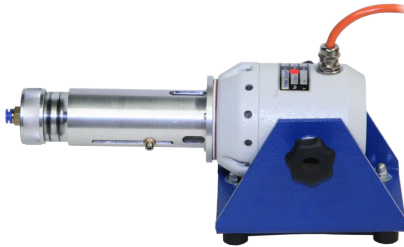


Figure 3.5: Pistonphone mounted onto shaker.

phone (Type *Brüel & Kjær* 4138) is positioned inside the gauge head. It has a frequency range of 6.5 Hz–140 kHz and a pressure range of about 0.01 Pa–7 kPa.

Displacement measurements

The displacement of the sample due to the fluctuating pressure is in the range of 10–100 μm , which demands a very accurate measurement method. Therefore, a laser scanning vibrometer, the PSV 300 from *Polytec*, is applied. A helium-neon laser exploits the Doppler effect to derive the velocity. The displacement is a sinusoidal movement and is obtained

by integrating over velocity, which is performed by the laser vibrometer's software.

Displacements up to a frequency of 1 kHz using 16 000 FFT-points are measured. Furthermore, the laser scanning vibrometer is capable of scanning a number of points on the surface, enabling the shape of the deformed area to be determined.

Due to the small displacement, external influence must be kept to a minimum or remedied. As a result, the measurement set-up, including the laser vibrometer, were placed on a vibration controlled table to damp outside vibrations and interferences.

The surface of the silicone sample reflects the laser poorly making laser measurement difficult, thus a titanium dioxide powder is applied onto the sample enabling it to reflect the laser light satisfactorily. A thin coating is sufficient and as the titanium dioxide is a fine powder, the elasticity modulus is not affected.

3.2.3 Damping measurement set-up

The damping behaviour of the considered silicone material is obtained using a free vibration decay test. To do this, a sandwich beam is constructed consisting of the silicone material and two steel plates, as displayed in Fig. 3.6. This sandwich beam is clamped and excited by an impulse ham-

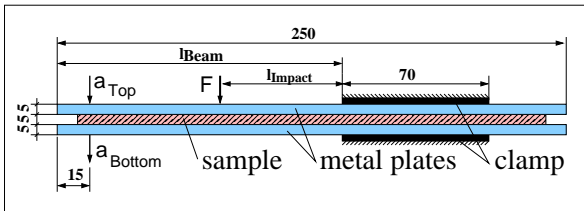


Figure 3.6: Sample between to plates (all dimensions in millimetre).

mer. Two miniature accelerometers on the top and the bottom steel plate measure the acceleration of the free vibration. Both accelerometers are

3.2 Determining material parameters with the pipette aspiration method

of the type 8614A500M1 (*kistler*), which resolve frequencies in a range of 10 Hz to 25 kHz and accelerations of up to ± 500 g at a sensitivity of 4 mV/g.

By changing the position of the clamping, different modes can be excited and thus decayed vibrations at different frequencies can be obtained. E.g., Fig. 3.7 displays the free vibration decay curves at a frequency of 32 Hz. By extracting from these curves the resulting peaks s_j , the loga-

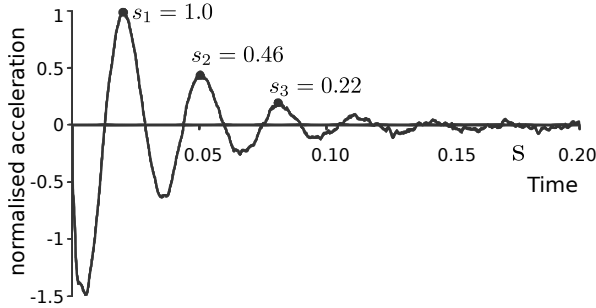


Figure 3.7: Measured normalised acceleration of the free vibration decay test (excited mode vibrates at 32 Hz).

rithmic decrement D_i is calculated with the following formula

$$D_i = \ln \frac{s_i}{s_{i+1}}. \quad (3.1)$$

Finally, the relation between the logarithmic decrement D_i , the modal damping factor ξ_i and the loss factor $\tan \delta_i$ is given by

$$\frac{1}{2} \tan \delta_i = \xi_i = \sqrt{\frac{D_i^2}{D_i^2 + 4\pi^2}}. \quad (3.2)$$

The experiments resulted in a constant loss factor $\tan \delta$ of 0.12 over the considered frequency range.

3.2.4 Numerical framework

Based on the solid mechanical equations highlighted in section 2.2 and the corresponding FEM (section 2.2.1), the simulation of pipette aspiration was performed. Four types of boundary conditions are necessary for the material sample, each at different surfaces, as shown in Fig. 3.8. For the boundary enclosed by the pipette Γ_P , a fluctuating force is set, given by the measured pressure from the experiment. This results in the formulation

$$[\sigma]^T \vec{n} = p_m \vec{n} \quad \text{on } \Gamma_P \times (0, T), \quad (3.3)$$

with p_m representing the measured pressure excitation. The region Γ_{D_z}

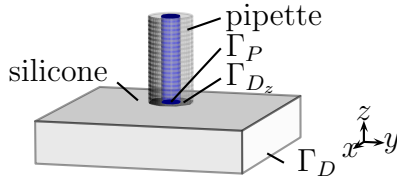


Figure 3.8: Different boundary conditions for the solid mechanics simulation of the pipette aspiration.

where the pipette is placed upon the sample can only move in the x - y -plane, restricting any movement in z -direction

$$u_z = 0 \quad \text{on } \Gamma_{D_z} \times (0, T).$$

From the bottom side Γ_D , the displacement is completely fixed leaving no degree of freedom

$$\vec{u} = 0 \quad \text{on } \Gamma_D \times (0, T).$$

3.2 Determining material parameters with the pipette aspiration method

All other boundaries Γ_N are not limited by outside forces, and therefore homogeneous boundary conditions are applied

$$[\sigma]^T \vec{n} = 0. \quad (3.4)$$

In order to meet the measured loss factor 0.12, the mass damping factors α_K and α_M are adjusted for each frequency in the harmonic analysis.

The Poisson ratio of the investigated silicones is in the range of 0.36 to 0.42 as shown by Drechsel [25] and can be assumed to be constant over the considered frequency range. This has been additionally ensured by performing all FE computations for determining the elasticity modulus with different Poisson ratios within the above mentioned range. Since the results only revealed a difference of 5% for the elasticity modulus, the presented data uses the mean value of the Poisson ratio.

3.2.5 Results

For experimental investigations, the fabricated samples were moulded into a cuboid with 50 mm in depth and width and 10 mm in height. All samples were made of a silicone which consists of a two-part silicone composite, Ecoflex™ Platinum Cure Silicone Rubber Part-A and Part-B, and a silicone thinner. The mixing ratio between silicone and silicone thinner determines the stiffness. Three samples with different mixing ratio were compared, 1:1:1, 1:1:2 and 1:1:3 (the first two numbers denote the ratio of the two-part silicone composite, while the third gives the ratio of the silicone thinner).

The measurements of all three samples have been performed by the pipette aspiration with the experimental set-up shown in Fig. 3.9. The applied pressure for the sample with a mixing ratio of 1:1:1 was kept at 158 Pa_{eff} over the whole frequency range. For the 1:1:2 sample it was 178 Pa_{eff} and 176 Pa_{eff} for the sample with the mixing ratio of 1:1:3. The pipette was lowered onto the sample taking special care that the pipette did not exert any force on the silicone, which would affect the results. This was achieved with the help of a travelling unit. A fluctuating pressure at a fixed frequency was applied with the help of the piston-

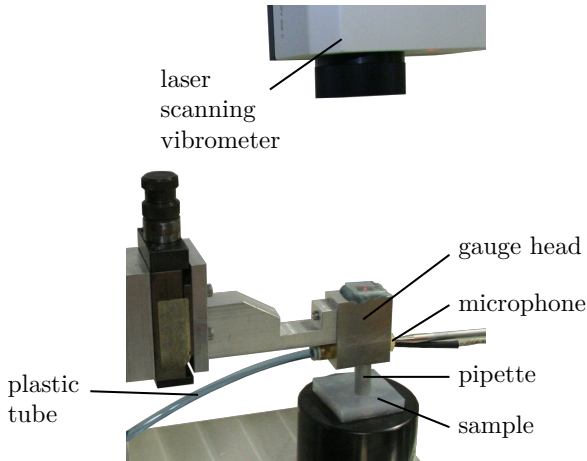


Figure 3.9: Laser vibrometer (top) measuring the displacement of the silicone sample through the gauge head (bottom).

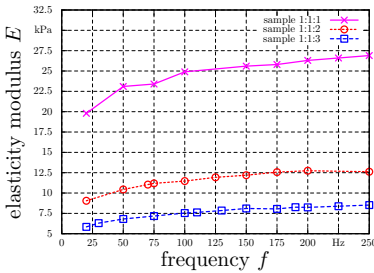
phone. Displacement and pressure was recorded. The piston was driven at different frequencies from 20–250 Hz to cover the frequency range of phonation.

To determine the elasticity modulus, the measurement was compared with the numerical simulation model as described in section 3.2.4. There-with, the numerical model was excited at the surface Γ_P (see Fig. 3.8) and the elasticity modulus was automatically adjusted by a gradient method in order to meet the measured displacements.

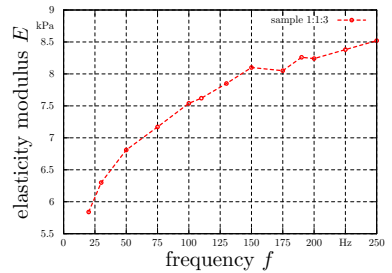
In Fig. 3.10a the elasticity moduli of all three samples are summarised with respect to the frequency at which they were excited. The results clearly show the increase of the elasticity modulus over the considered frequency range. For the stiffest material (mixing ratio of 1:1:1) an elasticity modulus of about 20 kPa was determined at an excitation frequency of 20 Hz. The elasticity modulus rises logarithmically to 27.5 kPa

3.2 Determining material parameters with the pipette aspiration method

at an excitation frequency of 250 Hz. The samples with a mixing ratio of 1:1:2 and 1:1:3 show a much lower elasticity modulus with a range of 9 kPa to 13 kPa and 5.8 kPa to 8 kPa, respectively. Nevertheless, the logarithmic increase of the elasticity modulus with increasing frequency can be seen for all samples. To further demonstrate this logarithmic behaviour of the elasticity modulus, Fig. 3.10b displays the results for the sample with mixing ratio of 1:1:3 separately,



(a) Elasticity modulus of a all three samples over different frequencies.



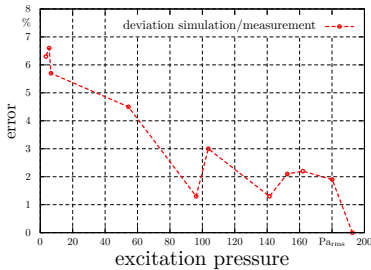
(b) A closeup of Fig. 3.10a for the 1:1:3 sample to identify the logarithmic behavior of the frequency dependant elasticity modulus.

Furthermore, the influence of the fluctuating pressure has been analysed by measuring the displacement of the 1:1:3 sample at different pressure amplitudes, keeping the frequency constant at 250 Hz. In a first step, measurements were performed at this fixed frequency and a pressure amplitude in the range of $6.6 \text{ Pa}_{\text{eff}} - 192 \text{ Pa}_{\text{eff}}$ was applied. For each measured point, the FE scheme was applied to determine the elasticity modulus. In a second step, simulations were performed for different pressure amplitudes, according to the measurements, but the elasticity modulus was kept constant for all computations, as extracted for the $192 \text{ Pa}_{\text{eff}}$ excitation case. Now, Fig. 3.10a shows the deviation between the simulated and measured peak displacement for all different pressure excitation cases. A dependency on the applied pressure that the sample is exposed to is visible. However, considering the pressure range, the

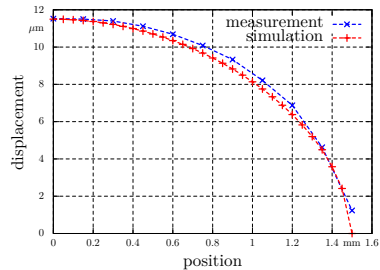
3 Vocal fold models and material parameters

deviation is relatively small. A 30 times decrease in excitation pressure results in a maximal deviation of only 7 % for the peak displacement.

In a final investigation, we studied the shape of the silicone material, which is periodically sucked into the pipette due to the harmonic excitation by the pressure. Since both the measured (using the scanning interferometer) and simulated (applying the FEM) shape exhibited axis symmetry of the curvature, the comparison is only shown for half of a cross-section through the centre. In Fig. 3.10b the measured and simulated shape is displayed, exhibiting a sufficient agreement.



(a) Derivation between simulated and measured peak displacement at different excitation pressures at a frequency of 250 Hz for a 1:1:3 sample.



(b) Displacement of measurement and simulation with rotation axis at y-axes. Excited with $43 \text{ Pa}_{\text{eff}}$ at 200 Hz.

Additionally, multiple measurements were made on the same are after removing and newly placing the pipette. Only marginal changes in the displacement resulted. This demonstrated that the pipette does not strain or damage the material.

CHAPTER 4

2D Simulation results

In the upcoming chapter, fully coupled FSI results of the human phonation will be presented. As 3D simulations are not yet feasible due to the computational cost caused by the iterative coupling of the flow field and structure, this chapter is restricted purely to 2D simulations.

Firstly, the numerical frame work will be discussed in section 4.1 and different vocal folds geometries will be investigated. Section 4.3 then analyses the impact and correctness of reducing the FSI problem in phonation to a pure flow problem with prescribed boundary conditions to reduce simulation time.

4.1 Numerical framework

As a measure, the volume flux, Q_V , of the glottis is used and calculated according to the following equation

$$Q_V(t) = \int_{\Gamma_G(t)} \mathbf{v} \cdot \mathbf{n} d\Gamma, \quad (4.1)$$

where Γ_G is the integration path inside the glottis (Fig. 3.1). Due to movement of the VFs, Γ_G varies in time.

4.1.1 Boundary conditions

As an inflow condition, a fixed pressure of 1 kPa is given and 0 Pa set at the outflow, which is consistent with realistic measurements made by Holmberg et al. [44]. The trachea wall Γ_T is set to a NSC

$$\mathbf{v} = \mathbf{0} \quad \text{on } \Gamma_T, t \quad (4.2)$$

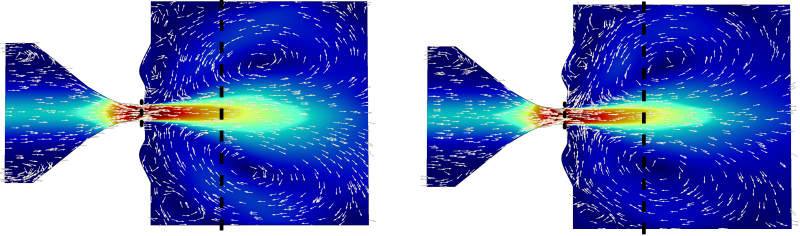
and VFs are fixed to the trachea, represented by a HBC

$$\mathbf{u} = \mathbf{0} \quad \text{on } \Gamma_T. \quad (4.3)$$

The interface boundary of fluid and structure is modelled as described in section 2.3.

The fluid is considered to be at rest as the initial condition in the analysis. The first 200 time steps of the analysis are disregarded, so that the flow field is fully developed and the VFs vibrate periodically.

To accurately resolve the flow structure, a grid study was performed (see section 4.1.2), which resulted in 42.000 finite elements with a quadratic basis function and, therefore, approximately 350.000 degrees of freedom for the flow velocity and pressure. To solve the PDE in time, the 2nd order backward differentiation formula (BDF2) with a time step size of $2.5 \cdot 10^{-5}$ s was used. Five thousand time steps were performed, which



(a) Time averaged velocity with 42K finite elements.

(b) Time averaged velocity with 105K finite elements.

Figure 4.1: Time averaged velocity field for different mesh sizes. Dashed line indicates the cross section displayed in the velocity profiles in Fig. 4.2.

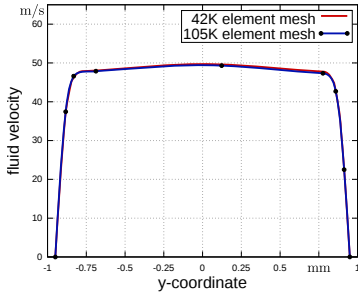
resulted in $t_{\text{end}} = 0.125$ s. As stopping criterion, for solving the nonlinear Navier-Stokes equations, an incremental L_2 -norm (both for velocity and pressure) with an accuracy of 10^{-5} is chosen. To address the strong coupling, iterations are necessary between the flow and structural mechanical field until the following incremental L_2 -norm for the mechanical displacement is met

$$\|u_{n+1}^{k+1} - u_{n+1}^k\|_2 < 10^{-6}, \quad (4.4)$$

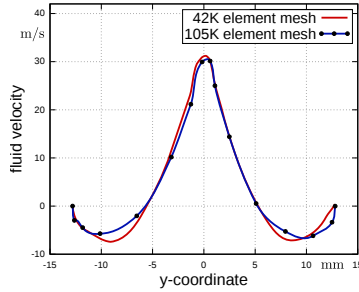
where n is the time step counter and k is the iteration counter.

4.1.2 Grid dependency

The influence of the computational mesh has been tested. A pure flow simulation and static geometry with a 42 K finite element grid was compared to a grid of 105 K elements. The time step size, number of steps, etc. were identical to values discussed in the previous section. The time averaged result of both mesh sizes are plotted in Fig. 4.1. Both simulations resulted in a similar pattern and position of the vortical structures.



(a) X component of velocity profile inside glottis of time averaged velocity field.



(b) X component of velocity profile downstream of glottis of time averaged velocity field.

Figure 4.2: Comparison of velocity profiles for mesh sizes at two cross sections (see Fig. 4.1).

To provide a more detailed analysis, the velocity profile of two significant cross sections are compared, considering the main component in the x direction (vertical component). The location of the cross sections are indicated in Fig. 4.1: one is inside the glottis and the second downstream of the glottis. The comparison of the velocity profiles, as plotted in Fig. 4.2, demonstrates a good agreement in the cross section inside the glottis (see Fig. 4.2a), whereas the profiles deviate slightly at the position downstream of the glottis. This is due to the lack of turbulence and boundary layer models: slight deviations are also expected with a finer mesh because it captures finer scales of turbulences. The analysis of downstream flow field is not the aim of this work and the results for different mesh sizes are in good agreement. Therefore, the 42 K finite element grid was used in the subsequent simulations.

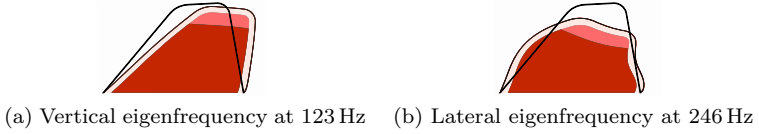


Figure 4.3: Eigenform and eigenfrequency of the 2D M5 model with 4 layers. The original form is outlined on top of each eigenform.

4.2 Comparison of vocal folds geometry

This section discusses the influence of VF geometry on the phonation process. Here, two VF geometries are closely examined; the M5 model and the S-Model, as presented in chapter 3. In Fig. 3.3b, the contours of the simulation geometry are shown. Only their VF geometry differs, all other parameters and boundary conditions are kept identical. Both have an identical channel geometry (length, width etc.) and initial glottis width. The inflow condition is set to 800 Pa, and the elasticity moduli of the epithelium, cover, ligament and muscle are set according to Tab. 3.1. An eigenfrequency analysis of the M5 model, given in Fig. 4.3, reveals that the second eigenfrequency is 30 Hz higher than for the S-Model (Fig. 4.8b). Further significant differences cannot be detected, as the vertical and lateral movement are similar, considering their different form. The transient simulation, however, reveals major differences. To quantify the dissimilarities, resulting values are compared and monitored at a control point positioned at the tip of the VF (see Fig. 3.3a and Fig. 3.2). Figure 4.4 divides up the displacement in each frequency component using a Fourier transformation. It shows that the vertical component at its first eigenfrequency (123 Hz) has a higher amplitude for the M5 model, whereas lateral movement (Fig. 4.4b) is more than twice as small as than for the S-Model. Generally speaking, the M5 model has a dominant movement in the flow direction, whilst the changes in glottis width turn out to be relatively small. In contrast, the absolute lateral displacement

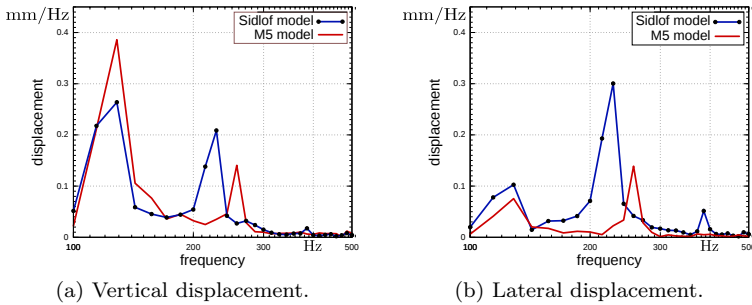


Figure 4.4: Vocal fold displacement in vertical and lateral direction at control point, divided into its frequency components by Fourier analysis.

of the S-Model is about 30% larger than its vertical displacement. Fig-

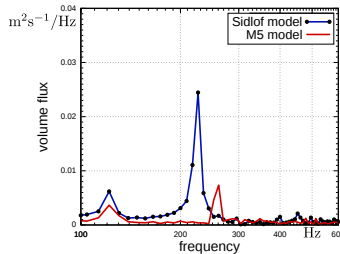


Figure 4.5: Volume flux in comparison of M5 model and S-Model, in frequency domain.

ure 4.5 illustrates the effect the vertical displacement has on the volume flux. The volume flux of the simulation with the M5 model has, at its main frequency, an amplitude 3 times lower in comparison to the flow simulation with the S-Model. And as the vertical displacement only has a marginally effect on the pulsation of the jet, a significantly dominant frequency in the flow of the M5 model is not present. In contrast, the

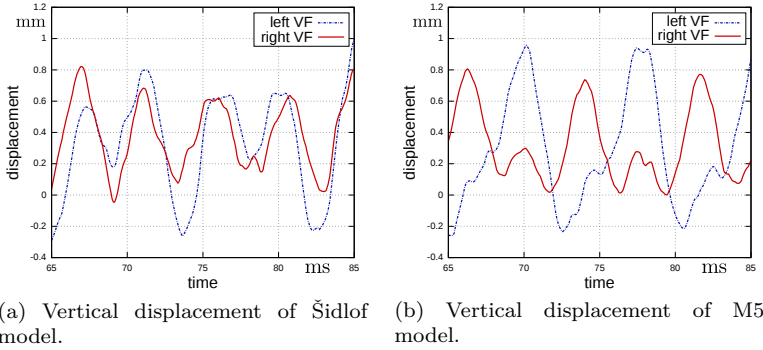
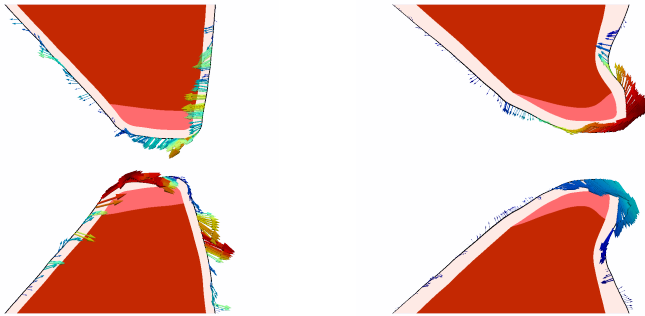


Figure 4.6: Vertical displacement of both VF models. Each graph shows the displacement of left and right VF.

flow simulated with the S-Model exhibits a notable peak at the frequency correlating to the lateral displacement frequency of its VFs.

The reason for the small lateral displacement of the M5 model is the bulky structure. The VFs need to be compressed to open. The S-Model has a bulge at its posterior side, called the sinus morgagni, so as the VFs are pushed downstream, they automatically open the glottis. As the fluid pressure equalises, the VFs move back and almost come into contact. Simulations show that the near contact is necessary for a synchronised oscillation. The M5 VFs do not come close enough and, therefore, when the flow field is fully developed, start to vibrate asynchronously at a phase shift of about 180° , as the time plot of the vertical displacement reveals (Fig. 4.6b). In contrast, for the vertical component of the S-model, as shown in Fig. 4.6a, both vocal folds move symmetrically. This symmetry behaviour for each model is shown Fig. ???. Vectors on the surface of the VFs indicate the displacement velocity and thereby the current direction. In Fig. 4.7a the opposite direction of the left and right VF is clearly visible, in contrast to the relatively symmetric movement of the S-Model (Fig. 4.7b).



(a) Asymmetric vibration of M5 model. (b) Symmetric vibration of S-Model

Figure 4.7: Deformation of both VF models at distinctive time steps. Vector arrows indicate the displacement velocity and thereby its current direction.

Gömmel [36] performed a similar study, with VF geometries comparable to the M5 and S-Model, but results differ from the current study. The model he used that was similar to *M5* shows a very good self oscillating vibration pattern, whereas his second model comparable to the S-Model and based on MRI (magnetic resonance imaging) data, has very small displacement amplitudes and, consequently, lower amplitudes in the flow. This difference to the current study, or even contradiction, can be explained by several points. Firstly, the VF models are not identical, only similar, and material parameters are, although in the same order, different. More relevant is, that Gömmel uses a 2- and 3-layer model (body, ligament and cover), thereby not including the epithelium. Simulations have shown that the epithelium bounds the very soft cover tissue, keeping the VFs as a unit and restricting an independent vibration of the cover. It must be pointed out that the epithelium only restricts and does not prevent the cover's oscillation. A further crucial cause for the discrepancies is the introduction of “artificial contact” and a smaller initial

glottis gap of 0.6 mm.

4.3 Investigation of prescribed movement

The aim of this study is to analyse the impact of reducing a fully-coupled fluid-structure phenomena to a purely fluid simulation with prescribed structural motion. To achieve this, structural displacements of a fully-coupled simulation are extracted and used as imposed motion for a straightforward flow simulation. Additionally, a number of variations to the pure fluid simulations, which include changes in fluid-structure interface conditions, pressure inlet and geometry, are examined. These variations imitate specific uncertainties or incorrect boundary conditions and are each elucidated in separate sections.

The geometric set-up, as discussed in section 3.1 with boundary values as given in section 4.1.1, is the reference set-up and will be referred to as the “original model”. Initially, a fully-coupled simulation is performed with the original model and the resulting VF movement is extracted; this is used as the prescribed movement for the pure fluid flow simulation. The first study (section 4.3.2) is a pure fluid simulation with prescribed movement and the velocity is set to $\mathbf{v} = 0$ at the interface boundary Γ_{fs} .

The second study (section 4.3.3) uses a lower inlet pressure of 800 Pa and sets the velocity field at the interface to the value recorded in the original set-up.

In section 4.3.4, slightly reformed VFs are used as shown in Fig. 4.13. To obtain a prescribed movement, the displacements from the fully-coupled simulations with the original VFs are projected onto the new shape. This case is then further altered by using a velocity inflow profile instead of a fixed pressure (section 4.3.5).

Different scenarios are assessed to analyse certain simulation approaches used to compute the human phonation process. Therefore, the focus lies on the impacts of using measurement data or estimates through observations (endoscopy) as prescribed VF movement and boundary condition of a pure flow simulation.

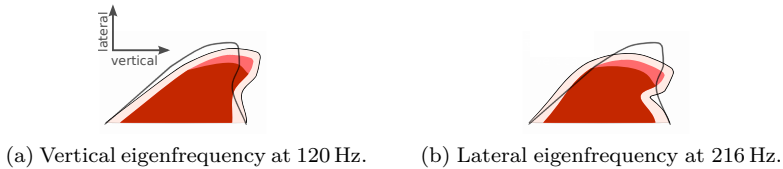


Figure 4.8: Eigenform and eigenfrequency of the 2D VF model with 4 layers. The original form is outlined on top of each eigenform.

4.3.1 Vocal fold vibration

An eigenfrequency analysis of the VFs is performed to determine the main frequencies of their natural vibration. The first two eigenfrequencies and their shapes are shown in Fig. 4.8. The lateral movement (Fig. 4.8b) is of importance, because it regulates the glottis width and, thereby, the fluid flow through the glottis. The reformed VFs have the first two eigenfrequencies at 122 Hz and 215 Hz. The eigenfrequencies of the two VFs are similar because their shapes do not differ greatly (see Fig. 4.13) and the material properties are the same.

Four characteristic time steps of a full VF vibration cycle are depicted in Fig. 4.9. The maximal glottis opening is about $1/5$ of the channel size with approximately 2.95 mm (Fig. 4.9a). In the closing stage the tips of the VFs move towards each other until the minimal glottis width of 0.45 mm is reached (Fig. 4.9a). Simulations suggest that during the opening phase, the VFs tend to move asynchronously. The closing stage (Fig. 4.9c), as the vocal folds almost make contact, prevents further asymmetric behaviour and resynchronises their movement. In section 4.2, a different model is analysed, which shows an asymmetric behaviour due to the lack of close contact between VFs.

A control point on the VF was chosen to monitor the VF displacement. This point is located inside the glottis at the tip of the VF, as shown in Fig. 3.2. The recorded displacements for all simulations are Fourier transformed and the results are displayed in Fig. 4.10. In Fig. 4.10a,

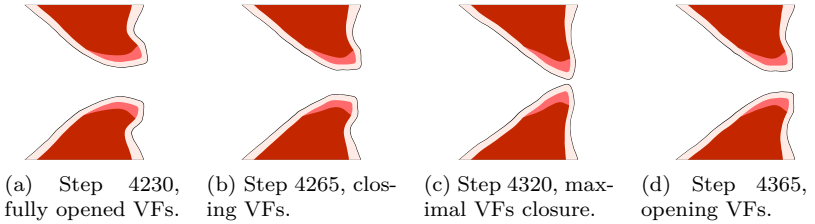


Figure 4.9: Vocal folds vibration cycle during one period. One time step is $2.5 \cdot 10^{-5}$ s long.

the vertical displacement is plotted and the two main peaks correspond to the first two eigenfrequencies of the VFs. The lateral movement is dominated by the second eigenfrequency and, to a lesser degree, at its second harmonic represented by a smaller peak. The amplitudes of the main frequencies are smaller for the case study of 800 Pa inlet pressure. This is due to weaker forces acting on the VFs. Furthermore, frequencies between 120 Hz and 216 Hz are noticeably larger when compared to the original (1 kPa inlet pressure) simulation.

4.3.2 Case study: homogeneous boundary condition

In this case study, fluid simulations with specified movements are presented. All parameters are identical to the original set-up (i.e., geometry and boundary conditions, apart from the fluid-structure interface). In the first pure fluid simulation, the interface velocity at the VFs is set to zero and in the second simulation, the fluid velocity is matched to the VF velocity at the interface. Equal VF and fluid velocity create the correct NSC, which corresponds to the fully-coupled simulation.

The volume flux of the original simulation and the prescribed simulations are displayed in Fig. 4.11a. It shows a main frequency in the volume flux at 216 Hz, which corresponds to the second eigenfrequency of the VFs and their lateral movement, the principle determiner of the fluid

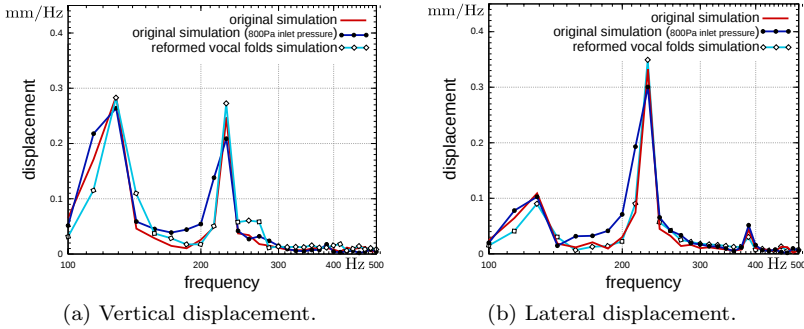


Figure 4.10: Vertical and lateral displacement as a function of frequency recorded at the control point on the VF during three different fully-coupled fluid-structural simulations.

flow. The movements prescribed with the HBC and with the NSC are in agreement with the fully-coupled simulation (i.e., frequency and amplitude coincide). However, the prescribed simulation with the HBC differs from the other two models with regard to the amplitude of the characteristic frequencies at the centre of Γ_G (Fig. 4.11b). In particular, the amplitude of the second harmonic is twice as high. These differences will have an impact on sound generation; the acoustic pressure field will be higher and the second harmonic will dominate, in contrast to the weaker fully-coupled simulation. However, the simulation with enforced no-slip conditions is in good agreement and will result in a similar acoustic field to the fully-coupled simulation. As the coupled scheme requires the iteration between fluid- and structural mechanics, the algebraic system of equations resulting from Navier-Stokes must be solved three times more frequently. Thus the simulation run time for the couple scheme was three times longer.

Mathematically, the fully-coupled simulation and the simulation case study with enforced no-slip conditions are equivalent and should result in identical results. However, the consistency of the two approaches can

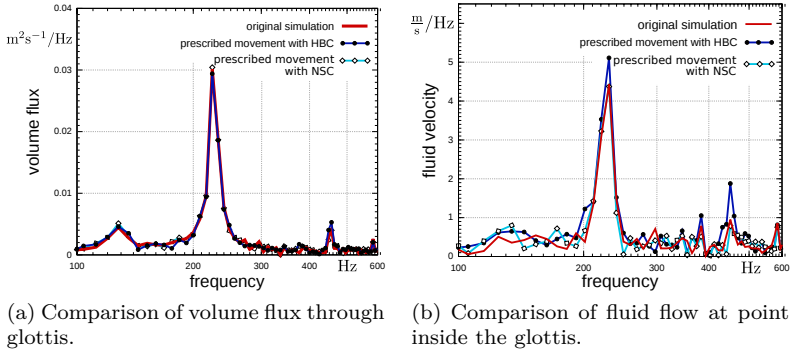


Figure 4.11: Fluid field comparison in the vertical direction of original simulation and pure fluid simulation with prescribed movement.

not be guaranteed in the discretised formulation due to the numerical approximation of the Navier-Stokes equations.

In particular, after 100 time steps, the fully-coupled scheme performed approximately 1400 solve steps (solving the algebraic system of equations) and the pure flow simulation performed about 450. Therefore, identical numerical results over a long time period is not possible. During the first time steps, both approaches show identical flow fields, but after approximately 200 time steps, they start to differ rapidly. The time point at which the two will differ may be delayed by reducing the error bound of the non-linear solver, but it is inevitable that they will differ at some point. To test for the effect of the iterative stopping criteria, the same simulations were performed with an error bound of 10^{-8} for the flow and coupling iteration (see section 4.1.1); accuracy was increased by a factor of 1000. The deviation between both simulations was only prolonged by about 100 time steps, which is minor considering the high increase in accuracy.

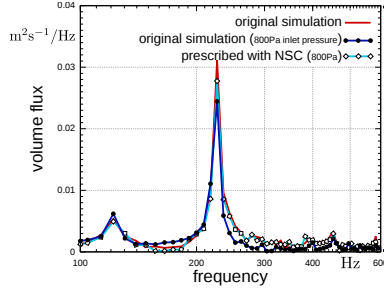


Figure 4.12: Comparison of volume flux at glottis of original simulation, simulation with reduced pressure and prescribed movement with reduced pressure.

4.3.3 Case study: 800Pa

In humans, measuring the exact pressure which drives the phonation process is difficult due to restricted access to the larynx. To simulate an inaccurate pressure measurement for a specific VFs vibration, prescribed movements are used. These are obtained from the original simulation with a reduced inlet pressure of 800 Pa. To provide an accurate representation of the interface, the fluid velocity is set equal to the VF velocities in equation (2.54), which corresponds to a no-slip condition (NSC).

The resulting volume fluxes for the two fully-coupled simulations and the prescribed simulation with reduced inlet pressure are plotted in Fig. 4.12. The amplitude at the main frequency is reduced, in contrast to the original simulation, due to the lower pressure. However, it is higher than the frequency amplitude of the fully-coupled case with 800 Pa inlet pressure, because the VFs open further. The increased opening can be deduced from the lateral displacement given in Fig. 4.10. Furthermore, reduced amplitudes at the frequency range of 120 to 216 Hz are found, which resembles the behaviour of the original simulation.

The difference in this frequency range, is due to the VFs vibration.

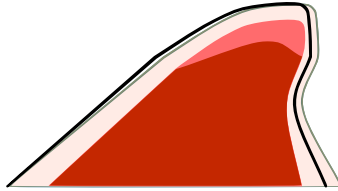


Figure 4.13: Reformed VF and outline of original geometry (solid black line).

The displacements of the original simulation (Fig. 4.10) reveal that the amplitudes in this frequency range are reduced in comparison to the fully-coupled simulation with 800 Pa inlet pressure. Therefore, it appears that with regards to pressure inlet conditions, the flow characteristic is determined by the VFs movement. Consequently, the prescribed case does not imitate the 800 Pa fully-coupled simulation correctly because frequency components are lacking and the amplitude at the main frequency is higher.

4.3.4 Case study: reformed vocal folds

It is common practice to use observations of real VFs vibration as input for the numerical simulation. However, the geometry used is not identical to the observed or measured data. Instead, simplified models are acquired since patient specific VF models are not yet available. In this case study, prescribed movement is simulated (i.e., acquired from measurements) and the obtained displacements are projected onto a different vocal fold shape. This demonstrates the effect of incorrect models or occurring measurement inaccuracies. In this case study, the two VF models differ only slightly (Fig. 4.13) maintaining similar eigenfrequency and resulting frequencies in the flow field.

To obtain a preset movement for the new geometry, each finite element node on the fluid structure interface determines its nearest neighbouring

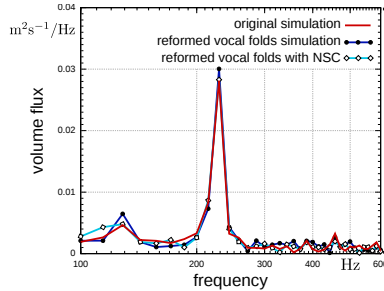


Figure 4.14: Comparison of volume flux at glottis of fully-coupled simulations with original and reformed VFs and simulation with prescribed movement on reformed VFs.

node of the original fully-coupled interface to obtain the displacement. The velocity is set accordingly (see (2.54)) and the inlet pressure in all three simulations is identical, set to 1.0 kPa.

Although the geometry change is minor, the volume flux is effected (Fig. 4.14). The volume flux at the two main frequencies is 7–8% higher for the fully coupled case with reformed VFs. It is likely that a greater difference in the geometry will have a correspondingly greater effect on the results. However, it should be noted that the prescribed movement does have the same characteristic peaks as the original fully-coupled simulation. This suggests that small measurement errors in the VFs shape do not have a strong impact on the volume flux. Therefore, a fluid simulation with prescribed movement is feasible.

4.3.5 Case study: reformed vocal folds with prescribed inflow

The basic model remains identical to the previous section, e.g., reformed VFs, prescribed movement from the original set-up, no-slip condition. The only difference is that the inflow pressure was replaced by a non-

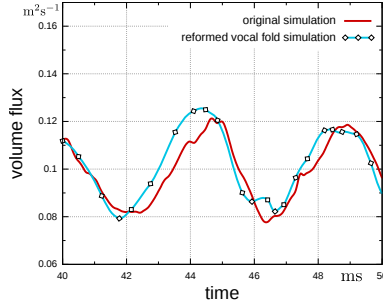
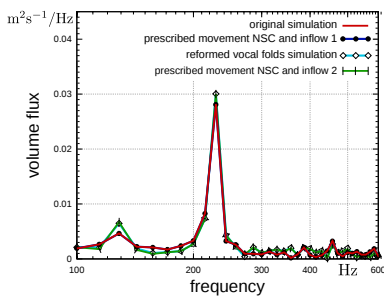
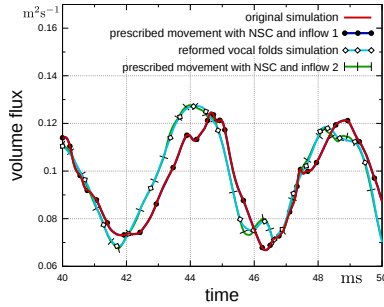


Figure 4.15: Extraction of volume flux at inflow for the fully-coupled simulations with original and reformed VFs.

uniform velocity profile, which was extracted from the original simulation. A second simulation uses the inflow profile of the fully-coupled simulation with reformed VFs. The first inflow condition is referred to as “inflow 1”, while the inflow condition gained from the simulation with reformed VFs is referred to as “inflow 2”. A time interval of the volume flux obtained by these two inflow conditions is depicted in Fig. 4.15. Next, simulations are performed with prescribed movement obtained from the original simulation and projected onto the reformed vocal folds; once with “inflow 1” and once with “inflow 2”. The results of the volume flux through the glottis do not appear to differ from previous findings (Fig. 4.16a). However, a closer look shows that the simulations with the same inflow have an identical volume flux through the glottis, regardless of whether they are prescribed or fully-coupled. This observation becomes clearer when the fluid flux is visualised in time (see Fig. 4.16b). Simulations with the same inflow also have the same flux through the glottis. This is especially interesting when the prescribed movements from the original simulation are applied, but “inflow 2” condition is used. This results in the same volume flux as the fully-coupled simulation with reformed VFs, however, the VF motion is different. The structural displacement of the VFs does not have an effect on the volume flux through the glottis when velocity



(a) Comparison of volume flux in the frequency domain.



(b) Comparison of volume flux in the time domain.

Figure 4.16: Volume flux through glottis in the time domain and frequency domain obtained by fully-coupled simulations with original and reformed VFs and simulations with prescribed movement on reformed VFs once with “inflow 1” and once with “inflow 2”.

profiles are used as inflow condition.

This example illustrates the importance of fluid-structure interaction. Generally, a change in the fluid field will result in a change of the VFs displacement which, in turn, affects the flow field. However, in the investigated cases of driven inflow, the flow field does not influence the VF movement.

4.3.6 Conclusion and summary

First, the investigations show that a homogeneous boundary condition for the flow velocity, in addition to the coupling interface, results in higher fluid velocities inside the glottis. Thus, one has to apply no-slip boundary conditions. Next, varying the inlet pressure (using 800 Pa rather than 1 kPa) results, not only in reduced volume fluxes at the main frequencies, but also in-between them, which is caused by the reduced oscillation amplitudes of the VFs. Furthermore, small deviations in the geometry of the VFs cause small differences in the fluid flux (7 – 8%), compared to the fully-coupled computation. Finally, replacing the pressure driven flow by a prescribed inflow condition demonstrates that the volume flux is unaffected by the prescribed movement. Consequently, the motion of the VFs does not have a strong effect on the volume flux through the glottis if velocity profiles are used as inflow condition.

A prescribed methodology has the advantage of significantly reducing the computational time, in this case by a factor of three. Although some agreement between the methodologies can be achieved, it is important to note the effects of the fluid flow on the acoustic sources and acoustic pressure. Higher flow velocities have an impact on the sound pressure level. A reduction or an increase of the flow amplitudes in a specific frequency range will also cause a change in the acoustic field. Therefore, in certain scenarios (e.g., velocity profile inflow condition), a fully-coupled scheme cannot be replaced by a pure fluid simulation with prescribed movement.

CHAPTER 5

3D Simulation results

This chapter is focused on acoustics resulting from a 3D flow simulation of the human phonation process. Three dimensional flow models can simulate turbulence and dispersion of vortices, which are the cause of broad frequency spectra concerning acoustic source terms. This broad band spectra is found in dysphonia, like hoarseness. Consequently, analysing flow effects and the resulting acoustics, may offer a detailed insight into voice production. As the larynx and the ventricular and real VFs form a complex geometry and flow velocities are relatively high, the airflow will inevitably develop turbulent structures, even in a healthy voice. It is therefore of interest to determine the flow field of a healthy voice differs from an unhealthy one.

Acoustic results presented in this chapter are calculated from flow simulations based on works by Schwarze et al. [79] and Šidlof et al. [95]. The first model, presented in section 5.1, is based on an experimental set-up by Triep et al. [92]. The main features of this model include an elliptic

glottal opening and a velocity inflow condition. The impact of static and dynamic moving VFs as well as different inflow conditions are analysed. The second model, presented in section 5.2, uses a simple 2D extruded geometry and a pressure gradient at the in- and outlet drives the flow. Different acoustic methodologies are then compared and a vocal tract is added to emulate the radiation from the mouth. By additionally simulating different glottal openings mimicking insufficient glottal closure, it exhibits the potential to analyse a variety of realistic phonation conditions.

As fully coupled FSI models are still difficult to tackle in 3D, the vocal folds movement are imposed, which are defined in the relevant sections. The CFD models are based on the time-dependent, incompressible Navier-Stokes equations for Newtonian fluids, as given in (2.24). They are numerically solved with the finite volume method in a cell-centred formulation using the open source CFD code *OpenFOAM*, presented by Weller et al. [97].

5.1 Velocity driven flow

A simulation model was constructed according to a measurement set-up from Triep et al. [92]. It is a 3D channel which is scaled up by a factor of three in comparison to the real human larynx. Additionally, water was used as the fluid in order to simplify the measurement since characteristic frequency and velocities are strongly reduced, as described in section 5.1.3. Variations of VF motion and inflow conditions are used to isolate the effects of each sound source mechanism. For comparison and verification purposes, the model is a replica of the experimental set-up of Triep et al. [92].

5.1.1 Geometry

In contrast to simplified models of the glottal constriction, e.g. slit-like models with a rectangular glottal cross-section or axi-symmetric models, we chose an elliptic form as depicted in Fig. 5.1 and presented by Triep et al. [92]. Its glottis form is similar to the shape found in the majority of healthy males (Inwald et al. [48]). All the dimensions given in Fig. 5.1 are based on the width D of the channel cross section.

Two different VF model configurations are considered in this computational study. The first is a static, fully opened state, so that the constriction ensures a lens-like shape, depicted in the transversal (y - z) cross section of Fig. 5.1. The maximum opening width of this constriction is h_{\max} with approximately $0.13D$. The opened length of the constriction in the z -direction is $0.8D$ so that a closed length of $0.1D$ is present at each end. The lens-shaped constriction reduces the area of the transversal cross-section by a factor of approximately eighteen. In the coronal cross-section (x - y), the constriction is contoured like a nozzle with a smooth convergent entry and a strong divergent exit. In a second configuration, the VFs are in motion, corresponding to the work of Triep et al. [92]. This dynamic model extends these characteristics of the glottal gap to a time varying opening area of the constriction, as plotted in Fig. 5.2. The VFs perform a time-varying prescribed movement that leads to a lens-like opening of the glottal constriction in transversal cross-section

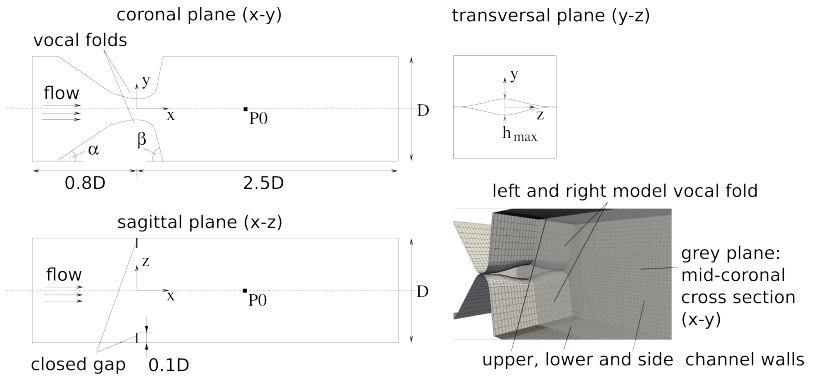


Figure 5.1: Geometry of the 3D computational domain sketched for three main cross-sections—coronal (x-y), sagittal (x-z) and transversal (yz).

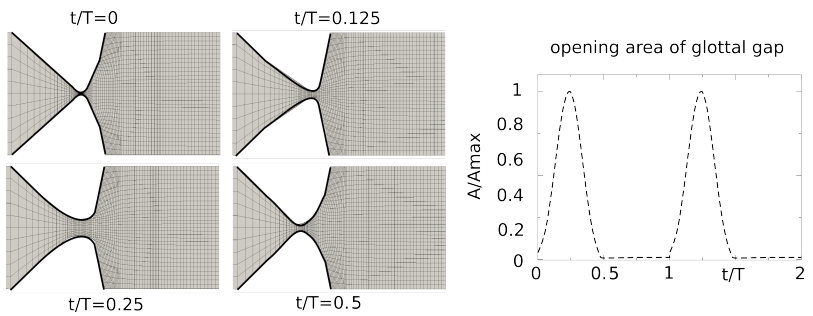


Figure 5.2: Dynamic model undergoes variation of the geometry according to depicted opening function of the glottal gap, static model corresponds to maximum opening of the glottal gap at $t/T=0.25$.

and a convergent to divergent nozzle shaped constriction in coronal cross section.

The inflow boundary is close to the glottal constriction, since no influence is exerted on the flow field with regard to its position and the velocities across the inflow boundary are expected to be uniformly distributed. In contrast, the outflow boundary is located 2.5D downstream of the constriction. All vortical structures of the pulsating supraglottal jet flow are captured since the penetration depth of the jet ranges between 1D and 1.5D. Shear layer vortices and their decay are within this range, so that only small structures are convected out of the computational domain.

5.1.2 Numerical framework

The computational domain as previously described in section 5.1.1 is meshed in a fully block structured manner with about $9 \cdot 10^5$ hexahedral cells. The cell length in the x-direction reduces from about $0.042D$ at the inflow to $0.0083D$ at the smallest cross section. Downstream, as the area of the cross-section is spread up to the channel width, massive cell expansion and distortion is avoided by introducing additional elements, whilst still conserving the block structure. The geometry of the constriction walls contains no sharp edges to ensure pressure driven flow separation, which is crucial in glottal flow as reported by Alipour and Scherer [1]. Regions near the walls have been refined by a layer of 15 cells in the normal direction to the wall, so that the condition for dimensionless wall distance $y^+ \approx 1$ is fulfilled. Here y^+ is defined with the velocity gradient u_τ at the wall, the wall distance y and the kinematic viscosity ν .

For the interpolation of the convective flux terms, a Total-Variation-Diminishing (TVD) scheme with a flux limiter function

$$\psi(r) = \max(0, \min(2r, 1))$$

by van Leer [93] is employed. The smoothness parameter r defines the ratio of successive gradients. A central differencing scheme with non-orthogonal correction is used to discretise the diffusive term. Time in-

tegration is performed with a scheme which blends the Crank-Nicholson and Euler implicit scheme by a weighting factor of 0.8 and 0.2, respectively. The time step size is kept constant at $\Delta t = 1 \cdot 10^{-5}$ s in all simulations. Mass conservation is enforced with the transient PISO algorithm (Issa [51]) with a collocated arrangement of pressure and velocity, which is in line with the correction presented by Rhie and Chow [74] in order to avoid non-physical oscillations in the flow variables. An algebraic multi-grid solver with Gauss-Seidel smoothing is used to solve the pressure. The momentum equations are solved with the bi-conjugate gradient algorithm of Fletcher [35], where incomplete LU decomposition is used to precondition the system. The residual error bounds for both iterative solvers were set to 10^{-8} .

No-slip condition $\mathbf{u}^{\text{wall}} = 0$ for velocity and zero normal gradient condition $\partial p / \partial \mathbf{n} = 0$ for pressure are defined for each wall boundary. At initial simulation time $t = 0$, the whole flow field is at rest.

This formulation of the CFD model with stationary VFs has been validated in a study by Schwarze et al. [79], where good agreement between numerical simulations and experimental measurements has been found.

5.1.3 Similitude model

In accordance with the experimental set-up (see Triep et al. [92]), the physical properties of water are chosen for the flow computation. Here, velocities and time are strongly reduced to make experimental measurements easier. To match the results for an air stream through a human sized larynx, the physical quantities are scaled in such a way that the Strouhal number (St), Reynolds number (Re) and Euler number (Eu)

are kept constant

$$Re = \frac{u_{\max}^{\text{air}} h^{\text{air}}}{\nu^{\text{air}}} = \frac{u_{\max}^{\text{water}} h^{\text{water}}}{\nu^{\text{water}}} \quad (5.1)$$

$$St = \frac{f_0^{\text{air}} h^{\text{air}}}{u_{\max}^{\text{air}}} = \frac{f_0^{\text{water}} h^{\text{water}}}{u_{\max}^{\text{water}}} \quad (5.2)$$

$$Eu = \frac{2\Delta p^{\text{air}}}{\rho^{\text{air}} (u_{\max}^{\text{air}})^2} = \frac{2\Delta p^{\text{water}}}{\rho^{\text{water}} (u_{\max}^{\text{water}})^2}. \quad (5.3)$$

In (5.1)-(5.3) ν^{medium} , denotes the kinematic viscosity in the appropriate medium, u_{\max} the maximum velocity, h_{\max} the maximum width of the glottal gap, f_0 the fundamental frequency of the oscillation, ρ the density and p the hydrodynamic pressure. These quantities and the resulting scaling factors for each relevant physical quantity are summarised in Tab. 5.1. In this thesis, referred physical quantities are regarded to be in air. *CFS++* was enhanced to convert these dimensions to calculate the acoustic sources and the wave propagation in air.

Inflow conditions

Realistic volume flows of the human phonation have been used as the inflow condition for the fluid field. The values have been taken from the experimental cam-model of Triep et al. [92]. Thereby, a driving pressure gradient Δp generated a pulsating flow-rate through the time-varying glottal constriction. The resulting volume flow waveform function was extracted and inserted as a uniform velocity distribution $u^{\text{in}}(t)$ into the inflow boundary condition of the computational model. Figure 5.3 displays the waveforms as a function over the flowrate. This has also been done for two pressure gradients of 600 Pa and 1400 Pa applied to the static and dynamic model, resulting in an overall comparison of 4 simulation set-ups. Rothenberg [75] also obtained this type of waveform with the method of inverse filtering. The represented open quotient of 0.5 is

Table 5.1: Characteristic values of the similarity parameters of the air flow in the laryngeal channel that are preserved by the model.

dimension	value	scaling factor (Water→Air)
characteristic dimension	$D = 20 \text{ mm}$	1/3
maximum velocity	$u_{\max} = [25 \dots 120] \text{ m/s}$	45
kinematic viscosity	$\nu_{\text{water}} = 1.0 \cdot 10^{-6} \text{ m}^2/\text{s}$	13
density (water)	$\rho_{\text{water}} = 1.0 \cdot 10^3 \text{ kg/m}^2$	1/975.6
glottis height	$h = 2.67 \text{ mm}$	1/3
main frequency	$f_0 = 135 \text{ Hz}$	135
pressure gradient (in- to outlet)	$\Delta p = \{600, 1400\} \text{ Pa}$	2

characteristic for healthy glottal airflow (Titze [89]).

The peak Reynolds number, as calculated by (5.1), is for the high pressure gradient with a moving glottal gap $Re_{\max} = 24030$ and for the low pressure gradient $Re_{\max} = 12930$. In the case of static glottal gap, a high pressure gradient causes $Re_{\max} = 12320$ and low pressure gradient $Re_{\max} = 5320$, respectively. Additionally, a sinusoidal waveform function as given in Fig. 5.3a is applied to the static model, which has a peak Reynolds number of $Re_{\max} = 14820$. The case of the sinusoidal waveform not only serves for validation purposes of the pulsating jet flow but provides additional insight into certain acoustic phenomena (see section 5.1.5). For details on verification for the static VF model see Schwarze et al. [79].

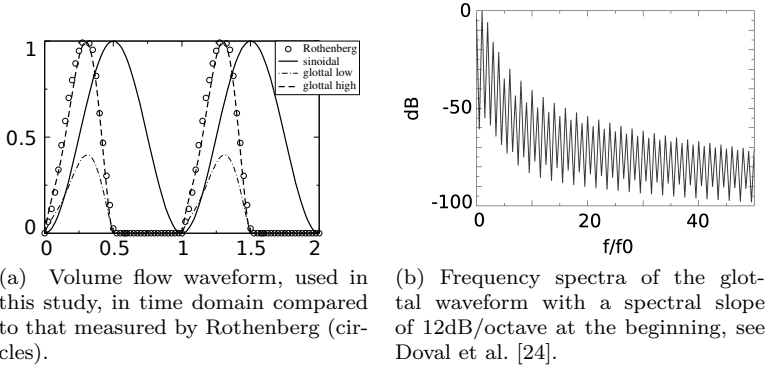


Figure 5.3: Volume flow waveforms were applied to the inlet boundary condition of the computational domain, the data was extracted from the experimental investigations of Triep et al. [92], and compared to that measured by Rothenberg [75].

5.1.4 Acoustic sources

McGowan [67] investigated the sound mechanisms in phonation from a fluid mechanical point of view. He introduces the vorticity-velocity interaction force, which is identical to the Lamb vector \mathbf{L} , apart from the density constant (see eq.(5.4)). To derive a relationship between this force and sound production, McGowan argues, based on Powell [72], that the Lighthill tensor \mathbf{T} may be approximated by the divergence of the Lamb vector,

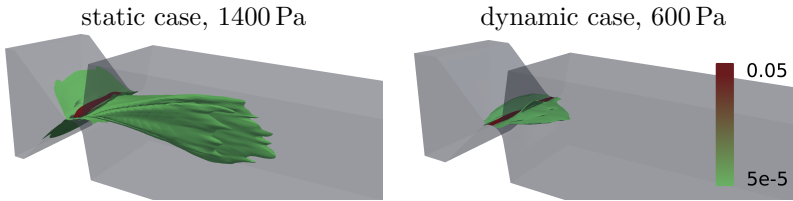
$$\frac{\partial \mathbf{T}_{ij}}{\partial x_i \partial x_j} \approx \rho \nabla \cdot \mathbf{L} = \rho \nabla \cdot ((\nabla \times \mathbf{u}) \times \mathbf{u}). \quad (5.4)$$

This approach is used to investigate the sound sources for two cases, the static simulation with a pressure gradient of 1400 Pa and the dynamic simulation with 600 Pa. Applying the Fast-Fourier-Transformation (FFT), the divergence of the Lamb vector is analysed for the main fre-

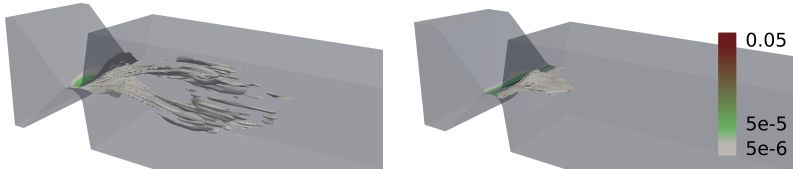
quency (135 Hz), the 6th harmonic (945Hz) and at 1kHz, which are plotted with the help of isosurfaces in Fig. 5.4. All results are normed to the maximum value taken from the dynamic simulation and the isosurfaces are visualised for the values 0.05 and $5 \cdot 10^{-5}$. For the analysis of 1 kHz, an additional isosurface at $5 \cdot 10^{-8}$ is introduced for the static case and for the dynamic case at $5 \cdot 10^{-7}$. The results indicate that at the main frequency the dominant source is clearly found inside the glottis. To be precise the highest values are found right above the surface of the VFs, forming a thin layer of sound sources. These are induced by the net force acting onto the surface of the VFs, also found by Zhao et al. [100]. Although the two simulations have approximately the same Reynolds number, their source distribution regarding lower magnitudes differ. For the static case, the source region corresponds to the shear layer of the jet and is quite extended in comparison to the dynamic case. As for the dynamic case, sources at the same magnitude are mainly found inside the glottis, barely penetrating the supraglottal tract. Looking at the source terms at the 6th harmonic, given in Fig. 5.4b, it becomes evident that for the static case the turbulent region 1D downstream of the glottis significantly contributes to the sound production. In contrast, the dynamic case not only has higher amplitudes but the source region is still localised at the glottis, as for the main frequency. For a non harmonic source, Fig. 5.4c displays the divergence of the Lamb vector at 1 kHz. Thereby, for the static case the sources concentrate on the vortical decay region, whereas for the dynamic case the sources correspond to the flow of the jet and are of one magnitude lower. In both cases, the sound sources are caused by the vortices, as can be deduced from the flow results presented by Schwarze et al. [79], and are of more than one order of magnitude lower than the sources inside the glottis, which corresponds to the findings of Zhao et al. [100]. The impact and further analysis into the acoustic is discussed in the upcoming section.

5.1.5 Aeroacoustic fields

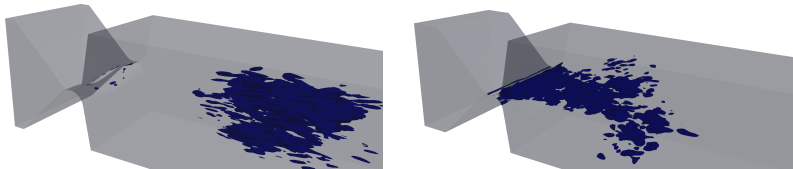
All computations have a simulation time of about 0.074s, which results in 10 cycles of the main phonation frequency of 135 Hz. The acoustic



(a) Isosurfaces at main frequency (135 Hz).



(b) Isosurfaces at 6th harmonic (945 Hz).



(c) Isosurfaces at $5 \cdot 10^{-7}$ for the static and $5 \cdot 10^{-8}$ for the dynamic case, at 1 kHz.

Figure 5.4: Isosurfaces of divergence of the Lamb vector in frequency domain for the static case with 1400 Pa pressure gradient (column left) and the dynamic case with 600 Pa pressure gradient (column right). The results are normed to the maximum value of the dynamic case.

simulation was performed on a time step size of about $7.4 \cdot 10^{-5}$ s, which according to the sampling theorem leads to a sufficient resolution for frequencies up to 5.0 kHz. For both cases with a 600 Pa and 1400 Pa pressure gradient, the acoustic frequency spectra are plotted in Fig. 5.5 for the static and dynamic case and as expected, the case with 1400 Pa has higher amplitudes. This is apparent, since higher velocities inside the glottis lead to a higher velocity gradient, which in turn results in higher acoustic sources. In mathematical terms this correlation is evident in Lighthill's tensor (2.69), which consists of the first and second derivatives of the velocity vector. Furthermore, from the analysis of the source terms, it is evident that the main sources are localised inside the glottis.

For the static case, the higher inlet pressure causes vortices to dissipate later which is noticeable in the sound spectra (see Fig. 5.5a) in which the pressure amplitudes of frequencies above 800 Hz are still significant, whereas with the pressure gradient of 600 Pa the amplitudes decrease with higher frequency. Comparing the two dynamic cases in Fig. 5.5b reveals similar results. At the main frequency and harmonics, the amplitudes are 5–10 dB higher for the 1400 Pa case compared to the lower pressure head, whereas amplitudes at frequencies in between are up to 20 dB higher.

The static simulation with a pressure gradient of 1400 Pa has a similar Reynolds number to the dynamic case with a 600 Pa pressure gradient. Their acoustic results are plotted separately for better comparison in Fig. 5.6. At the first three main frequencies the sound pressure level is identical, but they differ with regards to higher harmonics. For the dynamic case the harmonics are much more distinct, whereas for the static case the harmonics are covered up by other frequencies which have amplitudes over 20 dB higher than in the dynamic case. This effect is already clear by analyzing the divergence of the Lamb vector in Fig. 5.4, where for higher harmonics the dynamic case has higher amplitudes and the sources are focused inside the glottis. Furthermore, as Fig. 5.4c shows, acoustic sources caused by turbulence are of one magnitude higher for the static case.

In Fig. 5.7 the sinusoidal inflow condition is contrasted with the dynamic case with a 600 Pa pressure gradient. Figure 5.7a shows how the open quotient of 0.5 influences the acoustic field. During glottal closure the

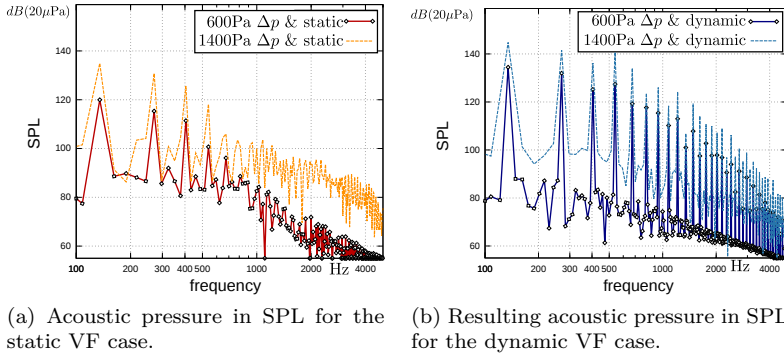


Figure 5.5: Frequency spectra of acoustic pressure for the static and dynamic cases with a pressure gradient of 600 Pa and 1400 Pa.

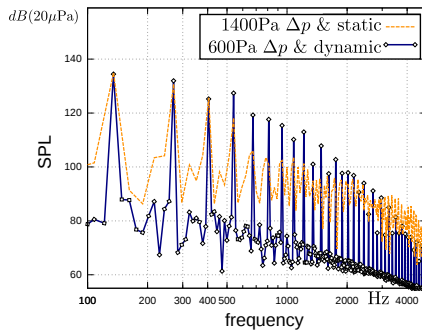
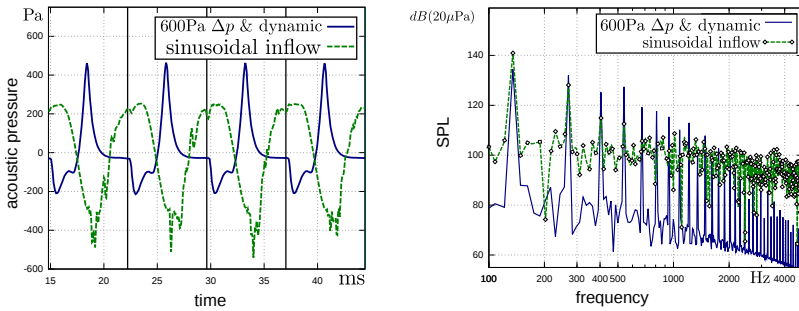


Figure 5.6: Frequency spectra of acoustic pressure for a pressure gradient of 1400 Pa without VF motion compared to the case with a pressure gradient of 600 Pa.

vortices disperse and the fluid field is more or less at rest. Hence, no acoustic sources are in the channel during this stage of the cycle. The effect is noticeable in the acoustic pressure, as it is almost constant to the end of each cycle. However, the sinusoidal inflow condition does not result in a uniform fluid field at any time. Looking at the frequency spectra, as depicted in Fig. 5.7b, the impact becomes more obvious. The main frequency and its harmonic are indistinguishable above the 5th harmonic frequency for the sinusoidal case, whereas for the glottal waveform all harmonics are very distinct, even up to 5 kHz. In terms of the signal to noise ratio, apart from the main frequency, all harmonics of the glottal wave form simulation have a higher acoustic pressure level and all other frequencies are significantly lower. A connection to the Reynolds number cannot be drawn since both are of same order, with about 14 820 for the sinusoidal case and 12930 for the dynamic case, but have very different SPLs concerning amplitude and frequency response.

The sound signal of the sinusoidal case is comparable to a human patient suffering from hoarseness. For this kind of dysphonia, high speed-imaging reveals an insufficient glottic closure, as in the static cases. Glottic closure initiates each cycle, avoiding flow structures to influence the succeeding cycles. As a result, the acoustic main frequency and harmonics are clearly distinguishable—the foundation of a healthy voice.



(a) Time signal comparison. Vertical lines are introduced to indicate the periodic phonation cycles.

(b) Frequency spectra of both cases.

Figure 5.7: Results of acoustic pressure in time and frequency domain of a monitoring point at the outflow for the sinusoidal case and glottal inflow with a pressure gradient of 600 Pa and dynamic VFs.

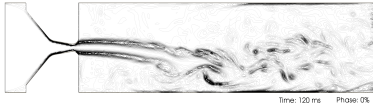
5.2 Pressure driven flow

With regard to the fluid simulation, this second model differs from the previous presented 3D model in two key points. (1) The glottis opening is slit-like and (2) the flow develops naturally due to a pressure gradient condition of 300 Pa defined at the in- and outlet—in contrast to a velocity driven flow. This ensures that any occurring frequencies arise from the VF movement, which is prescribed, and not from the inflow condition. The imposed VF vibration is symmetrical and solely in the medial-lateral direction with a frequency of $f = 100$ Hz, leaving a minimum glottal gap $g_{\min} = 2 \cdot 0.1$ mm and maximum glottal opening $g_{\max} = 2 \cdot 0.9$ mm.

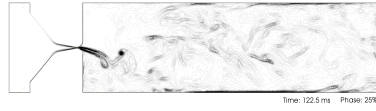
The fluid simulations on which the upcoming results are based were performed by Dr. Petr Šidlof. The methodology of the fluid mechanical problem and detailed analysis are found in his recent work [95]. For the sake of completeness, Fig. 5.8 shows vorticity contours at 4 characteristic time instances during vibration of the VFs. It shows how the jet develops throughout the opening phase and attaches to the bottom wall, until it is almost completely cut off by the glottal closure.

The focus in this section lies in comparing two hybrid methods, Lighthill's acoustic analogy, as presented in section 2.4.1, and the perturbation ansatz presented in section 2.4.3. For a complete characterisation of these approaches, the simulation domain is extended by a realistic but geometrical fixed vocal tract and a propagation region, as covered in section 5.2.1.

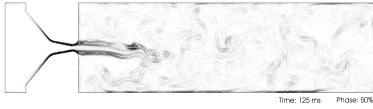
With this enhanced acoustic model it is now possible to analyse the cause and effect of certain phonation phenomena, for instance the impact of supraglottal structures. In section 5.2.4, the acoustic impact of false vocal folds (FVFs), also known as ventricular folds, are investigated. Figure 5.9a shows the flow field at time step 180 ms, when the jet is fully developed, of the simulation with and without FVFs. The flow rate in Fig. 5.9b reveals that with FVFs the peak flow rate is about 10% reduced. This leads back to the smaller pressure gradient between glottis and supraglottal region, as Fig. 5.9c confirms, showing a plot of the pressure along the glottal midline. A thorough flow analysis is not



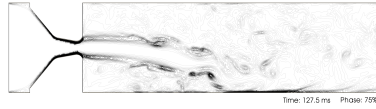
(a) Beginning of 12th cycle, VFs closing.



(b) Vocal folds closed and jet is cut off.



(c) Vocal folds open and jet starts to develop.



(d) End of 12th cycle, VFs fully opened and jet fully developed.

Figure 5.8: Vorticity contours at 4 characteristic time steps during the 12th cycle of VF vibration (courtesy of Dr. Petr Šidlof [95]).

the aim as it exceeds the scope of this work ¹.

5.2.1 Geometry

A rectangular shaped larynx with VF geometries “M5” proposed by Scherer et al. [76] is used in this set-up. A 2D slice of the fluid domain is sketched in Fig. 5.10a, which is extruded in depth to acquire a 3D model (see Fig. 5.10b). Once the fluid simulations are carried out, changes are made to the domain, which are necessary for the acoustic simulation. A vocal tract is appended to the laryngeal geometry and an extended region is added to this in order to monitor the radiated sound from the mouth (see Fig. 5.11a). The vocal tract model is directly attached to the larynx and consists of multiple frustums concatenated one after another. The number of frustums and their radius determines the resulting sound radiating from the artificial mouth. The cross sections (so-called area

¹A publication, comparing fluid flow and acoustics of simulations with and without FVFs, is in progress.

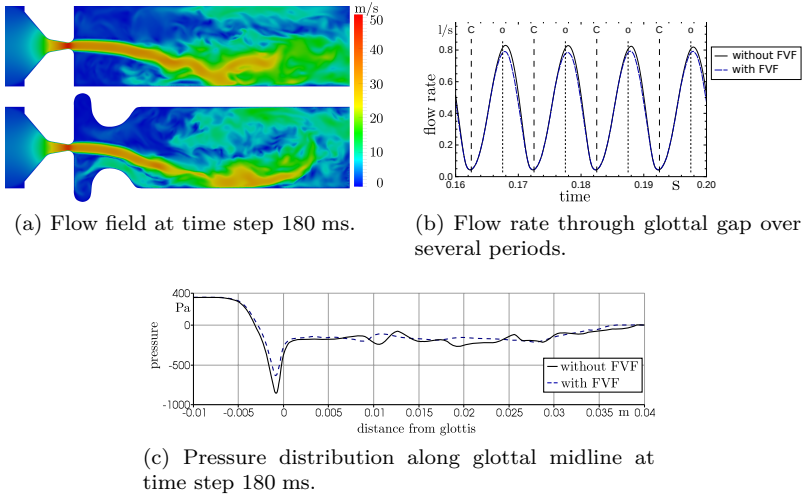


Figure 5.9: Fluid dynamic results in comparison, with and without FVFs. (courtesy of Dr. Petr Šidlof [95])

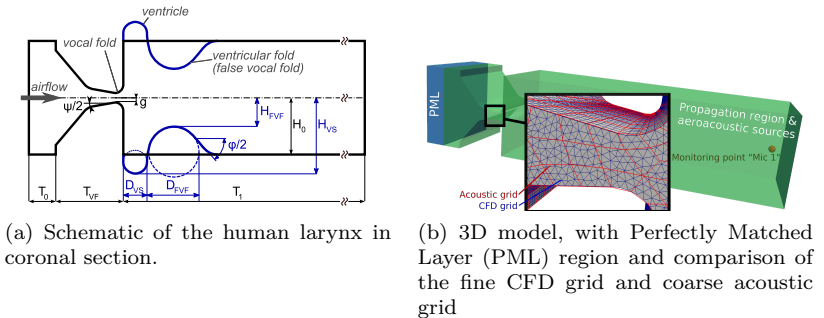


Figure 5.10: Schematic of the human larynx, with acoustic monitoring point at end of channel.

functions) were taken from works by Story et al. [82], who acquired 3D vocal tract shapes of particular vowels and consonants by means of magnetic resonance imaging (MRI). Thereby, 18 vocal tract configurations were discussed, each being divided up into single segments, with a length of about 3.97 mm. Two of these shapes are used in this work, representing the sounds /i/ (“heed”) and /u/ (“who”). The vocal tract for /i/ consists of 44 segments and for /u/ of 46 segments resulting in a length of approximately 17.5 cm and 18.25 cm, respectively. The area of the vocal tracts segments as a function of distance from the larynx is plotted for both models in Fig. 5.11b. Since the CFD simulations are run on a simple rectangular channel and the vocal tract geometry is circular, the small discrepancies to the shape measured by Story et al. [82] introduce an error which will be discussed later. At the end of the vocal tract, the mouth, an acoustic propagation region is added to capture the effect of an impedance jump due to the transition from the relatively small volume of the vocal tract to an open domain.

Consequently, the acoustic domain consists of three subdomains as depicted in Fig. 5.11a. The first subdomain is the acoustic source region, where the fluid simulation is performed and in which the flow induced sources are computed. The fine grid of the fluid simulation (characteristic length 0.15 mm) is unnecessary for the acoustic calculation. Therefore, to preserve acoustic energy, the acoustic sources are conservatively interpolated onto a coarser grid with a characteristic length of 2 mm (see Fig. 5.10b). According to Kaltenbacher [54], this leads to a correct frequency resolution in space of up to 8.5 kHz, as 20 finite elements per wave length are required. Once the acoustic sources are determined, the sound propagation is computed on the whole acoustic domain, consisting of both the larynx (fluid flow—source region), and the vocal tract and radiation regions. PML regions are to be found in front of the larynx and surrounding the far field to ensure no acoustic wave leaving the domain is reflected back.

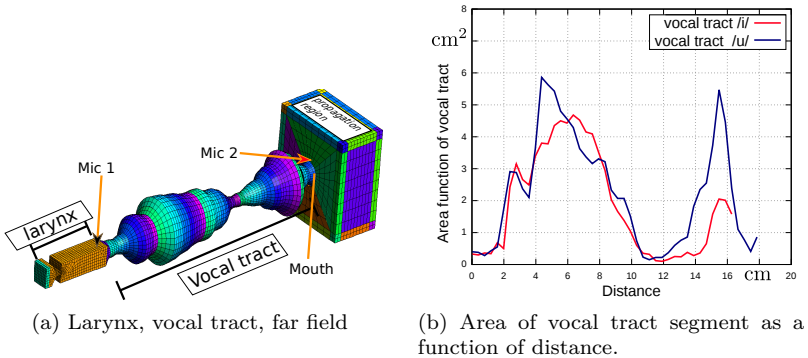


Figure 5.11: Geometry and mesh for the acoustic simulation.

5.2.2 Acoustic sources

The acoustic sources are investigated for the pressure driven simulation in the same manner as for the velocity driven set-up discussed in the previous section 5.1.4. In addition to the derivative of the Lamb vector, given in (5.4), the source terms provide by the perturbation equation in (2.79) are visualised and compared.

Applying the Fast-Fourier-Transformation (FFT), all source terms for the main frequency (100 Hz) and at 1425 Hz are analysed. These are plotted with the help of isosurfaces in Fig. 5.12. For each acoustic approach the results are normed to their maximum value and the isosurfaces are visualised for the values 0.4, 0.1, $9.5 \cdot 10^{-3}$ and $1 \cdot 10^{-3}$. For the analysis of 1425 Hz, additional isosurfaces are introduced, which are specified in the corresponding caption to the figures.

The results indicate that at the main frequency the dominant source is clearly found inside the glottis. To be precise, the highest values are found right above the surface of the VFs, as in the previous section 5.1.4. This effect is especially visible for the divergence of the Lamb vector, as the isosurface at the value $1 \cdot 10^{-3}$ is found directly on the surface of the

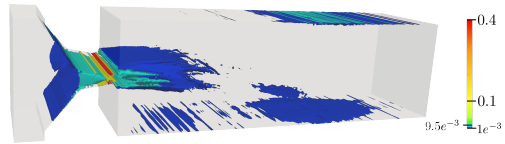
VF's. Also downstream, at the top and bottom of the supraglottal wall, a surface-like source region is found. This is caused by the main vortex, which deflects the jet (see section 5.2). This, together with the no-slip boundary condition, leads to high velocity gradients towards the walls, and as can be deduced from (5.4), to these source regions.

For a non harmonic, Fig. 5.12c and Fig. 5.12d displays the acoustic sources at the frequency 1 425 Hz. Thereby, the sources concentrate in the vortical decay region. For the divergence of the Lamb vector, the jet is also a contributor to the sources at this frequency, emphasising that for a proper display the isosurface is a magnitude lower than for the source terms of the perturbation equations. Sound sources based on vortical structures are of magnitude lower than the sources inside the glottis, as determined in section 5.1.4 and Zhao et al. [100].

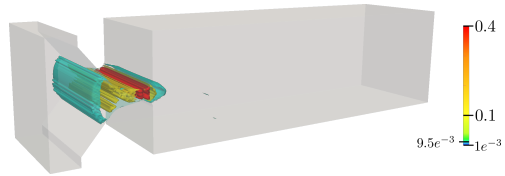
5.2.3 Vocal tract influence

As stated by Lighthill [59], Lighthill's acoustic analogy is not valid inside the flow field. To confirm this assumption, acoustic pressure determined by the two approaches at the monitoring point "Mic 1" (see Fig. 5.10a) will be compared. In addition, a comparison is made for the microphone "Mic 2", positioned 1 cm downstream from the vocal tract, inside the propagation region—outside the flow field. For "Mic 2" the impact of the different vocal tract, representing /i/ and /u/, is analysed.

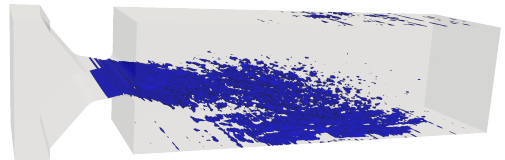
Figure 5.13 presents the acoustic sound spectrum at the position "Mic 1". The two approaches show a discrepancy over the whole frequency range. Calculations performed with the wave equation reveal a significant higher sound pressure level (SPL), up to 20 dB for the main frequency of 100 Hz. Furthermore, the relations between the frequency are different: For the frequency range of 0.5–2.5 kHz the wave equation stagnates at about 70–80 dB, whereas for the perturbation equation the SPL rises from about 55 dB–75 dB in the range of 0.5–1.3 kHz and then drops down to 50 dB at 2.5 kHz. Consequently, higher harmonics are indistinguishable for the wave equation case, but for the perturbation equation, harmonics up to 700 Hz are detectable. This indicates that for acoustics inside the flow field Lighthill's analogy significantly overestimates not only the SPL over



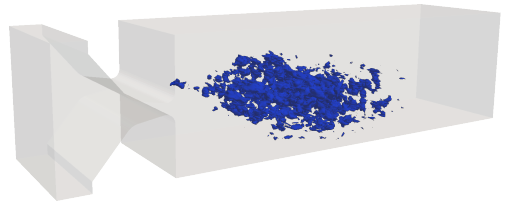
(a) Lighthill tensor at 100 Hz



(b) PE source terms at 100 Hz



(c) Lighthill tensor at 1425 Hz with the isosurface at $3 \cdot 10^{-4}$



(d) PE source terms at 1425 Hz with the isosurface at $1.6 \cdot 10^{-3}$

Figure 5.12: Acoustic source of the two hybrid approaches at different frequencies.

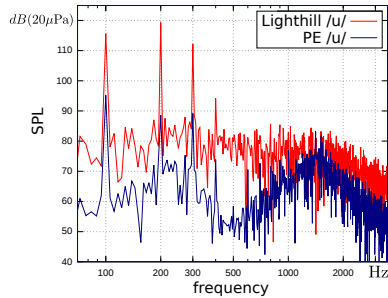


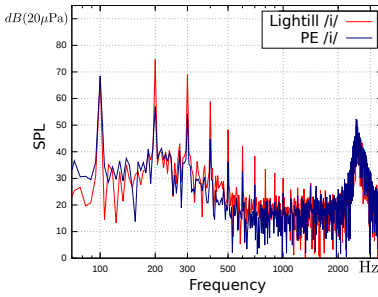
Figure 5.13: Acoustic pressure inside the flow domain, at “Mic 1” with vocal tract /u/ attached.

the whole frequency range, but also the relation of the SPL between frequencies. This becomes clear as Lighthill’s approach does not decompose the total pressure as done for the perturbation equation in section 2.4.3. It therefore also includes fluctuating pressure that is purely hydrodynamical and not acoustical, which accounts for the higher results.

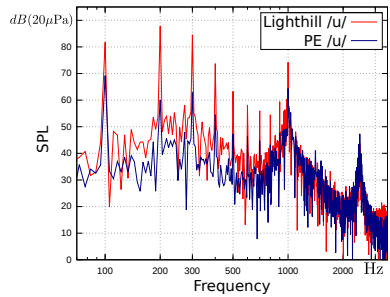
The sound spectrum evaluated at “Mic 2” is given in Fig. 5.14 for the /i/ and /u/ vowels, comparing both aeroacoustic approaches. The computed formant frequencies (local maxima of the spectral envelope, distinctive attributes of the individual vowels) are summarised in Tab. 5.2, and compared to the formant frequencies of natural speech published by Story et al. [82]. In both cases the first formant is not in accordance with natural speech, whereas for the second and third formants the error is below 10%. Since both numerical approaches show identical formants, it is suspected that the discrepancy to natural speech in the first formant is caused by the geometrical deviation of the model with respect to Story’s measured data (especially by introducing the additional volume of the larynx). Figure 5.14 shows the excellent agreement between Lighthill’s and the PE approach. The spectra do show different amplitudes for the fundamental frequency of 100 Hz and its harmonics, nevertheless, all formants are identical in frequency and amplitude, which also holds for the frequency range in between. By comparing with the spectra evaluated

Table 5.2: First three formants from natural speech as given by Story et al. [82] and simulated by our reproduced vocal tract. Denoted by superscript “N” is the natural speech and “S” the simulated version (Lighthill’s analogy and PE are identical).

	$/i/^{N}$	$/i/^{S}$	$/u/^{N}$	$/u/^{S}$
F1	333	292	389	270
F2	2332	2538	987	1000
F3	2986	2749	2299	2484

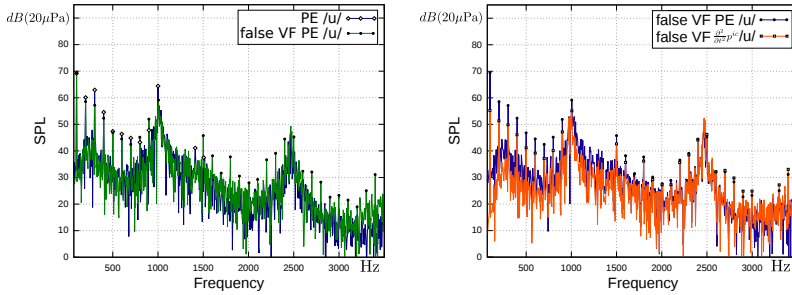


(a) SPL for vocal tract $/i/$.



(b) SPL for vocal tract $/u/$.

Figure 5.14: Acoustic sound spectra at a monitoring point 1 cm downstream of the mouth for both vocal tract models, comparing Lighthill’s acoustic analogy and the perturbation equations.



(a) Acoustic results of the perturbation equations, comparing with and without FVFs.

(b) Comparing the perturbation equations and the wave equation with the source term $\partial^2/\partial t^2 p^{ic}$.

Figure 5.15: Acoustic sound spectra at a monitoring point 1 cm downstream of the mouth for the vocal tract model /u/, comparing with and without FVFs. Harmonics are emphasised with the symbol \diamond (without FVFs) and \bullet (with FVFs) for the perturbation approach and for the wave equation the symbol \square (with FVFs) is used.

inside the larynx, it can be reasoned that the harmonics overestimated by Lighthill’s approach follow from the source region, which shows a similar pattern of the harmonic frequencies.

5.2.4 Acoustic impact of false vocal folds

To assess the acoustic impact of the FVFs, it is sufficient to focus on the results achieved with the perturbation equations on the simulation domain representing the vocal tract /u/. In Fig. 5.15a the observed frequency spectra are contrasted with the simulation without false vocal folds. These differ only in the harmonics. Without FVFs, harmonics dominate other frequencies up to 1 kHz, whereas with FVFs they are clearly visible over the whole illustrated frequency range. This phenomena is noticeable when analysing the acoustic sources in Fig. 5.16, where they are plotted in the coronal plane at one of the harmonics (2.6 kHz).

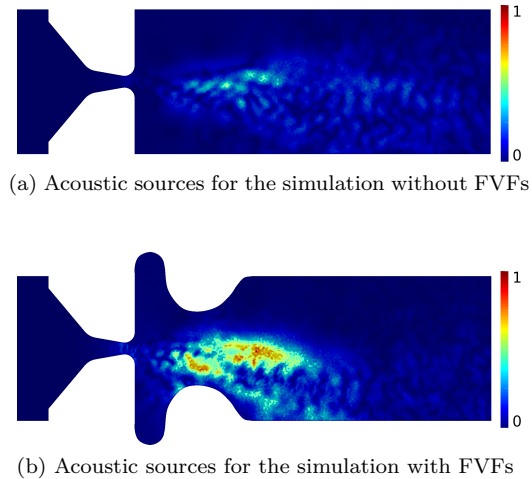


Figure 5.16: Acoustic sources of the acoustic perturbation equation at 2.6 kHz in the coronal plane. Normed to the maximum value found for the FVFs case.

The figure reveals that by including the FVFs a significantly larger source region is generated, which is higher in amplitude.

Another comparison between hybrid methods is presented in Fig. 5.15b. Here, the perturbation equations and the wave equation with the second derivative in time of the incompressible pressure as source term, as presented in section 2.4.4, are compared. This wave equation approach is also in excellent agreement with the perturbation approach, although a smaller sound pressure level below 1 Hz is detectable.

5.2.5 Discussion and conclusions

Both prescribed 3D simulations have the advantage of simulating the fluid flow through the larynx realistically, since 3D flow effects can be accounted for, e.g., dissipation of vortices. Turbulence causes a broad

spectral sound and these models are therefore suited to determine the cause of a hoarse or unhealthy voice. To perform the simulations in a reasonable time, the VF vibration were induced, modelling only a one way FSI coupling. This does have drawbacks and may cause errors, as established in section 4.3. This implies that a velocity driven flow, as used in section 5.1, does not react on VF movement. Therefore, the inflow frequency determines the resulting acoustic frequency and not the vocal fold vibration. In contrast, a pressure driven flow develops naturally, as presented in section 5.2. This makes it feasible to identify definite correlations between certain acoustic phenomena and VF vibration, e.g., the influence of supraglottal structures like the FVFs (section 5.2.4). Section 5.2 presented a comparison of Lighthill's acoustic analogy and the PE ansatz, demonstrating a good agreement of the acoustic pressure outside the fluid domain. Lighthill's approach is inappropriate inside the aeroacoustic flow region, as it also includes non acoustic quantities. Additionally, it was shown that it is possible to extend the fluid simulation domain with acoustic propagation domains and thereby not only allow for acoustic analysis during phonation, but also for the whole speech process. Multiple diverse acoustic investigations can now be performed, all based on one computationally expensive fluid simulation.

CHAPTER 6

Conclusion

The object of this thesis is to analysis the effect of simplifying the human phonation model and the impact of the introduced error. Reasons for simplifications are mainly computational costs, but may also be inaccuracies from measurements or lack of data.

To ensure correct input data, a measurement set-up for determining the elasticity modulus as a function of the frequency is presented, which in future can serve as a reliable source for identifying VF material parameters. Its advantages over other measurement techniques are that it does not damage or strain the material and it can resolve small local areas.

With the numerical framework established, which is based on the work of Link [61] and implemented in *CFS++*, improvements were made to tackle the further tasks. The changes enabled the analysis of different kinds of coupling between fluid and structural mechanics. It showed that to simulate phonation, the two way coupling between the physical fields can never be fully dismissed. However, results showed good agreement,

for a pressure driven flow and compatible imposed motion of the VFs, with the equivalent fully coupled set-up. It should be emphasised that correct boundary conditions at the interface are important for the accuracy.

A further investigation into model error was to analyse the impact of the geometrical model. Thereby, a modified version of the renowned M5 VF model is compared to a realistic one, extracted from an ex vivo plaster-casting methodology by Šidlof et al. [94]. Results have proven that the latter provides a realistic vibration pattern, which is not the case for the M5 model. The M5 model was demonstrated to have significantly smaller amplitudes in lateral direction and after a few cycles the VFs started to vibrate asymmetrically.

The thesis then discusses and compares two different aeroacoustic methodologies, the acoustic analogy by Lighthill [59] and a perturbation approach as derived by Hüppe [47]. Thereby, 3D air flow simulations through the larynx, calculated with *OpenFOAM*, were used as input data for these hybrid methods. Acoustic results showed an excellent agreement between the two approaches outside the simulated flow region. However, inside the flow region, the frequency spectra do not match as, the wave equation with Lighthill's source term formulation includes non acoustical fluctuating quantities which do not propagate as acoustics into the far field. This suggests that the decomposition of the field variables in hydrodynamical and acoustical parts is required for a correct representation of acoustics inside the flow field.

With these findings, it is now possible to identify the main acoustic sources, which are to be found inside the glottis at the main frequency the VFs vibrate and also at its harmonics. Acoustic sources at non harmonic frequencies originated downstream of the glottis, which correlates to the decay of the glottal jet and occurring vortical structures. In a second stage, FVFs were included, which lead to an additional acoustic source region surrounding these subglottal features. This caused further higher harmonics to appear in the acoustical field, but without the drawback of increasing the amplitudes of any non harmonic frequencies. Furthermore, by including a static vocal tract geometry, a first step towards simulating the complete speech process was made.

6.1 Outlook

The presented measurement set-up for determining material parameters is being further developed at the Chair of Sensor Technology at the Friedrich-Alexander University Erlangen-Nuremberg. A next step is to reliably measure material parameters of VFs, as this is still an open issue and crucial for the correct simulation input data.

The thesis also analysed and discussed errors that are introduced by the model itself. Further questions to explore include, for instance, the impact of a complete realistic geometry of the larynx. Currently the air way through the larynx is modelled by a straight rectangular channel and it would be of interest to compare it to a realistic model of tubular form, which also includes bends and kinks. However, this raises the question of which geometrical properties are essential for a healthy voice and how big are the margins for variations which still allow for a healthy voice. In essence these questions analyse the robustness of the larynx as a voice producing organ, as no two larynges in humans are alike. As a note, asymmetric positioned VFs or non glottal closure during phonation can still create a perceived healthy voice. Nevertheless, glottal closure is an essential part of the phonation process, but especially challenging from a numerically point of view, since the contact of the vocal fold separates the flow domain into two parts and conventional approaches dealing with deformations cannot be applied.

Another possibility for future developments is the enhancement of the vocal tract model, used for the 3D aeroacoustic calculations. Current CT (computer tomography) or MRI (magnetic resonance imaging) could improve the resolution of the vocal tract and additionally include the nasal cavities.

APPENDIX A

Anatomical terms of location

Figure A.1 illustrates the three perpendicular reference planes and direction which are used in medicine as terms of location. The sagittal plane is a vertical plane, dividing the body into two, the right and left half. The transverse plane is horizontal and thereby perpendicular to the vertical axis. The coronal plane divides the body into front and back.

Terms for describing directions are lateral (along the left-right axis), medial (centre), superior (above), inferior (below), anterior (in front), and posterior (behind).

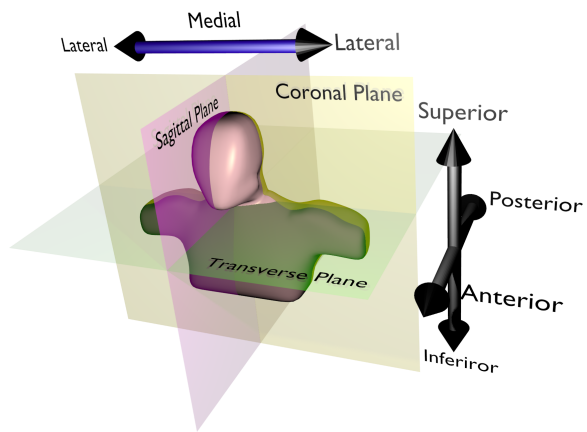


Figure A.1: Anatomical terms of location.

APPENDIX B

Mathematics for engineers

Definition (support):

The support of a function $\varphi : \Omega \rightarrow \mathcal{R}$ is defined as

$$\text{supp}(\varphi) := \overline{\{x \in \Omega : \varphi(x) \neq 0\}} \quad (\text{B.1})$$

The support is called compact if $\text{supp}(\varphi)$ is compact (i.e. closed and bounded).

Lemma (conservation of angular moment):

The Cauchy tensor $[\sigma]$ is symmetric.

Proof. Consider a body in equilibrium then the torque M (moment of force) around the y -axis, as shown in Fig. B.1, is

$$\Sigma M_y = 0.$$

The torque could also be expressed by the stress tensor tangential to its

direction

$$2\sigma_{zx}A \cdot l - 2\sigma_{xz}A \cdot l = 0$$

with area A and l the length of the moment arm. For a unit cube the area $A = dx \cdot dy$ and the length of $l = 0.5dx$. It follows $\sigma_{zx} = \sigma_{xz}$. Analogously for moments around x - and z -axis follows, $\sigma_{yz} = \sigma_{zy}$ and $\sigma_{xy} = \sigma_{yx}$, respectively. \square

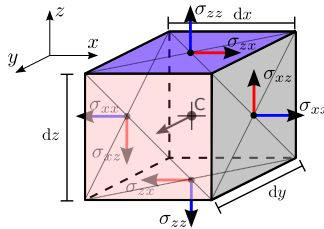


Figure B.1: Moments of force around the y -axis for a unit cube.

Definition (Voigt notation):

The symmetric Cauchy tensor

$$[\boldsymbol{\sigma}] = \begin{bmatrix} \sigma_{xx} & \sigma_{xy} & \sigma_{xz} \\ \sigma_{yx} & \sigma_{yy} & \sigma_{yz} \\ \sigma_{zx} & \sigma_{zy} & \sigma_{zz} \end{bmatrix} = \begin{bmatrix} \sigma_{11} & \sigma_{12} & \sigma_{13} \\ \sigma_{21} & \sigma_{22} & \sigma_{23} \\ \sigma_{31} & \sigma_{32} & \sigma_{33} \end{bmatrix}$$

can be simplified by using the Voigt notation to a 6-dimensional vector

$$\boldsymbol{\sigma} = \begin{pmatrix} \sigma_{11} \\ \sigma_{22} \\ \sigma_{33} \\ \sigma_{23} \\ \sigma_{13} \\ \sigma_{12} \end{pmatrix} = \begin{pmatrix} \sigma_1 \\ \sigma_2 \\ \sigma_3 \\ \sigma_4 \\ \sigma_5 \\ \sigma_6 \end{pmatrix}.$$

Definition (Time average):

The bar symbol $(\bar{\cdot})$ over a time dependent value denotes the temporal mean, e.g., for the physical value $g(x, t) : \mathbb{R} \times \mathbb{R}^+ \rightarrow \mathbb{R}$ the temporal mean is defined as

$$\bar{g}(x) := \frac{1}{T} \int_0^T g(x, t) dt. \quad (\text{B.2})$$

Lemma (Splitting technique calculus):

For a physical quantity $g(x, t)$ and $h(x, t)$ ($g, h : \mathbb{R} \times \mathbb{R}^+ \rightarrow \mathbb{R}$) that are decomposed into a temporal mean and a fluctuating part, i.e. $g(x, t) = \bar{g}(x) + g'(x, t)$, the following calculus rules hold

- (i) $\overline{\bar{g}(x)} = \bar{g}(x)$
- (ii) $\overline{g'(x, t)} = 0$
- (iii) $\overline{\bar{g}(x) \cdot h'(x, t)} = 0$
- (iv) $\overline{\bar{g}(x) \cdot h(x, t)} = \bar{g}(x) \cdot \bar{h}(x)$
- (v) $\frac{\partial}{\partial t} \bar{g}(x) = 0$
- (vi) $\overline{g(x, t) + h(x, t)} = \bar{g}(x) + \bar{h}(x)$
- (vii) $\overline{\nabla h(x, t)} = \nabla \bar{h}(x)$

Proof. As some calculus are not directly evident a short proof for each statement is sketched.

- (i) $\overline{\bar{g}(x)} = \frac{1}{T} \int_0^T \bar{g}(x) dt = \bar{g}(x) \frac{1}{T} \int_0^T 1 dt = \bar{g}(x)$
- (ii) $\overline{g'(x, t)} = \frac{1}{T} \int_0^T g(x, t) - \bar{g}(x) dt \stackrel{(i)}{=} \bar{g}(x) - \bar{g}(x) = 0$
- (iii) $\overline{\bar{g}(x) \cdot h'(x, t)} = \frac{1}{T} \int_0^T \bar{g}(x) \cdot h'(x, t) dt = \bar{g}(x) \cdot \frac{1}{T} \int_0^T h'(x, t) dt \stackrel{(ii)}{=} 0$

(iv) $\overline{g(x) \cdot h(x, t)} = \overline{g(x)} \frac{1}{T} \int_0^T h(x, t) dt = \overline{g(x)} \cdot \overline{h(x)}$

(v) $\frac{\partial}{\partial t} \overline{g(x)} = 0$, since $\overline{g(x)}$ is constant in t .

(vi) Integral operator is linear.

(vii) Integral operator and gradient operator are linear.

□

Bibliography

- [1] F. Alipour and R. C. Scherer. Flow separation in a computational oscillating vocal fold model. *Journal of the Acoustical Society of America*, 116:1710–1719, 2004.
- [2] F. Alipour, D. A. Berry, and I. R. Titze. A finite-element model of vocal-fold vibration. *The Journal of the Acoustical Society of America*, 108(6):3003–3012, 2000. doi: 10.1121/1.1324678.
- [3] F. Alipour, C. Brücker, D. D Cook, A. Gömmel, M. Kaltenbacher, W. Mattheus, L. Mongeau, E. Nauman, R. Schwarze, I. Tokuda, and S. Zörner. Mathematical models and numerical schemes for the simulation of human phonation. *Current Bioinformatics*, 6(3): 323–343, September 2011. doi: doi:10.2174/157489311796904655.
- [4] F. Alipour-Haghighi and I. R. Titze. Viscoelastic modeling of canine vocalis muscle in relaxation. *Journal of the Acoustical Society of America*, 78:1939–1943, 1985.
- [5] F. Alipour-Haghighi and I. R. Titze. Elastic models of vocal fold

- tissues. *Journal of the Acoustical Society of America*, 90:1326–1331, 1991.
- [6] T. Aoki, T. Ohashi, T. Matsumoto, and M. Sato. The pipette aspiration applied to the local stiffness measurement of soft tissues. *Annals of Biomedical Engineering*, 25:581–587, 1997.
- [7] Y. Bae and Y. J. Moon. Computation of phonation aeroacoustics by an INS/PCE splitting method. *Computers & Fluids*, 37(10): 1332–1343, 2008. ISSN 0045-7930. doi: DOI:10.1016/j.compfluid.2007.12.002.
- [8] K. J. Bathe. *Finite Element Procedures*. Prentice Hall, 1st edition, June 1995. ISBN 0133014584.
- [9] S. Becker, S. Kniesburges, S. Müller, A. Delgado, G. Link, M. Kaltenbacher, and M. Döllinger. Flow-structure-acoustic interaction in a human voice model. *Journal of the Acoustical Society of America*, 125:1351–1361, 2009.
- [10] P. Birkholz. *3D-artikulatorische Sprachsynthese*. PhD thesis, 2005.
- [11] P. Birkholz. A survey of self-oscillating lumped-element models of the vocal folds. In: *Kröger BJ, Birkholz P (eds.) Studentexte zur Sprachkommunikation: Elektronische Sprachsignalverarbeitung*, pages 184–194, 2011.
- [12] D. Braess. *Finite Elemente*. Springer, Berlin, 3. edition, 2003.
- [13] A. N. Brooks and T. J. R. Hughes. Streamline upwind/Petrov-Galerkin formulations for convection dominated flows with particular emphasis on the incompressible Navier-Stokes equations. *Computer Methods in Applied Mechanics and Engineering*, 32:199–259, 1982. doi: 10.1016/0045-7825(82)90071-8.
- [14] R. W. Chan. Estimation of viscoelastic shear properties of vocal-fold tissues based on time-temperature superposition. *Journal of the Acoustical Society of America*, 110:1548–1561, 2001.

- [15] R. W. Chan. Measurements of vocal fold tissue viscoelasticity: Approaching the male phonatory frequency range. *Journal of the Acoustical Society of America*, 115:3161–3170, 2004.
- [16] R. W. Chan and M. L. Rodriguez. A simple-shear rheometer for linear viscoelastic characterization of vocal fold tissues at phonatory frequencies. *Journal of the Acoustical Society of America*, 124:1207–1219, 2008.
- [17] R. W. Chan and I. R. Titze. Viscoelastic shear properties of human vocal fold mucosa: Theoretical characterization based on constitutive modeling. *Journal of the Acoustical Society of America*, 107: 565–580, 2000.
- [18] D. D. Cook, E. Nauman, and L. Mongeau. Ranking vocal fold model parameters by their influence on modal frequencies. *J. Acoust. Soc. Am.*, 126(4):2002–2010, 2009. doi: 10.1121/1.3183592.
- [19] M. de Oliveira Rosa, J. C. Pereira, M. Grellet, and A. Alwan. A contribution to simulating a three-dimensional larynx model using the finite element method. *The Journal of the Acoustical Society of America*, 114(5):2893–2905, 2003. doi: 10.1121/1.1619981.
- [20] G. de Vahl Davis and G. Mallinson. An evaluation of upwind and central difference approximations by a study of recirculating flow. *Computers & Fluids*, 4(1):29 – 43, 1976. ISSN 0045-7930. doi: 10.1016/0045-7930(76)90010-4.
- [21] M. P. de Vries, H. K. Schutte, A. E. P. Veldman, and G. J. Verkerke. Glottal flow through a two-mass model: Comparison of Navier–Stokes solutions with simplified models. *J. Acoust. Soc. Am.*, 111 (4):1847–1853, 2002.
- [22] G. Z. Decker and S. L. Thomson. Computational simulations of vocal fold vibration: Bernoulli versus Navier–Stokes. *J Voice*, 21: 273–284, 2007.

- [23] M. Döllinger. The next step in voice assessment: High-speed digital endoscopy and objective evaluation. *Current Bioinformatics*, 4(2): 101–111, May 2009. doi: 10.2174/157489309788184774.
- [24] B. Doval, C. d’Alessandro, and N. Henrich. The spectrum of glottal flow models. *Acta Acustica united with Acustica*, 92(6):1026–1046, 2006.
- [25] J. S. Drechsel. Characerization of synthetic, self-oscillating vocal fold models. Master’s thesis, Department of Mechanical Engineering, Brigham Young University, 2007.
- [26] F. Durst. *Grundlagen der Strömungsmechanik*. Springer, 2006.
- [27] M. Döllinger, U. Hoppe, F. Hettlich, J. Lohscheller, S. Schubert, and U. Eysholdt. Vibration parameter extraction from endoscopic image series of the vocal folds. *IEEE Trans Biomed Eng.*, 49(8): 773–781, Aug 2002.
- [28] E. Emmrich. Stability and convergence of the two-step BDF for the incompressible Navier-Stokes problem. *International Journal of Nonlinear Sciences and Numerical Simulation*, 5(3):199–209, 2004.
- [29] E. Emmrich. Error of the two-step BDF for the incompressible Navier-Stokes problem. *ESAIM: Mathematical Modelling and Numerical Analysis*, 38(5):757–764, 3 2010.
- [30] E. A. Evans. New membrane concept applied to the analysis of fluid shear- and micropipette-deformed red blood cells. *Biophysical Journal*, 13:941–954, 1973.
- [31] L. C. Evans. *Partial Differential Equations*, volume 19 of *Graduate Studies in Mathematics*. American Mathematical Society, Providence, Rhode Island, June 1998. ISBN 0821807722.
- [32] R. Ewert and W. Schröder. Acoustic perturbation equations based on flow decomposition via source filtering. *Journal of Computational Physics*, 188:365–398, 2003.

- [33] J. L. Fitch and A. Holbrook. Modal vocal fundamental frequency of young adults. *Archives of Otolaryngology*, 92(4):379–382, 1970. doi: 10.1001/archotol.1970.04310040067012.
- [34] J. Flanagan and L. Landgraf. Self-oscillating source for vocal-tract synthesizers. *Audio and Electroacoustics, IEEE Transactions on*, 16(1):57–64, mar 1968. ISSN 0018-9278. doi: 10.1109/TAU.1968.1161949.
- [35] R. Fletcher. Conjugate gradient methods for indefinite systems. 506:73–89, 1976. doi: 10.1007/BFb0080116. 10.1007/BFb0080116.
- [36] A. Gömmel. *Modellbildung und Fluid-Struktur-Interaktion in der Biomechanik am Beispiel der menschlichen Phonation*. PhD thesis, RWTH Aachen, February 2010.
- [37] E. Goodyer, S. Hemmerich, F. Muller, J. B. Kobler, and M. Hess. The shear modulus of the human vocal fold, preliminary results from 20 larynxes. *Eur Arch Otorhinolaryngol*, 264:45–50, 2006.
- [38] H. Gray, P. Williams, and L. Bannister. *Gray’s Anatomy: The Anatomical Basis of Medicine and Surgery*. Gray’s Anatomy. Churchill Livingstone, 1995. ISBN 9780443045608.
- [39] P. M. Gresho and R. L. Lee. Don’t suppress the wiggles—they’re telling you something! *Computers & Fluids*, 9(2):223 – 253, 1981. ISSN 0045-7930. doi: 10.1016/0045-7930(81)90026-8.
- [40] E. Hairer, S. P. Norsett, and G. Wanner. *Solving ordinary differential equations II: Stiff and differential-algebraic problems*. Springer, Berlin, 2nd revised edition edition, 1991.
- [41] P. Hansbo and A. Szepessy. A velocity-pressure streamline diffusion finite element method for the incompressible Navier-Stokes equations. *Computer Methods in Applied Mechanics and Engineering*, 84(2):175 – 192, 1990. ISSN 0045-7825. doi: 10.1016/0045-7825(90)90116-4.

- [42] M. M. Hess, F. Mueller, J. B. Kobler, S. M. Zeitels, and E. Goodyer. Measurements of Vocal Fold Elasticity Using the Linear Skin Rheometer. *Folia Phoniatr Logop*, 58:207–216, 2006.
- [43] G. C. J. Hofmans, G. Groot, M. Ranucci, G. Graziani, and A. Hirschberg. Unsteady flow through in-vitro models of the glottis. *The Journal of the Acoustical Society of America*, 113(3):1658–1675, 2003. doi: 10.1121/1.1547459.
- [44] E. B. Holmberg, R. E. Hillman, and J. S. Perkell. Glottal airflow and transglottal air pressure measurements for male and female speakers in low, normal, and high pitch. *Journal of Voice*, 3(4):294–305, 1989. ISSN 0892-1997. doi: 10.1016/S0892-1997(89)80051-7.
- [45] T. J. Hughes. *The Finite Element Method*. Dover, Mineola, N.Y., 1. edition, 2000.
- [46] T. J. R. Hughes, W. K. Liu, and T. K. Zimmermann. Lagrangian-Eulerian finite element formulation for incompressible viscous flows. *Computer Methods in Applied Mechanics and Engineering*, 29(3): 329–349, 1981. ISSN 0045-7825. doi: 10.1016/0045-7825(81)90049-9.
- [47] A. Hüppe. *Spectral finite elements for acoustic field computation*. PhD thesis, Alps-Adriatic University of Klagenfurt, 2012.
- [48] E. C. Inwald, M. Döllinger, M. Schuster, U. Eysholdt, and C. Bohr. Multiparametric Analysis of Vocal Fold Vibrations in Healthy and Disordered Voices in High-Speed Imaging. *Journal of Voice*, 25(5): 576 – 590, 2011. ISSN 0892-1997. doi: 10.1016/j.jvoice.2010.04.004.
- [49] B. M. Irons and R. C. Tuck. A version of the aitken accelerator for computer iteration. *International Journal for Numerical Methods in Engineering*, 1(3):275–277, 1969. ISSN 1097-0207. doi: 10.1002/nme.1620010306.
- [50] K. Ishizaka and N. Isshiki. Computer simulation of pathological vocal-cord vibration. *J. Acoust. Soc. Am.*, 60:1193–1198, 1976.

- [51] R. I. Issa. Solution of the implicitly discretised fluid flow equations by operator-splitting. *Journal of Computational Physics*, 62(1): 40–65, 1986. ISSN 0021-9991. doi: 10.1016/0021-9991(86)90099-9.
- [52] A. Johnson and T. Tezduyar. Mesh update strategies in parallel finite element computations of flow problems with moving boundaries and interfaces. *Computer Methods in Applied Mechanics and Engineering*, 119(1-2):73 – 94, 1994. ISSN 0045-7825. doi: 10.1016/0045-7825(94)00077-8.
- [53] B. Kaltenbacher, M. Kaltenbacher, and I. Sim. A modified and stable version of a perfectly matched layer technique for the 3-d second order wave equation in time domain with an application to aeroacoustics. *Journal of Computational Physics*, 235(0):407 – 422, 2013. ISSN 0021-9991. doi: <http://dx.doi.org/10.1016/j.jcp.2012.10.016>.
- [54] M. Kaltenbacher. *Numerical Simulation of Mechatronic Sensors and Actuators*. Springer, Berlin, 2. edition, 2007. ISBN 978-3-540-71359-3.
- [55] M. Kaltenbacher, M. Escobar, I. Ali, and S. Becker. Numerical Simulation of Flow-Induced Noise Using LES/SAS and Lighthill’s Acoustics Analogy. *International Journal for Numerical Methods in Fluids*, 63(9):1103–1122, 2010. doi: 10.1002/fld.2123.
- [56] M. Kob. *Physical modeling of the singing voice*. PhD thesis, Rheinische-Westfälische Technische Hochschule Aachen, 2002.
- [57] U. Küttler and W. A. Wall. Fixed-point fluid-structure interaction solvers with dynamic relaxation. *Computational Mechanics*, 43(1): 61–72, 2008. ISSN 0178-7675. doi: 10.1007/s00466-008-0255-5.
- [58] M. Larsson and B. Müller. Numerical simulation of confined pulsating jets in human phonation. *Computers & Fluids*, 38(7):1375–1383, 2009. ISSN 0045-7930. doi: 10.1016/j.compfluid.2008.01.033. Special Issue Dedicated to Professor Alain Lerat on the Occasion of his 60th Birthday.

- [59] M. J. Lighthill. On sound generated aerodynamically I. General theory. *Proceedings of the Royal Society of London*, 211:564–587, 1951.
- [60] M. J. Lighthill. On sound generated aerodynamically II. Turbulence as a source of sound. *Proceedings of the Royal Society of London*, 222:1–32, 1953.
- [61] G. Link. *A Finite Element Scheme for Fluid-Solid-Acoustics Interactions and its Application to Human Phonation*. PhD thesis, Technisch Fakultät Universität Erlangen-Nürnberg, 2008.
- [62] G. Link, M. Kaltenbacher, M. Breuer, and M. Döllinger. A 2d finite-element scheme for fluid-solid-acoustic interactions and its application to human phonation. *Computer Methods in Applied Mechanics and Engineering*, 198:3321–3334, 2009.
- [63] R. Löhner and C. Yang. Improved ale mesh velocities for moving bodies. *Communications in Numerical Methods in Engineering*, 12(10):599–608, 1996. ISSN 1099-0887. doi: 10.1002/(SICI)1099-0887(199610)12:10<599::AID-CNEM1>3.0.CO;2-Q.
- [64] H. Luo, R. Mittal, X. Zheng, S. A. Bielamowicz, R. J. Walsh, and J. K. Hahn. An immersed-boundary method for flow-structure interaction in biological systems with application to phonation. *Journal of Computational Physics*, 227:9303–9332, 2008.
- [65] T. Matsumoto, H. Abe, T. Ohashi, Y. Kato, and M. Sato. Local elastic modulus of atherosclerotic lesions of rabbit thoracic aortas measured by pipette aspiration method. *Physiological Measurement*, 23:635–648, 2002.
- [66] W. Mattheus and C. Brücker. Asymmetric glottal jet deflection: Differences of two- and three-dimensional models. *The Journal of the Acoustical Society of America*, 130(6):EL373–EL379, 2011. doi: 10.1121/1.3655893.

- [67] R. S. McGowan. An aeroacoustic approach to phonation. *The Journal of the Acoustical Society of America*, 83(2):696–704, 1988. doi: 10.1121/1.396165.
- [68] R. Mittal, S. P. Simmons, and F. Najjar. Numerical study of pulsatile flow in a constricted channel. *Journal of Fluid Mechanics*, 485:337–378, May 2003. doi: 10.1017/S002211200300449X.
- [69] R. Mittal, B. D. Erath, and M. W. Plesniak. Fluid dynamics of human phonation and speech. *Annual Review of Fluid Mechanics*, 45(1):null, 2013. doi: 10.1146/annurev-fluid-011212-140636.
- [70] T. Ohashi, H. Abe, T. Matsumoto, and M. Sato. Pipette aspiration technique for the measurement of nonlinear and anisotropic mechanical properties of blood vessel walls under biaxial stretch. *Journal of Biomechanics*, 38:2248–2256, 2004.
- [71] H. Parkus. *Mechanik der festen Körper*, volume 2. Springer, Wien NewYork, 2009 (orig. 1966). ISBN 978-3211807774.
- [72] A. Powell. Theory of vortex sound. *The Journal of the Acoustical Society of America*, 36:177 – 196, 1964.
- [73] R. P. Rand and A. C. Burton. Mechanical Properties of the Red Cell Membrane I. Membrane Stiffness and Intracellular Pressure. *Biophysical Journal*, 4:115–135, 1964.
- [74] C. M. Rhie and W. L. Chow. Numerical study of the turbulent flow past an airfoil with trailing edge separation. *AIAA*, 21(11): 1525–1532, 1983.
- [75] M. Rothenberg. A new inverse-filtering technique for deriving the glottal air flow waveform during voicing. *The Journal of the Acoustical Society of America*, 53(6):1632–1645, 1973. doi: 10.1121/1.1913513.
- [76] R. C. Scherer, D. Shinwari, K. J. D. Witt, C. Zhang, B. R. Kucinski, and A. A. Afjeh. Intraglottal pressure profiles for a symmetric

- and oblique glottis with a divergence angle of 10 degrees. *The Journal of the Acoustical Society of America*, 109(4):1616–1630, 2001. doi: 10.1121/1.1333420.
- [77] R. C. Scherer, D. Shinwari, K. J. D. Witt, C. Zhang, B. R. Kucinski, and A. A. Afjeh. Intraglottal pressure distributions for a symmetric and oblique glottis with a uniform duct (L). *The Journal of the Acoustical Society of America*, 112(4):1253–1256, 2002. doi: 10.1121/1.1504849.
- [78] H. R. Schwarz and N. Köckler. *Numerische Mathematik*. Vieweg+Teubner, 2008.
- [79] R. Schwarze, W. Mattheus, J. Klostermann, and C. Brücker. Starting jet flows in a three-dimensional channel with larynx-shaped constriction. *Computers & Fluids*, 48(1):68–83, 2011. ISSN 0045-7930. doi: 10.1016/j.compfluid.2011.03.016.
- [80] J. H. Seo and R. Mittal. A high-order immersed boundary method for acoustic wave scattering and low-Mach number flow-induced sound in complex geometries. *J. Comput. Phys.*, 230:1000–1019, February 2011. ISSN 0021-9991. doi: <http://dx.doi.org/10.1016/j.jcp.2010.10.017>.
- [81] I. Steinecke and H. Herzel. Bifurcations in an asymmetric vocal-fold model. *Journal of the Acoustical Society of America*, 97(3):1874–1884, 1995. doi: 10.1121/1.412061.
- [82] B. H. Story, I. R. Titze, and E. A. Hoffman. Vocal tract area functions from magnetic resonance imaging. *The Journal of the Acoustical Society of America*, 100(1):537–554, 1996. doi: 10.1121/1.415960.
- [83] J. Suh and S. H. Frankel. Numerical simulation of turbulence transition and sound radiation for flow through a rigid glottal model. *The Journal of the Acoustical Society of America*, 121(6):3728–3739, 2007. doi: 10.1121/1.2723646.

- [84] C. Tao, Y. Zhang, D. G. Hottinger, and J. J. Jiang. Asymmetric airflow and vibration induced by the Coanda effect in a symmetric model of the vocal folds. *J. Acoust. Soc. Am.*, 122(4):2270–2278, 2007. doi: 10.1121/1.2773960.
- [85] T. E. Tezduyar, S. Mittal, S. E. Ray, and R. Shih. Incompressible flow computations with stabilized bilinear and linear equal-order-interpolation velocity-pressure elements. *Computer Methods in Applied Mechanics and Engineering*, 95(2):221–242, 1992. ISSN 0045-7825. doi: 10.1016/0045-7825(92)90141-6.
- [86] I. R. Titze. The human vocal cords: A mathematical model. I. *Phonetica*, 28(3):129–70, 1973.
- [87] I. R. Titze. The human vocal cords: A mathematical model. II. *Phonetica*, 29(1):1–21, 1974.
- [88] I. R. Titze. The physics of small-amplitude oscillation of the vocal folds. *Journal of the Acoustical Society of America*, 83(4):1536–52, 1988.
- [89] I. R. Titze. *The myoelastic aerodynamic theory of phonation*. The National Center of Voice and Speech, Denver, 2006.
- [90] I. R. Titze, S. A. Klemuk, and S. Gray. Methodology for rheological testing of engineered biomaterials at low audio frequencies. *Journal of the Acoustical Society of America*, 115:392–401, 2004.
- [91] M. Triep and C. Brücker. Three-dimensional nature of the glottal jet. *The Journal of the Acoustical Society of America*, 127(3):1537–1547, 2010. doi: 10.1121/1.3299202.
- [92] M. Triep, C. Brücker, and W. Schröder. High-speed PIV measurements of the flow downstream of a dynamic mechanical model of the human vocal folds. *Experiments in Fluids*, 39:232–245, 2005.

- [93] B. van Leer. Towards the ultimate conservative difference scheme. V. A second-order sequel to Godunov's method. *Journal of Computational Physics*, 32(1):101–136, 1979. ISSN 0021-9991. doi: 10.1016/0021-9991(79)90145-1.
- [94] P. Šidlof, J. G. Švec, J. Horáček, J. Veselý, I. Klepáček, and R. Havlík. Geometry of human vocal folds and glottal channel for mathematical and biomechanical modeling of voice production. *Journal of Biomechanics*, 41:985–995, 2008. doi: 10.1016/j.jbiomech.2007.12.016.
- [95] P. Šidlof, J. Horáček, and V. Řídký. Parallel CFD simulation of flow in a 3D model of vibrating human vocal folds. *Computers & Fluids*, 80(0):290 – 300, 2013. ISSN 0045–7930. doi: 10.1016/j.compfluid.2012.02.005. Selected contributions of the 23rd International Conference on Parallel Fluid Dynamics ParCFD2011.
- [96] W. A. Wall. *Fluid-Struktur-Interaktion mit stabilisierten Finiten Elementen*. PhD thesis, Universität Stuttgart, Holzgartenstr. 16, 70174 Stuttgart, 1999.
- [97] H. G. Weller, G. Tabor, H. Jasak, and C. Fureby. A tensorial approach to computational continuum mechanics using object-oriented techniques. *Computers in Physics*, 12:620–631, 1998.
- [98] D. Wong, M. R.Ito, N. B.Cox, and I. R. Titze. Observation of perturbations in a lumped-element model of the vocal folds with application to some pathological cases. *The Journal of the Acoustical Society of America*, 89(1):383–394, 1991. doi: 10.1121/1.400472.
- [99] A. Yang, M. Stingl, D. A. Berry, J. Lohscheller, D. Voigt, U. Eysholdt, and M. Döllinger. Computation of physiological human vocal fold parameters by mathematical optimization of a biomechanical model. *The Journal of the Acoustical Society of America*, 130(2): 948–964, 2011. doi: 10.1121/1.3605551.
- [100] W. Zhao, C. Zhang, S. H. Frankel, and L. Mongeau. Computational aeroacoustics of phonation, part I: Computational methods and

- sound generation mechanisms. *Journal of the Acoustical Society of America*, 112:2134–2146, 2002.
- [101] W. Zhao, C. Zhang, S. H. Frankel, and L. Mongeau. Computational aeroacoustics of phonation, part II: Effects of flow parameters and ventricular folds. *Journal of the Acoustical Society of America*, 112: 2147–2154, 2002.
- [102] X. Zheng, Q. Xue, R. Mittal, and S. Beilamowicz. A coupled sharp-interface immersed boundary-finite-element method for flow-structure interaction with application to human phonation. *J. Biomech. Eng.*, 132(11):111003, 2010. doi: 10.1115/1.4002587.
- [103] X. Zheng, R. Mittal, and S. Bielamowicz. A computational study of asymmetric glottal jet deflection during phonation. *The Journal of the Acoustical Society of America*, 129(4):2133–2143, 2011. doi: 10.1121/1.3544490.
- [104] X. Zheng, R. Mittal, Q. Xue, and S. Beilamowicz. Direct-numerical simulation of the glottal jet and vocal-fold dynamics in a three-dimensional laryngeal model. *J. Acoust. Soc. Am.*, 130 (1):404–415, 2011. doi: 10.1121/1.3592216.
- [105] S. Zörner, M. Kaltenbacher, and M. Döllinger. Investigation of prescribed movement in fluid-structure interaction simulation for the human phonation process. *Computers & Fluids*, 86(0):133–140, 2013. ISSN 0045-7930. doi: 10.1016/j.compfluid.2013.06.031.

Curriculum Vitae

Personal Data

Name: Stefan Zörner
Date of Birth: April 8,1981
Place of Birth: Stade, Germany

Education

2000 Diploma from secondary school,
German School Prague, Czech Republic
10/2000 – 10/2002 Studied Informatics
Friedrich-Alexander-University
Erlangen-Nuremberg, Germany
10/2002 – 11/2007 Dipl.-Math. in Mathematics
Friedrich-Alexander-University
Erlangen-Nuremberg, Germany

Professional Experiences

07/2001 – 12/2002 Research assistant at the RRZE
(Regionales Rechenzentrum Erlangen)
03/2006 – 03/2007 Research assistant at the
Fraunhofer Institute for Integrated Systems
and Device Technology, Erlangen, Germany
01/2008 – 06/2008 PhD. student, Chair of Sensors Technology,
FAU Erlangen-Nuremberg, Germany
07/2008 – 06/2012 PhD. student, Institute of Smart System-
Technologies, Alps-Adriatic University,
Klagenfurt, Austria
07/2012 – PhD. student, Institute of Mechanics and
Mechatronics,
Vienna University of Technology, Austria